Theoretical Insights into Catalysis on Nanoporous Gold from *Ab Initio* Molecular Dynamics

Dissertation

zur Erlangung des Doktorgrades der Naturwissenschaften

- Dr. rer. nat. -

des Fachbereichs 2 (Biologie/Chemie)

der Universität Bremen

vorgelegt von

Yong Li

Bremen, 06 Oktober 2020

Supervisor: Prof. Dr. Marcus Bäumer

Erstgutachter: Prof. Dr. Tim Stauch

Zweitgutachter: Prof. Dr. Lucio Colombi Ciacchi

Versicherung an Eides Statt

Ich, Yong Li, Sonderburger Str.17 Bremen, Germany, Matr.-Nr. 3068082

versichere an Eides Statt durch meine Unterschrift, dass ich die vorstehende Arbeit selbständig und ohne fremde Hilfe angefertigt und alle Stellen, die ich wörtlich dem Sinne nach aus Veröffentlichungen entnommen habe, als solche kenntlich gemacht habe, mich auch keiner anderen als der angegebenen Literatur oder sonstiger Hilfsmittel bedient habe.
Ich versichere an Eides Statt, dass ich die vorgenannten Angaben nach bestem Wissen und Gewissen gemacht habe und dass die Angaben der Wahrheit entsprechen und ich nichts verschwiegen habe.
Die Strafbarkeit einer falschen eidesstattlichen Versicherung ist mir bekannt, namentlich die Strafandrohung gemäß § 156 StGB bis zu drei Jahren Freiheitsstrafe oder Geldstrafe bei vorsätzlicher Begehung der Tat bzw. gemäß § 161 Abs. 1 StGB bis zu einem Jahr Freiheitsstrafe oder Geldstrafe bei fahrlässiger Begehung.

Bremen, 06.07. 2020 Yong Li
_____

Ort, Datum Unterschrift

Acknowledgment

Upon completion of this dissertation, I would like to express my gratitude to those who have offered help, kindness and encouragement during the preparation of my doctoral dissertation.

First of all, I would like to thank **Dr. Lyudmila V. Moskaleva** for organizing and supporting this PhD project. It is my honor to have worked with you and your meticulous attitude and extensive knowledge always helped a lot in my academic research. Thank you for the guidance you have supported me with during my studies.

I want to thank **Prof. Dr. Marcus Bäumer** for all the discussions and suggestions regarding scientific presentation and writing. Your comprehensive knowledge of physics and surface science offered an especially important contribution to this work.

I want to thank **Prof. Dr. Thomas Risse** and **Prof. Dr. Thorsten Klüner** for their valuable input, discussions and guidance in the course of this work. I would also like to thank **Simona Keil,** who is very approachable and shared an office with me for four years. It has been my pleasure working with you.

My sincere gratitude goes to **Priv. Doz. Dr. Volkmar Zielasek**, **Dr. Arne Wittstock, Dr. Sebastian Kunz, Junjie Shi**, **Anastasia Lackmann** and all other IAPC group members for providing me a pleasant and comfortable working environment. It has been a pleasure working with you. Thank you for sharing your knowledge and ideas with me.

Finally, I would also like to thank my friends and family for supporting and encouraging me.

List of Publications

Papers I, II, III, IV, and V listed below build the foundation of this dissertation.

[I] S. Hoppe, **<u>Yong Li</u>**, L.V. Moskaleva, S. Müller. How Silver Segregation Stabilizes 1D Surface Gold Oxide: a Cluster Expansion Study Combined with *Ab Initio* MD Simulations. ***Phys***. ***Chem***. ***Chem***. ***Phys***., 2017, 19 14845-14853.

Contribution: I was responsible for designing the AIMD model, carrying out AIMD simulation, and writing the AIMD part of the manuscript.

[II] **<u>Yong Li</u>**, W. Dononelli, R. Moreira, T. Risse, M. Bäumer, T. Klüner, L.V. Moskaleva. Oxygen-Driven Surface Evolution of Nanoporous Gold: Insights from *Ab Initio* Molecular Dynamics and Auger Electron Spectroscopy. ***J***. ***Phys***. ***Chem***. ***C***, 2018, 122, 5349-5357. (Cover paper)

Contribution: I was responsible for designing the theoretical model, carrying out the computation, analyzing data, and contributed significantly to writing the theoretical part of the manuscript.

[III] **<u>Yong Li</u>**, S. Li, M. Bäumer, E. Ivanova-Shor, L.V. Moskaleva. What Changes on the Inverse Catalyst? Insight from CO Oxidation on Au-Supported Ceria Nanoparticles using *Ab Initio* Molecular Dynamics. ***ACS***. ***Catal***., 2020, 10, 3164-3174.

Contribution: I was responsible for designing all theoretical models, carrying out all computations, analyzing data, and contributed significantly to writing the manuscript.

[IV] **<u>Yong Li</u>**, S. Li, M. Bäumer, L. V. Moskaleva. Transient Au-CO Complexes Promote the Activity of an Inverse Ceria/Gold Catalyst: an Insight from *Ab Initio* Molecular Dynamics. ***J. Catal.*** (Under revision)

Contribution: I was responsible for designing all theoretical models, carrying out all computations, analyzing data, and contributed significantly to writing the manuscript.

[V]   G. Tomaschun, W. Dononelli, **Yong Li**, M. Bäumer, T. Klüner, L.V. Moskaleva. Methanol Oxidation on the Au(3 1 0) Surface: A theoretical Study. *J. Catal*., 2018, 364, 216-227.

Contribution: I contributed to designing a theoretical model, carryied out part of the computation and contributed to manuscript writing.

In addition to my PhD project, I also participated in other research activities, which resulted in the following publications:

[VI] Z. Zhuang, **Yong Li**, Z. Li, F. Lv, Z. Lang, K. Zhao, L. Zhou, L. Moskaleva, S. Guo, L. Mai. MoB/g-C$_3$N$_4$ Interface Materials as a Schottky Catalyst to Boost Hydrogen Evolution. *Angew. Chem. Int. Ed.*, 2018, 57, 496-500.

Contribution: I was responsible for providing all theoretical interpretation and computation and theoretical part of manuscript writing.

[VII] J. Du, **Yong Li**, H. Liu, W. Shi, L.V. Moskaleva, P. Cheng. Formation of One-Dimensional Coordination Chains for High-Performance Anode Materials of Lithium-Ion Batteries via a Bottom-Up Approach. *ACS Appl. Mater. Interfaces*, 2019, 11, 25863-25869.

Contribution: I was responsible for providing all theoretical interpretation and computation and writing the theoretical part of the manuscript.

[VIII] C.-X. Wang, **Yong Li**, Z.-F. Li, Z.-J. Liu, E.F. Valeev, L.V. Moskaleva. A Combined Relativistic *Ab Initio* Multireference and Experimental Study of the Electronic Structure of Terbium Luminescent Compound. *J. Phys. Chem. A*, 2020, 124, 82-89.

Contribution: I was responsible for providing all theoretical interpretation and computation and writing theoretical part of the manuscript.

Zusammenfassung

Nanoporöses Gold (np-Au) hat sich kürzlich als hochselektiver Katalysator mit Potential für umweltfreundlichen Einsatz bei niedrigen Temperaturen herausgestellt. Im Gegensatz zu den intensiv erforschten Katalysatoren auf Basis von Au-Nanopartikeln sind die katalytischen Prozesse an nicht funktionalisiertem und oxidbeschichtetem np-Au mechanistisch weit weniger verstanden. Quantenchemische Methoden, insbesondere Methoden der Dichtefunktionaltheorie (DFT) können erfolgreich eingesetzt werden, um ein mechanistisches Verständnis auf mikroskopischer Ebene zu erreichen, das notwendig ist für die Optimierung der katalytischen Eigenschaften von Materialien auf Basis von np-Au.

In dieser Dissertation fasse ich meine theoretisch-chemische Arbeit zusammen, die einem tieferen Einblick in die Chemie und Physik von np-Au als Katalysator gewidmet ist. Die moderne Forschung an Oberflächen hat gezeigt, dass ein Katalysator kein starrer Körper ist, sondern während chemischer Prozesse auf seiner Oberfläche schnelle (manchmal irreversible) dynamische Änderungen erfährt. Während viele theoretische Studien immer noch ein stark vereinfachtes Modell eines Metallkatalysators als starre, saubere und perfekte Oberfläche verwenden, untersucht die vorliegende Arbeit dynamische Prozesse auf der Oberfläche von np-Au, die bei Änderungen der chemischen Umgebung ablaufen, mithilfe von Ab-initio-Molekulardynamik (AIMD). Dies umfasst sauerstoffinduzierte Reorganisation der Oberfläche, die Bildung von kettenförmigen Strukturen von Oberflächen-gebundenem Sauerstoff und katalytische Elementarreaktionen auf np-Au. Zusätzlich zu AIMD-Simulationen wurden anhand traditioneller „statischer" DFT-Berechnungen Minima und Übergangszustände in der Reaktionsenergielandschaft verifiziert und Reaktionsenergiediagramme erstellt. Die wichtigsten Ergebnisse der Veröffentlichungen, die die Grundlage dieser Arbeit bilden, lassen sich wie folgt zusammenfassen.

Die Oberfläche von np-Au enthält Spuren von Silber als Rückstand des Herstellungsprozesses, was zur Oberflächenchemie beiträgt. Wechselwirkungen zwischen Au-Atomen und Oberflächen-O-Atomen, die voradsorbiert sind und / oder während der Katalyse erzeugt werden, und die Mitwirkung von Ag-Atomen führen zu einer komplexen Oberflächendynamik. Im Fall von nicht funktionalisiertem np-Au zeigen die theoretischen Studien, dass Oberflächen-O-Atome auf einer gestuften Au(321)-Oberfläche dynamisch ein- und zweidimensionale -(Au-O)- Kettenstrukturen

bilden und zu einer Reorganisation der Oberfläche führen. Im Gegensatz dazu wurde bei Au(111) keine Kettenbildung gefunden, was eine höhere strukturelle Flexibilität und Neigung zur Reorganisation der gestuften Oberfläche aufzeigt. Darüber hinaus legen die Ergebnisse nahe, dass eine Migration von Ag-Atomen aus dem Volumen zur Oberfläche, also eine adsorbatinduzierte Segregation von Ag an der Oberfläche, durch adsorbierten atomaren Sauerstoff ausgelöst wird.

Ein weiterer Schwerpunkt der Arbeit betrifft die Physik und Chemie von mit Ceroxid funktionalisiertem np-Au-Material. Um die Reaktivität dieser Systeme und die Beteiligung von Partikel-Träger-Wechselwirkungen an der CO-Oxidation zu untersuchen, wurden AIMD-Simulationen und statische DFT-Berechnungen durchgeführt. Als Modelle dienten $Ce_{10}O_{20/19}$-NPs auf dem thermodynamisch stabilen Au(111) und auf der gestuften (rauen) Au(321)-Oberfläche. Für das Ceroxid auf Au(111) zeigten die Simulationen die Präferenz eines Reaktionsmechanismus vom Mars-van-Krevelen-Typ, bei dem ein CO-Molekül zuerst mit einem Gitter-O-Atom von Ceroxid und nicht mit einer aktivierten O_2^{2-}-Oberflächenspezies zu CO_2 reagiert, was zu einer Sauerstofffehlstelle führt. Diese Fehlstelle wird anschließend durch ein diffundierendes O-Atom wieder aufgefüllt, das durch Reaktion von O_2 mit einem anderen CO (am Rand der Ceroxid-Nanopartikel) freigesetzt wird. Die Rechnungen zeigen auch, dass im Gegensatz dazu die CO-Adsorption an der abgestuften Au(321)-Oberfläche (in der Nähe des Ceroxid-Nanopartikels) zur dynamischen Extraktion von Au-Atomen von der Oberfläche unter Bildung von Au-CO-Carbonylspezies führen kann, die anschließend auf der Au-Oberfläche diffundieren können und mit O im Gitter von Ceroxid zu CO_2 mit einer sehr geringen Aktivierungsenergie reagieren können. Nach dem Reaktionsschritt bindet das extrahierte ligandenfreie Au-Atom wieder an eine Stufe der Au-Oberfläche. Da dies nicht der ursprüngliche Bindungsplatz ist, führt dieser Teil des Katalysezyklus zu einer Reorganisation der Oberfläche. Der zweite Teil des Zyklus ist sehr wahrscheinlich der gleiche wie für das Ceroxid auf Au(111).

Die vorliegende Arbeit diskutiert auch den Vergleich zweier „inverser" Typen von Katalysatoren , nämlich von Au-Nanopartikeln, die auf Ceroxid abgelagert sind, und Ceroxid-Nanopartikel, die auf Gold abgeschieden sind (und im Mittelpunkt dieser Arbeit stehen), in Bezug auf alle für die Oberflächenreaktivität relevanten Aspekte wie Oberflächendynamik, Ladungstransfer zwischen der Gold- und der Oxidphase und den Mechanismus der CO-Oxidation.

Abstract

Nanoporous gold (np-Au) has recently emerged as a highly selective catalyst, potentially suited to environmentally friendly and low-temperature applications. In contrast to the more extensively studied gold nanoparticle catalysts, the mechanistic understanding of catalytic processes on pristine and oxide-coated np-Au is far less developed. Quantum chemical methods, in particular, those based on density functional theory (DFT) can be used successfully to achieve a mechanistic understanding at the microscopic level, which is needed to optimize materials based on np-Au with respect to their catalytic properties.

In this thesis, I summarize my computational work devoted to a deeper insight into the chemistry and physics of np-Au as a catalyst. Modern surface science has revealed that a catalyst is not a rigid body but undergoes rapid (sometimes irreversible) dynamic changes during chemical processes occurring on its surface. Whereas many theoretical studies still use an oversimplified model of a metal catalyst as a rigid, clean, and perfect surface, my PhD work examines dynamic processes occurring on the surface of np-Au in response to changes of the chemical environment, such as oxygen-induced surface restructuring, the formation of surface oxygen chain structures, and elementary catalytic reactions on np-Au, by using *ab initio* molecular dynamics (AIMD) simulations. In addition to AIMD simulations, traditional "static" DFT computations have been performed to verify minima and transition states in the reaction energy landscape and to construct reaction energy diagrams. The main results of the publications comprising the foundation of this thesis can be summarized as follows.

Although np-Au consists of almost pure gold, silver atoms are also present on the surface as residues of the preparation process. Therefore, its surface chemistry turns out to be more complex than anticipated. Interactions between Au atoms and O atoms pre-adsorbed and/or generated during catalysis and the involvement of Ag impurities result in complex surface dynamics. First of all, with regard to pristine np-Au, the theoretical studies reveal that surface O atoms dynamically form one- and two-dimensional –(Au–O)– chains on a stepped Au(321) surface and lead to surface restructuring. In contrast, no chain formation has been found on Au(111), pointing to higher structural flexibility and propensity for restructuring of the stepped surface. Furthermore, our study predicts migration of subsurface Ag atoms to the surface, i.e. adsorbate-induced Ag surface

segregation, in the presence of adsorbed atomic oxygen.

Second, my thesis addresses the physics and chemistry of np-Au material functionalized with cerium oxide. To probe the reactivity of these systems and the involvement of inherent particle-support interactions towards CO oxidation, AIMD simulations and static DFT computations were carried out. As models, $Ce_{10}O_{20/19}$ NPs supported on thermodynamically stable Au(111) and on the stepped (rough) Au(321) surface were employed. For the ceria/Au(111) system, the simulations revealed the preference of a Mars-van-Krevelen type of reaction mechanism, in which a CO molecule first reacts with a lattice O atom of ceria rather than with an activated O_2^{2-} surface species, forming CO_2 and leaving an O vacancy behind. This vacancy becomes subsequently refilled by an O atom which diffuses from the site of the reaction of O_2 with another CO molecule (at the gold-ceria perimeter). My studies also revealed that, in contrast, CO adsorption on the stepped Au(321) surface (in proximity to the ceria nanoparticle) may lead to the dynamic extraction of Au atoms from the surface resulting in Au-CO carbonyl species, which may subsequently diffuse on the Au surface and react with lattice O of ceria to CO_2 with very low activation energy. After the reaction step, the extracted bare Au atom attaches to a step on the Au surface. As this is not the original site, this part of the catalytic cycle leads to a rearrangement of the surface structure. The second part of the cycle is likely to be the same as found for the ceria/Au(111) system. Finally, this thesis discusses the correlation between two types of catalysts that are "inverse" with respect to each other, namely, Au nanoparticles deposited on ceria and ceria nanoparticles deposited on Au (being the focus of this thesis), with respect to all aspects relevant for the surface reactivity, such as surface dynamics, charge transfer between the gold and the oxide phases, and the mechanism of CO oxidation.

Contents

ix

Chapter 1 Introduction

1.1 Catalytic Activity of Gold Nanoparticles from Electronic Structure Perspective

Gold possesses an electronic configuration [Xe] $4f^{14}5d^{10}6s^1$ and is one of the elements, for which relativistic effects are particularly large. The relativistic effects in gold cause strong contraction (and, therefore, energy lowering) of the valence $6s$ (and to a lesser extent $6p$) shell, as seen from **Fig. 1.1**, thus resulting in greater ionization energy than it would be without consideration of relativistic effects and high electronegativity comparable with iodine.[1-2] As an indirect influence of relativistic effects, the $6s$ and $6p$ contraction shields the electrons in fully-occupied $4f$ and $5d$ shells, further bringing them closer in energy to the $6s$ level (or the Fermi level, if we are talking about metallic gold). This influence leads to a reduction of the $6s$-$5d$ energy gap, which gives rise to the yellow color of gold ($5d$ to Fermi level transition lies in the blue region of the visible light spectrum). The strong relativistic effects make gold a unique element.
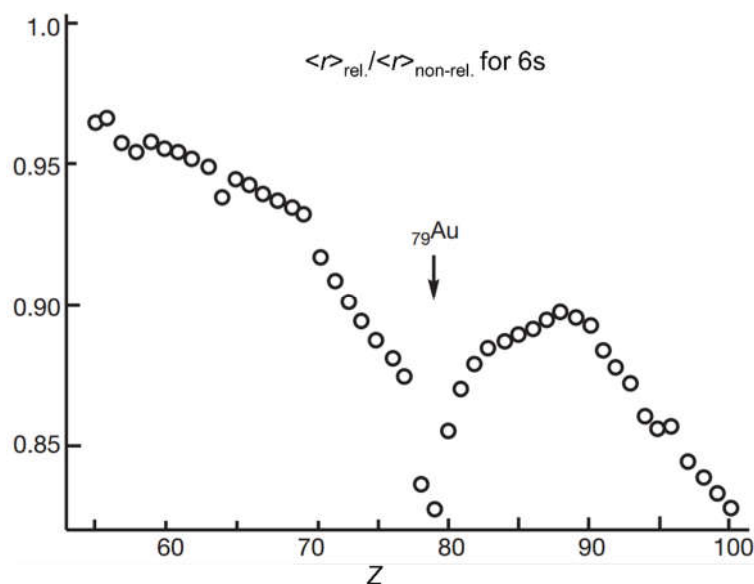
Fig. 1.1 The theoretically computed relativistic contraction of the 6s shell is given by the ratio of relativistic radius to the non-relativistic radius. (Reproduced from refs. 1-2, with permission from the American Chemical Society.)

Gold usage in catalysis started to attract increasing attention after the pioneering work of Haruta et al., who demonstrated an outstanding low-temperature catalytic activity of nano-sized Au particles supported on metal oxides for CO oxidation.[3] In the

subsequent studies, free, ligand-stabilized, and oxide-supported gold NPs have been found to demonstrate catalytic activity.[4-8] In recent decades, numerous experimental and theoretical studies have aimed to elucidate the origin of the catalytic activity of nano-sized gold catalysis and to provide direct insights into the reaction mechanisms. Currently, most authors agree that there may be several effects, contributing to the special activity of supported Au NPs. These effects include small size and associated quantum-size effects, the shape of gold nanoparticles, the abundance of surface Au atoms with low coordination number, and effects related to interaction with the support, such as charge transfer between gold and the support and/or the chemical involvement of the support in the reaction mechanism. The catalytic activity of oxide-supported Au NPs for CO oxidation with O_2 in the gas phase significantly correlates with the Au particle size. In general, catalytically active Au NPs are smaller than 5 nm in diameter.[6] Gold NPs were reported to lose their catalytic activity toward CO oxidation when their shape changed from icosahedron or face-centered cuboctahedron to decahedron.[9] Numerous experimental and theoretical studies suggested that the active centers of gold nanoparticle catalysts are low-coordinated gold atoms, which facilitate the activation of O_2 and CO adsorption.[10-15] On some supports, strong metal-support interaction (SMSI) may significantly affect the catalytic activity of nano-sized gold particles, e.g., through a charge transfer between the Au nanoparticle and the support and charge accumulation at the Au-support interface; reducible support can even participate in the catalytic cycle and supply active oxygen atoms.[16-25]
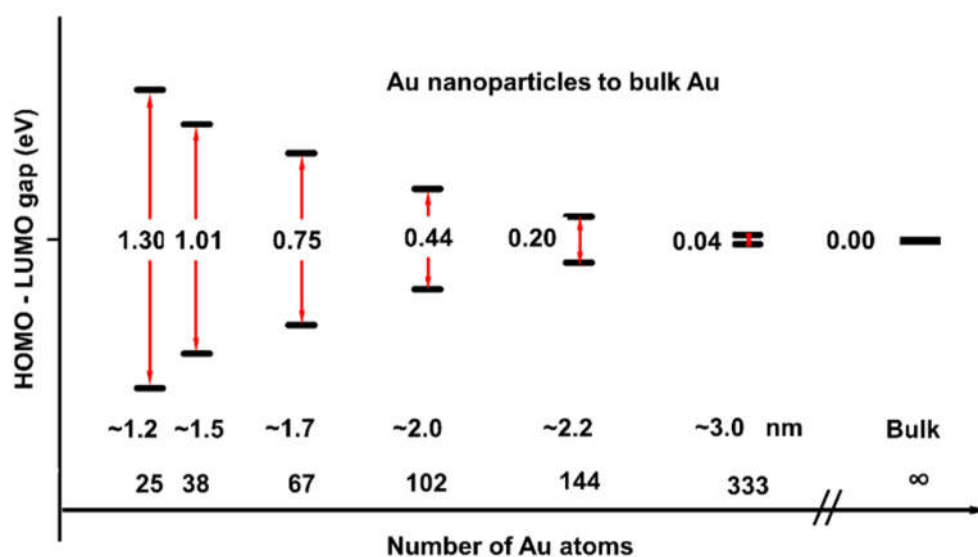

Fig. 1.2 The gaps between the highest occupied molecular orbital and the lowest unoccupied molecular orbital (HOMO−LUMO gaps) decrease with increasing cluster size. The data were taken from literature.[26-29]

2

Bulk gold is notorious for being catalytically inert and highly conductive. Like any other metal, it has a zero band gap. By decreasing the size of a gold object from a macroscopic piece of metal (bulk gold) to a nano-sized particle, the energy levels transform from continuous energy bands to discrete orbital energies due to quantum size effects. In comparison to bulk gold with its zero band gap, the HOMO-LUMO gap of catalytically active gold NPs gradually decreases from 1.3 to 0.04 eV with increasing the number of Au atoms in the nanoparticle from 25 up to 333, as shown in **Fig. 1.2**. For gold NPs, relativistic contraction of the 6*s* shell, together with an upward shift of the 5*d* shell to the frontier orbitals, leads to a reduction of the *s-d* energy gap resulting in the hybridization (mixing) of the 5*d* and 6*s* orbitals, thus partially depopulating 5*d* states.[30-31] As a result, gold exhibits strong covalent bonding.[1-2] Recently, a theoretical study suggested that the catalytic activity of nanostructured gold can be explained by the appearance of so-called "*σ*-holes" (i.e., maxima in the surface electrostatic potential), at low-coordinated gold atoms, due to the overlap of singly occupied *s*-orbitals.[32]

The mechanistic details of the catalytic activity of supported Au NPs are still being debated. A substantial body of experimental and theoretical evidence suggests that key reaction steps, such as the activation of adsorbed O_2, occur at or close to the interfacial perimeter between the Au nanoparticle and the support but there are a number of different propositions regarding the exact sequence of elementary steps and the nature of the involvement of the oxide support (via surface hydroxyl groups, redox reactions on the support or charge transfer). We will not attempt to summarize the existing literature here but we refer the reader to recent reviews.[7, 33] In Chapter 3, we will discuss the current literature and state of knowledge regarding the mechanisms of CO oxidation on ceria-supported Au NPs.

1.2 Nanoporous Gold: A Monolithic Catalytically Active Form of Gold

Nanoporous gold (np-Au) has recently emerged as a catalyst showing high activity for low-temperature CO oxidation.[34-35] The three-dimensional bicontinuous structure of np-Au is comprised of nanopores and ligaments with a size of about tens of nm.[36] That is apparently larger than the typical size of catalytically active Au NPs, of 5 nm and

below. A wide range of interesting reactions in gas and liquid phases, from CO oxidation to more complex organic transformations have been catalyzed by nanoporous gold due to its remarkable catalytic activity and high selectivity.[37-39] However, the broader use of np-Au as a catalyst has been restricted due to thermal coarsening and a loss of specific surface area at temperatures of 200-300 °C in reactive atmospheres.[40] In addition, adsorbate-enhanced surface atom diffusion can also increase the tendency of coarsening of the nanoporous network.[36, 41-43] Theoretical and experimental explanations for the unexpected catalytic activity of np-Au have been proposed, including the role of low-coordinated surface Au atoms,[44] the involvement of noble metallic impurities (inherently present as residuals after dealloying from an Au-Ag or Au-Cu alloy),[45-47] and the not quite well-characterized chemisorbed-oxygen on its surface, possibly forming O phases.[48] A high-resolution scanning transmission electron microscopy study by Fujita group recently revealed the atomic structure of np-Au ligaments, **Fig. 1.3**, and has demonstrated a high density of low-coordinated Au atoms associated with steps and kinks on the curved surface of np-Au ligaments, comparable to that of 3-5 nm Au NPs.[44] Hence, the high density of low-coordinated Au atoms is a common feature of Au NPs and np-Au. In line with that, some of the authors attributed the origin of the catalytic activity of np-Au to the low-coordinated Au atoms, especially in the early years after the discovery of the catalytic activity of this material. Later on, theoretical and experimental studies suggested that Ag and Cu residuals likely exert notable influence on the surface structure and catalytic properties of np-Au by facilitating the O_2 adsorption and activation.[45-47] It was theoretically predicted that adsorbed atomic oxygen may play important role as reactive or spectactor species influencing the activity of np-Au in airobic oxidation reactions.[49-50] Recent *in situ* electron microscopy studies by Fujita et al.[41] and by Friend et al.[51] revealed dynamic restructuring of np-Au induced by chemical reactions and CO adsorption. In a surface-science study using high-resolution photoelectron spectroscopy along with other techniques, Schaefer et al.[52] observed Ag enrichment in the surface region of np-Au after ozone treatment and the depletion of Ag surface content after a subsequent reduction treatment using CO. According to a recent theoretical study by our group using Au(321) as a model for np-Au[48], –(O–Au)– chain structures, represent the thermodynamically most stable form of adsorbed surface oxygen on gold at low O coverage. Previously, Fajín et al.[53] studied oxygen adsorption behavior on Au(321) and

identified the most favorable adsorption sites. They also investigated surface restructuring at high O coverage by considering different arrangements of O adsorption sites.[54] Although these authors did not specifically look for the formation of –(O–Au)– chains, the lowest-energy structures identified in their study[54] contain structural motifs with linear O–Au–O units connected in infinite chains. Similar findings were earlier described in other theoretical studies of O adsorption on Au(111)[55] and Au(110).[56] A few years later an experimental TEM study finally provided evidence confirming the existance of O chains on the Au(110)-(1 × 2) surface exposed to ozone.[57] The –(O–Au)– chains were found to be significantly stabilized as compared to individually adsorbed O atoms, by ~0.15 eV per O atom, whereas in the case of analogous –(O–Ag)– chains, the energy gain is much smaller.[48]
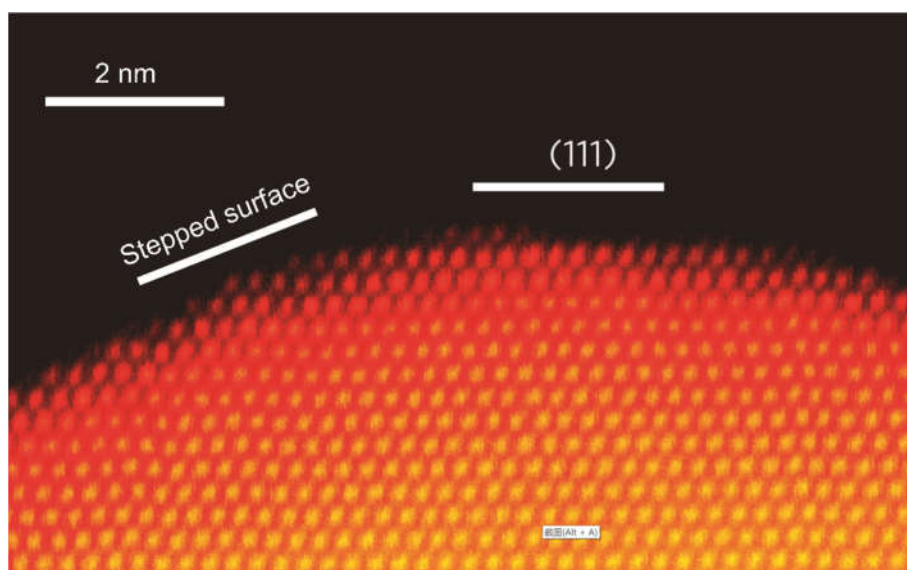

Fig. 1.3 Low-coordinated Au atoms at steps and kinks of an np-Au ligament. Reproduced from ref. 39, with permission from Nature Publishing Group.

1.3 Catalytic Activity of Oxide-Functionalized Nanoporous Gold

Metal oxides are widely used in catalysis either as active components or as supports for nanoparticles of a metallic catalyst. Because catalytically active metals are usually very expensive, anchoring them on a less expensive support material with a high-surface-area allows for more effective usage of the active component, increases the effective surface area of the catalyst and gives mechanical stability to catalyst nanoparticles. In

many cases it has been suggested that supports affect the properties of a catalyst. These effects could be either of physical nature, e.g. different adhesive properties of different supports or the support may transfer some charge to or from a metal nanoparticle, or in some cases the catalyst could be even chemically modified (oxidized or reduced, especially at the interface between the metal particle and the support). In some catalytic processes an oxide support may also directly participate in the catalytic cycle, as some parts of the cycle occur on the support or at the boundary between the support and the metal particle. Reducible oxides, like ceria or titania, can for certain reactions be active catalysts on their own due to their excellent redox properties. They are also used as supports for metallic catalysts and the resulting composite catalyst benefits from properties of both metal and oxide components. In particular, ceria has been widely used in catalysis due to the easy formation and diffusion of oxygen vacancies, high capacity of oxygen storage and release, and facile acceptance/release of electrons in oxides surface.[58-59] The synergistic catalytic effects, such as interaction between the components (support and nanoparticle) of a composite catalyst, significantly enhance the catalytic performance as compared to the individual components.[60] Catalytic applications of oxide-supported Au NPs, an exemplary system illustrating a synergistic effect between the Au NPs and the support, have attracted tremendous research interest. As an inverse system with respect to oxide-supported metal NPs, in which CeO_2 and TiO_2 NPs are supported on metal surfaces (Au and Cu), has been developed by Rodriguez and co-workers, who investigated the synergistic effect between the two components and demonstrated that the metal-support synergy enhances the catalytic performance of such an inverse catalyst.[61-62] While Rodriguez et al. developed model catalysts in which ceria nanoparticles were supported on flat metal surfaces, it is possible to make a step forward toward practical applications of such catalysts by replacing a flat metal surface with a porous metallic framework. This novel form of an inverse catalyst has been realized through the deposition of nano-sized oxide particles (TiO_2, Al_2O_3, or CeO_2) on np-Au. Such an oxide coating was found to significantly improve the thermal stability of np-Au up to temperatures of 600°C and above by improving resistance of its nanopores and ligaments to coarsening.[36, 63-65] At the same time, functionalizing np-Au with reducible oxides enhances its catalytic activity compared to pristine np-Au.[36, 63-65] In the case of reducible oxides, the formation and refilling of oxygen vacancies (denoted as O_V hereafter) is facile; the involvement of lattice oxygen opens new catalytic pathways enabling new types of reactions, not

catalyzed by pristine np-Au.[63, 66] The resulting composite oxide/np-Au catalysts were found to be active for a few industrially relevant chemical reactions, e.g. the water-gas shift reaction,[66-67] NO reduction[63] and steam reforming of methanol,[68] for which pristine np-Au is not catalytically active. This dissertation focused on ceria as a coating material for np-Au. The system comprised of ceria NPs deposited on np-Au shows very promising catalytic properties, which have been partly ascribed to the easy formation of oxygen vacancies in ceria.[66-68] as well as to a synergistic action of the nanostructured metal and the oxide at particle boundaries. In related experimental studies by Bäumer group, a high concentration of O vacancies was inferred from studying the Ce^{3+}/Ce^{4+} ratio with X-ray photoelectron spectroscopy.[66-68] This finding is consistent with the relatively high experimentally measured concentration of Ce^{3+} ions (18%) in 3 nm ceria NPs supported on silica aerogel, as determined with electron magnetic resonance (EMR) spectroscopy and magnetization studies.[69] Oxygen vacancies in the Au-supported cerium oxide NPs have been suggested to play a key role in the catalytic activity of such catalysts.[66] These findings are in line with numerous studies on ceria-supported Au NPs (Au/ceria), which have been investigated for a much longer time than the inverse system ceria/np-Au. Au NPs supported on CeO_2 have been intensively studied with regards to many aspects, including their catalytic properties and mechanistic details, of catalytic reactions, the chemistry and physics of the Au/oxide interface, and the charge transfer between the gold and the oxide.[70-73] The influence of interface dynamics, charge transfer and synergistic catalytic pathways for ceria-supported Au NPs has been discussed to explain the catalytic activity of such systems.[70-74] It is generally recognized that the Au–oxide interfacial perimeter plays an important role for the catalytic activity.[74-77] The reactivity of such catalysts is affected by the structural and electronic properties of Au NPs, the interaction between gold, the support, and adsorbates. The environmental transmission electron microscopy analysis[78] revealed that gold NPs on CeO_2 support change their shapes at the interfacial area in response to alternating oxidizing and reducing atmospheres. However, in contrast to oxide-supported Au NPs, the theoretical studies of oxide NPs supported on Au are rare; thus, the mechanistic details of oxidation reactions taking place on such inverse catalysts still remain unclear. Before this work, to the best of our knowledge,[71,72, 79] only one computational study published by Kim and Henkelman addressed Au supported ceria nanoparticles theoretically. The authors studied O vacancy formation energy at the Au−CeO_2 interface using small ceria clusters (Ce_5O_{10} and Ce_9O_{18}) supported on

7

Au(111).

1.4 Aims of this Dissertation

Because nanoporous gold is usually prepared via a chemical dealloying of an Au-Ag alloy, its nanostructured surface remains in a metastable state with high surface energy and dense surface defects. The first part of this work, summarized in Chapter 2, aimed to explore and understand the atomic rearrangements, bonds breaking/formation, and atomic diffusion during the process of surface restructuring in the np-Au system under the influence of the oxygen-containing atmospheres. The stepped and kinked Au(321) surface featuring zigzag-shaped steps with 6-and 8-fold low-coordinated Au atoms at steps as well as narrow terraces of (111) type was chosen to represent rough and flat structural motifs of the nanoporous gold surface. With this Au(321) surface model, *ab initio* molecular dynamics (AIMD) simulations were carried out to reveal the equilibration process at the atomic level in the presence of surface defects, chemisorbed O atoms, and Ag impurities on the surface and in subsurface layers of np-Au.

Although the np-Au catalyst is prone to thermal instability under elevated temperatures and upon exposure to reactive atmospheres (e.g. CO + O_2), as already mentioned in Section 1.2, deposition of ceria nanoparticles on np-Au improves its resistance to coarsening and boosts the activity. Theoretically, such composite catalysts have been studied to a far lesser extent as compared with their inverse counterparts, the ceria-supported gold nanoparticles. To the best of our knowledge, publications III and IV of this dissertation represent the first theoretical mechanistic studies about CO oxidation on the inverse ceria/gold system. These publications have been summarized in Chapters 3 and 4 of the thesis. By using the computational models $Ce_{10}O_{19/20}$/Au(111) and $Ce_{10}O_{19/20}$/(321), this theoretical work pursued the following specific objectives: (i) to identify the most stable geometry of the ceria/np-Au system, (ii) to study oxygen vacancy formation and defect chemistry, (iii) to investigate the origins of the high thermal stability of the np-Au substrate coated with ceria, (iv) to characterize the structural dynamics associated with the charge transfer between the Au and the ceria NP, and (v) to study the mechanism of dioxygen activation and CO oxidation, (vi) to elucidate the catalytic mechanism and the origins of a higher catalytic activity compared to pristine np-Au.

Chapter 2   Oxygen-Driven Surface Dynamics of Nanoporous Gold

Chapter 2 summarizes the results of publications I and II, which contributed to our knowledge about the surface composition of np-Au from the thermodynamic and dynamic perspective. As mentioned above, np-Au material contains a small amount of Ag impurities, which, nevertheless, exhibit a strong effect on its chemistry, as it has by now been evidenced by various experimental and theoretical studies.[45, 48-49, 80-81] Oxygen atoms in the surface region of "as-prepared" and activated np-Au in at least three different chemical states have been identified in the near-surface region by XPS and may have been incorporated in the material during its fabrication through dealloying.[52] The O atoms can also be generated during a catalytic reaction on np-Au or deposited to the surface deliberately (e.g. by ozone treatment). Atomic oxygen species are expected to play a crucial role in aerobic oxidation reactions catalyzed by gold.[48, 80] At the same time, the supply and consumption of surface O may cause restructuring and redistribution of Ag impurities within the surface.[82] Therefore, studying the surface evolution of gold in the presence of O atoms should help to better understand the interplay between gold, oxygen and silver impurities during the catalysis. The Ag enrichment in the surface region of np-Au after ozone treatment and depletion of Ag surface content after a reduction using CO have been observed using high-resolution photoelectron spectroscopy along with other surface–science techniques.[52] One can anticipate that such change is caused by oxygen-driven diffusion of silver. Hence, the first objective of this chapter is to characterize the structural rearrangements in the surface region associated with the mentioned O and Ag diffusion processes; and the second aim is to find out whether Ag diffusion in the top surface layer or from subsurface layers to the surface could be induced by oxygen adsorbates. This chapter reveals the formation of oxygen chain structures on gold and oxygen-driven silver diffusion and segregation by applying *ab initio* molecular dynamics (AIMD) simulations and static DFT computations on the theoretical model of Au(321) surface, providing deeper insight into the surface restructuring processes of nanoporous gold.

2.1 Formation of Oxygen Chain Structures on a Stepped Gold Surface

The gold-oxygen chain structures comprised of linear O–Au–O units with a significant degree of directional covalent bonding were first predicted by using density functional theory on Au surfaces,[55-56] and a recent experimental TEM study evidenced the possible presence of such chain structures on O sputtered Au(110).[57] The results of our AIMD simulations published in papers I and II provide atomic-level insight into the details of the dynamic chain formation process on Au and bimetallic Au-Ag surfaces. The AIMD simulation is a method that can mimic the atomic thermal motion of a real system, allowing the system to equilibrate to thermodynamically stable states via diffusion or reactions. Numerous intermediates, transient structures, transition states, byproducts and products, not necessarily foreseen before starting the simulation, can be sampled, such as complex surface rearrangements involving multiple atoms. Approximate transition states and minima identified in a simulation can then be refined by conventional DFT optimization. A simulation (**Fig. 2.1**) was carried out using a model of the Au(321) surface with five individually adsorbed O atoms per (3×2) unit cell corresponding to a coverage of 0.17 ML. The dynamic evolution of surface restructuring and chain formation was simulated at 700 K for 22 ps. Note that the relatively high simulation temperature used in our AIMD simulations was chosen for technical reasons, as described in Chapter 7.

This simulation (**Fig. 2.1**) revealed the formation of a –(Au–O)– chain structure mainly via diffusion of O atoms and accompanied by relatively large displacements of adjacent Au atoms on Au(321) surface. Driven thermodynamically (as the process is exothermic), the first –O–Au–O– chain fragment is formed during the first 7 ps. This rearrangement involves migration of O and Au atoms, as well as lifting of certain Au atoms from the terraces. During the next 7 ps of the simulation, O(**7**) migrates and attaches to Au(**6**) and Au(**8**) forming a long chain structure. The long-chain formed remains stable to the end of this simulation at 22 ps; therefore, one can assume that the simulation has approached a relatively deep stable minimum. This AIMD simulation demonstrated that surface O on a stepped Au surface tends to form chain structures.
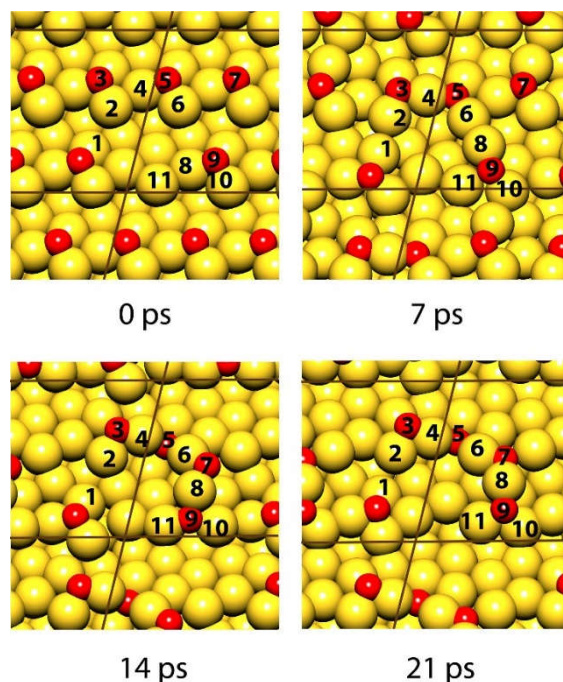
Fig. 2.1. Snapshots of an AIMD simulation showing a -(Au-O)- chain formation from individually adsorbed O atoms on Au(321) without Ag impurities. (3×2) unit cell and O coverage of 0.17 ML. Color coding: Au, yellow; O, red. (Reproduced from Publication II, with permission from the American Chemical Society.)

The AIMD simulation described above has shown that chain formation from individually adsorbed O atoms is thermodynamically favorable. This is in line with the static DFT calculations of the formation of a chain fragment as shown in **Fig. 2.2**, in which the chain formation barrier and energies were estimated. The migration of O forming the first chain is slightly exothermic (MIN). The chain fragment becomes almost linear in the final state (FS) releasing 0.18 eV energy with respect to the initial state (IS), implying a thermodynamically favorable process. A very low activation barrier of 0.35 eV for the formation of the first chain implies that it should be very easy to overcome even at room temperature. As compared to the regular values, both shortened Au–O and Au–Au bonds (~2.14-2.17 and 2.85-2.92 Å, respectively) within the chain (for values see **Fig. 2.2**) imply stronger bonding interaction within a chain. Two additional pathways for the formation of a short –O–Au–O– chain starting from different initial arrangements of O atoms were calculated, **Fig. 2.3**. Both of them show the activation barrier below 0.5 eV and are slightly exothermic as well, implying that the chain formation is thermodynamically favorable.
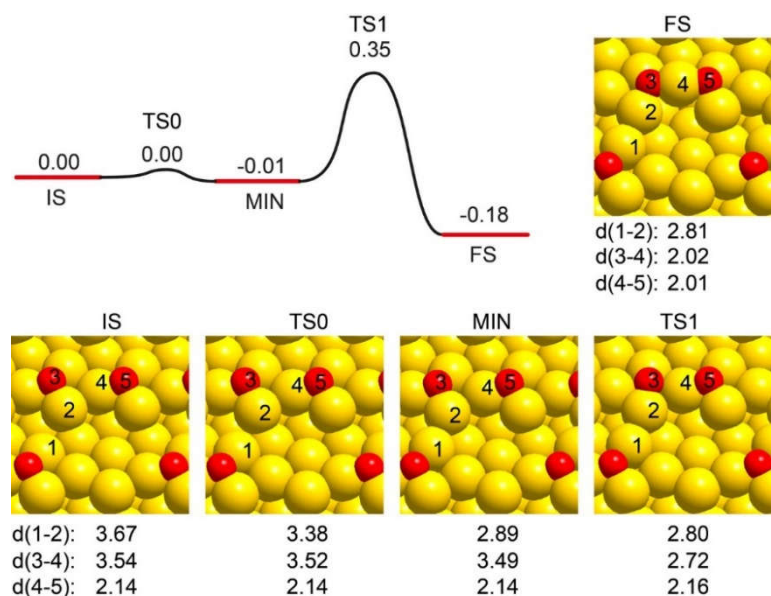
Fig. 2.2. First steps of the chain formation. (2×2) unit cell and O coverage of 0.15 ML. Energies are in eV, bond distances in Å. Color coding: Au, yellow; O, red. (Reproduced from Publication II, with permission from the American Chemical Society.)

Fig.2.3. Possible reaction paths for a short-chain formation on Au(321). Energies are in eV, bond distances in Å. Color coding: Au, yellow; O, red. (Reproduced from Publication II, with permission from the American Chemical Society.)
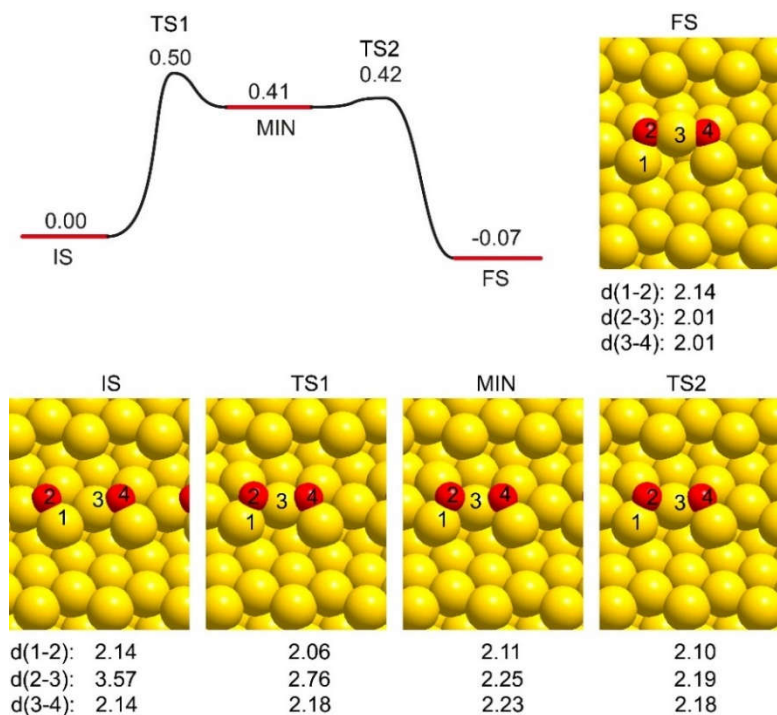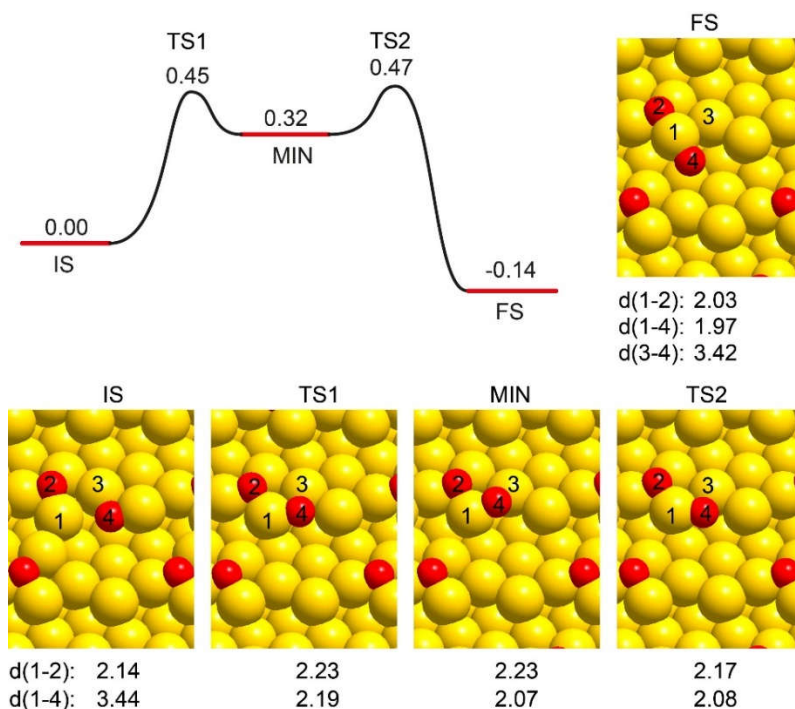
Fig. 2.4. Continued from Fig. 2.3. (Reproduced from Publication II, with permission from the American Chemical Society.)

In the course of the AIMD simulation described above, the chains started to form along the step edges of the Au(321) surface, characterized by a high density of low-coordinated Au atoms. One can expect that a chain formation could be facilitated on a surface with low-coordinated atoms (the Au atoms near or at the step edge). To verify this, the formation of chains at the flat Au(111) surface starting from a similar initial O coverage was studied as well, **Fig**. **2.5**. The surface with adsorbed O atoms remained unchanged and no chain formation was observed after 24 ps of an AIMD simulation, confirming the crucial role of steps and low-coordinated atoms for the facile kinetics of chain structure formation. Therefore, one can expect the formation of chain structures on the surface of nanoporous gold, which should be facilitated by its high density of steps and low-coordinated Au atoms.[44]
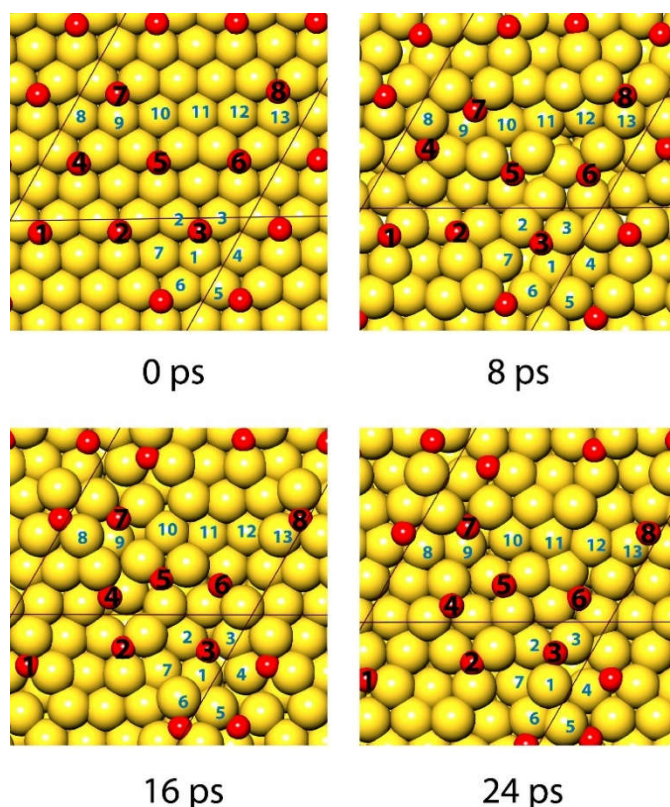
Fig. 2.5. Snapshots of an AIMD simulation showing surface evolution of Au(111) with individually adsorbed O atoms initially occupying 3-fold fcc sites. (6×6) unit cell and O coverage of 0.22 ML. Color coding: Au, yellow; O, red. O atoms and selected Au atoms are marked with numbers. No linear O-Au-O fragments have been formed after 24 ps of the simulation at 700 K. (Reproduced from Publication II, with permission from the American Chemical Society.)

2.2 Effect of Silver Impurities on the Formation of Metal-Oxygen Chains

Approximately 1-5% of silver impurities remain in nanoporous gold as a result of incomplete leaching of Ag from the AuAg alloy. It was reported that Ag impurities may facilitate the adsorption of O_2, and may lower its dissociation barrier to atomic O, providing active O species for oxidation reactions on the bimetallic Au-Ag surfaces.[45, 48] It was also found that the concentration of silver in the surface region is even higher than in the bulk (6-20 atom%) and may increase if samples are exposed to air long enough,[52, 83] which renders silver an important constituent to contribute to the catalysis and surface chemistry of np-Au. Therefore, the influence of Ag impurities to the surface reconstruction and chain formation was explored in this chapter.
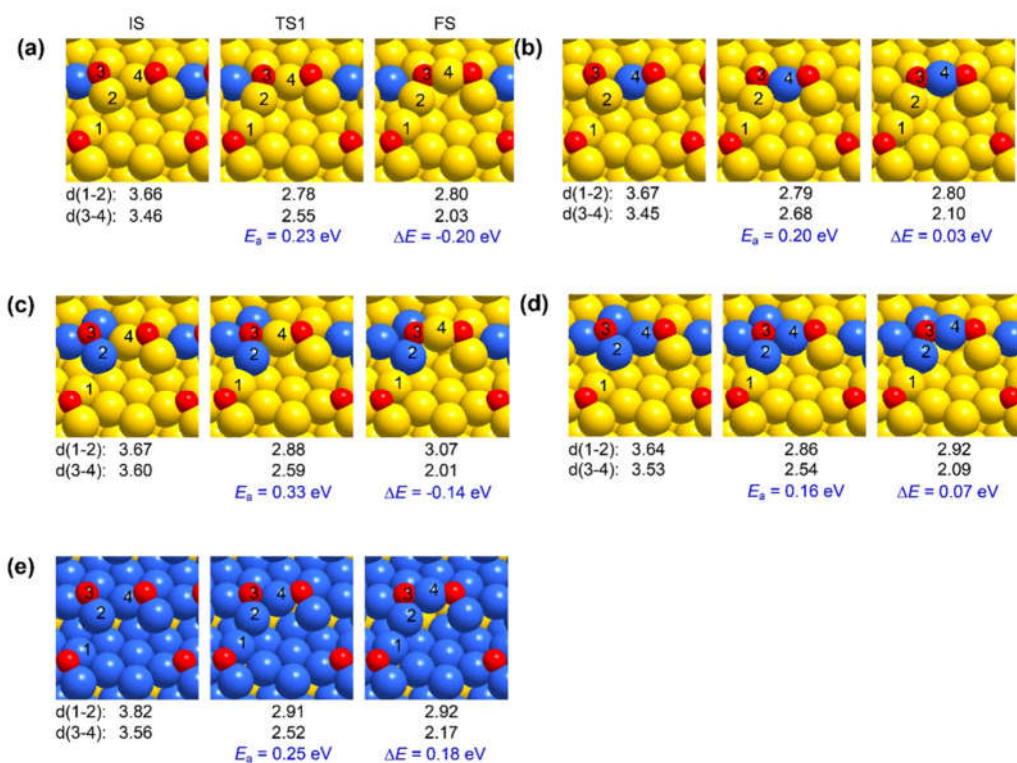
Fig. 2.6. Effect of Ag impurities on the –O–M–O– chain formation (M = Au, Ag). The O coverage is 0.15 ML. One (a, b), three (c), four (d), or twenty (e) Ag atoms per unit cell are substituting the Au atoms in the top layer. Energies are in eV and are referenced to the energy of the initial state (IS). The bond distances in Å. Color coding: Au, yellow; Ag, blue; O, red. (Reproduced from Publication II, with permission from the American Chemical Society.)

The effect of Ag impurities on the barriers and energy of –O–Au–O– chain formation was investigated along the same reaction path and with the same initial arrangement of adsorbed O atoms as on pure Au(321). The results are shown in **Fig. 2.6**. Five possible arrangements of Ag atoms with respect to adsorbed oxygen atoms were investigated. Computations reveal that Ag impurities generally lower the activation barrier for the migration of O atoms, which leads to the formation of a short O–M–O chain. In the case where the migrating O atom is completely surrounded by Ag atoms (**Fig. 2.6d**), the barrier reduces to only ~0.16 eV. The formation of a -O–Ag–O– chain is in all cases (**Fig. 2.6b**, **d** and **e**) a slightly endothermic process implying that it is thermodynamically unfavorable. However, the –O–Au–O– chain formation was found in all cases to be exothermic and thus thermodynamically favorable. The most favorable chain formation with the reaction energy of -0.20 eV, was found in the case (**Fig. 2.6a**), where a single Ag atom is bound to the migrating O atom but is not part of the formed chain structure. In related work (Publication I) we investigated the role of silver in stabilizing the –(Au–O)– chain structures by means of cluster expansion

methodology.[84] Consistently with the present results, we found that –(Au–O)– chain structures on a bimetallic Au-Ag surface are thermodynamically most favorable if Ag impurity atoms are located near to chains but not inside a chain. A similar phenomenon is found here (a and c). If Ag atoms surround a chain structure but are not part of a chain, the chain formation is especially energetically favorable. We proposed the following explanation for this phenomenon. The ionic component in the bonding interaction between Ag and O atoms favors high-coordination structure (adsorption at 3-fold sites), at the same time, the covalent component favors a linear O–Ag–O arrangement with the most efficient orbital overlap. In the case of an O–Au–O chain, the component of covalent interaction is stronger, as supported by electronic localization function analysis;[84] thus, the formation of linear O–Au–O structures is energetically favorable. When all top-layer Au atoms are replaced by Ag (**Fig. 2.6e**), the formation of the –O–Ag–O– chain is endothermic with the reaction energy of +0.18 eV; the barrier to IS was computed as 0.25 eV. Both reaction energy and barrier suggest that silver alone should not form chains.

2.3 Oxygen-Driven Ag Segregation Revealed by Molecular Dynamics

By using high-resolution X-ray photoelectron spectroscopy (XPS) and other surface–science techniques to study the oxidation and cleaning of nanoporous gold,[52] Ag enrichment in the surface region after an ozone treatment and a depletion of Ag surface content after a reduction using CO were observed. These changes were attributed to the preferential formation of surface Ag–O bonds than Au–O bonds and Ag diffusion in the surface region driven by the high or low concentration of surface O. The diffusion and segregation of Ag impurities in nanoporous gold plays an important role in catalysis, especially for O_2 adsorption and activation.[48] In an experimental characterization of catalytically active np-Au samples using temperature-programmed desorption (TPD) and XPS, both surface O and Ag impurities were found to be present in the surface region of nanoporous gold ligaments.[83] The study of Ag segregation on the stepped Au(332) surface with Ag impurities by Auger electron spectroscopy shows that atomic oxygen is able to induce Ag segregation already at 200 K.[82] The result of the latter study is in line with the mentioned above oxygen-induced Ag surface segregation in nanoporous gold.[52] The observed Ag segregation indicates that such processes have to

be considered in studying the catalytic reactions on np-Au performed above 200 K. Although the on-surface (and possibly subsurface) oxygen is probably present only in low concentration in np-Au during catalysis, it probably influences the physicochemical properties of the catalyst, in particular, it attracts Ag to the surface, which is required for O_2 adsorption and activation, a key step in aerobic oxidation reactions.

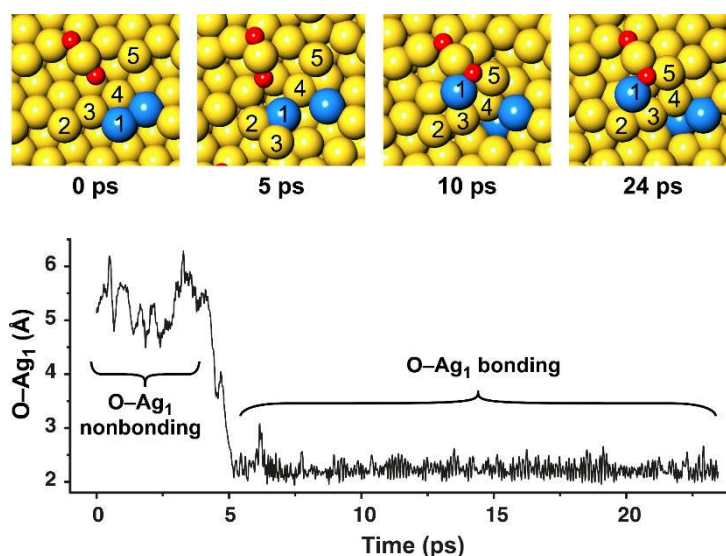In line with the experimental findings, our AIMD simulations discussed below

Fig. 2.7. An AIMD simulation of Ag migration from a kink site to an O–Au–O chain on the surface. Color coding: Au, yellow; Ag, blue; O, red. Some atoms are labeled with numbers for clarity. The Ag_1–O distance between the migrating Ag_1 and the nearest O atom of the chain is plotted as a function of time. (Reproduced from Publication I, with permission from the American Chemical Society.)

predict surface diffusion of Ag impurities caused by adsorbed surface oxygen. Here, we distinguish between two types of Ag diffusion in the surface region. The first one is the lateral migration of Ag in the top layer and the second is vertical Ag migration from subsurface sites onto the surface. The first type of Ag diffusion has been elucidated using an AIMD simulation, as shown in **Fig**. **2.7**, where an Ag atom occupying a kink site of a lower terrace migrates toward the O–Au–O chain and forms a bond with oxygen after 5 ps equilibration, as seen from the bond distance. At the same time, the Au(5) atom at a kink site of the upper terrace detaches from its position and diffuses toward the O atom of the chain. The AIMD simulation reveals that adsorbed O atoms (arranged in short O-Au-O chain structures) facilitate Ag diffusion on the surface. It is worth noting that the O–Au–O chain behaves as a rigid unit during the entire surface reconstruction in an AIMD simulation. The O–Au–O chain slightly changes its

orientation during the thermalization. However, its linear structure and connectivity remain unchanged, supporting the conclusion that the Au–O bonds within the chain are stronger than the external Au–O bonds.
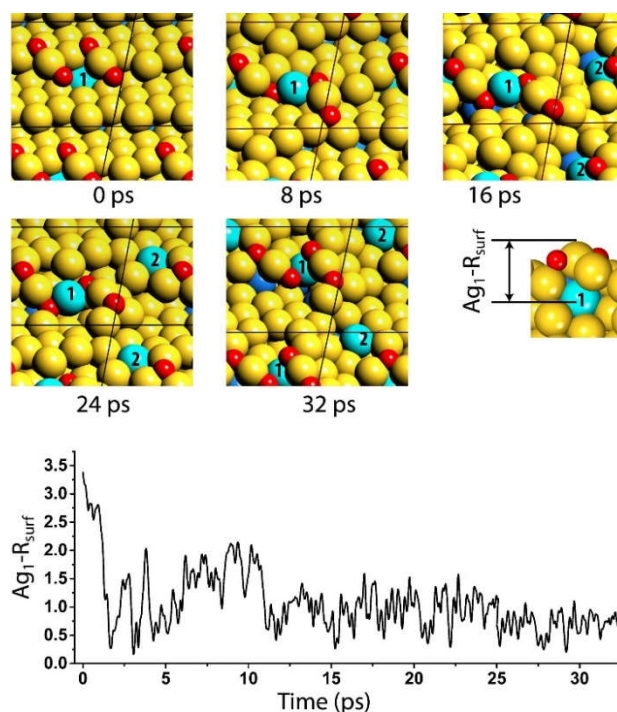

Fig. 2.8. An AIMD simulation showing vertical Ag diffusion from a subsurface layer to the surface. Ag_1-R_{surf} represents the distance of Ag(**1**) atom initially located near the step edge to a reference surface and is plotted as a function of the simulation time. R_{surf} denotes a reference surface that is chosen as a surface plane normal to [321] direction crossing the Z-axis slightly above the Au atom of the O-Au-O fragment at 0 ps and is kept fixed during the simulation. (Reproduced from Publication II, with permission from the American Chemical Society.)

To address the vertical Ag migration, an AIMD simulation in **Fig**. **2.8**, was started from a theoretical model in which 16 Au atoms were replaced by Ag atoms at subsurface positions under the two adjacent O–Au–O structures. A short O–Au–O fragment represents the simplest possible chain; thus, it should be a stable structure on the surface, since such short chains are energetically more favorable than individually adsorbed O atoms. The AIMD simulation (**Fig. 2.8**) shows vertical Ag diffusion from a subsurface layer to the surface as a result of thermal equilibration. **Fig. 2.9** illustrates that in the course of the same simulation a Ag atom located deeper inside the subsurface, labeled as Ag(**2**), which is initially ~4 Å away from the nearest adsorbed oxygen atom, also migrates toward the surface and finally finds itself in the top surface layer. This diffusion occurs at ~14 ps of the AIMD simulation. At the end of the simulation, the distance of Ag(**2**) to the surface, Ag-R_{surf}, decreases from ~4 to ~0 Å, indicating that

Ag(**2**) has migrated onto the surface. **Fig**. **2**.**9** also shows the coordination number of that Ag atom, which changes from 12 to 6-8 during the simulation, implying the Ag diffusion from the bulk to the surface.
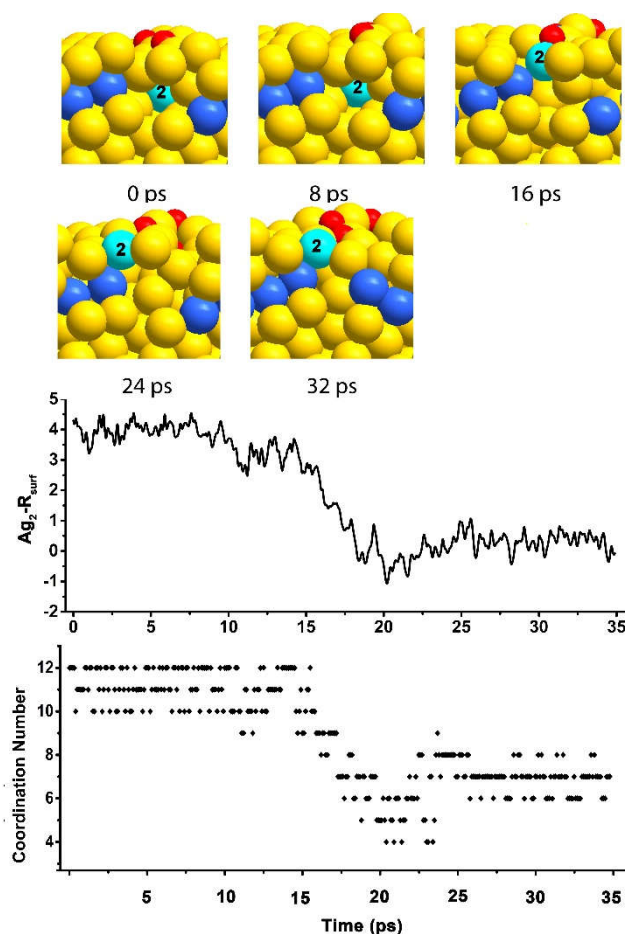

Fig. 2.9. An AIMD simulation showing vertical Ag diffusion from a subsurface layer to the surface. Ag atom is initially located below the surface gold layer. The distance of Ag to the surface, Ag_2-R_{surf}, and the coordination number of migrating Ag were monitored along the whole simulation trajectory. The reference surface is chosen in the same way as in Fig. 2.8. (Reproduced from Publication II, with permission from the American Chemical Society.)

To further support the result of this simulation that O atoms are responsible for Ag diffusion, a new simulation for a similar initial structure was repeated but without adsorbed O atoms, as shown in **Fig. 2.10**. The arrangement of Ag atoms is very similar to the initial structure of **Fig. 2.9,** except the two additional Ag atoms at the step edge. The trajectories at 0 ps, 8 ps, 16 ps and 24 ps are shown in **Fig**. **2**.**10**. On the time scale of our simulation at 700 K, no diffusion or surface reconstruction was observed. The diffusion coefficient was calculated as 0.028 Å^2 ps^{-1}, implying no diffusion. Hence, these results provide a theoretical basis for oxygen-induced Ag diffusion on the surface of np-Au.
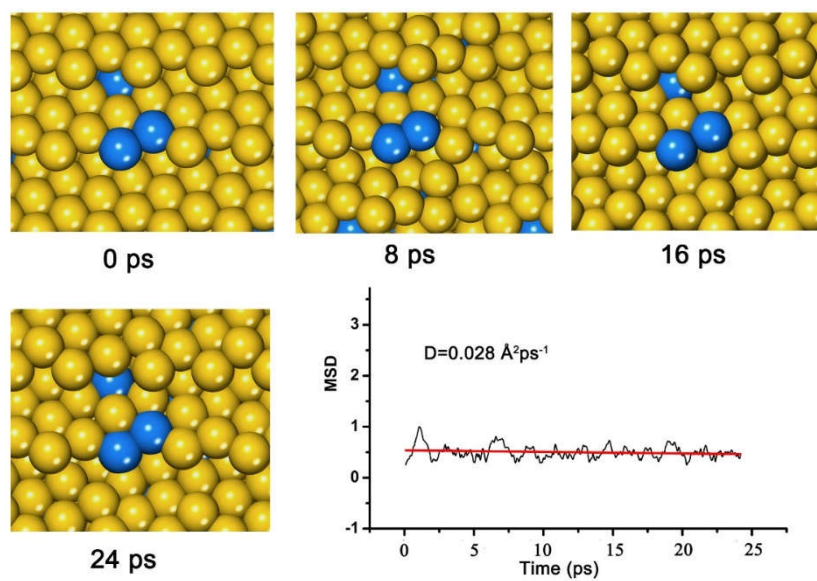
Fig. 2.10. An AIMD simulation shows a dynamic evolution of a Au(321) surface with Ag impurities but without chemically adsorbed O atoms. MSD stands for mean square displacement. The diffusion coefficient was calculated from Einstein relations. (Reproduced from Publication II, with permission from the American Chemical Society.)

Chapter 3 Structural Dynamics of Gold-Supported Ceria Nanoparticles

This chapter summarizes the results of publications III and IV which explored possible origin of the enhanced thermal stability of ceria-coated np-Au. The remarkable catalytic activity and high selectivity of nanoporous gold render this catalyst interesting for a variety of practically interesting reactions ranging from CO oxidation to more complex organic transformtion.[37-39] However, a potential problem restricting commercial applications of np-Au in catalysis, is its limited thermodynamic stability, which results from the nanosize of its ligaments in the range of a few 10 nm. Especially during catalysis, diffusion processes on the catalyst surface are accelerated by elevated temperature, surface reactions, and fast adsorption/desorption events further leading to coarsening of the nanoporous ligaments and finally resulting in a loss of catalytic activity.[36, 41-44] As discussed in Chapter I, deposition of nano-sized oxide particles (TiO_2, Al_2O_3, or CeO_2) on np-Au provides an opportunity to improve the thermal stability of its nanoporous structure to prevent coarsening even at very high temperatures of up to 600°C.[36, 63-65] The composite catalysts composed of ceria NPs deposited on np-Au (further denoted "ceria/np-Au") show very promising catalytic properties associated with the propensity of ceria to generate lattice oxygen vacancies.[66-68] This chapter summarizes the results of our theoretical study on the particle-support interaction, structural dynamics, and oxygen vacancy formation and migration processes in Au-supported ceria nanoparticles, in which the following model has been used a to represent the ceria/np-Au catalyst: a stoichiometric pyramidal $Ce_{10}O_{20}$ cluster (diameter ~1nm), as well as reduced clusters derived from this model ($Ce_{10}O_{19}$), were deposited either on the flat Au(111) surface or on the stepped Au(321) surface with kinks. Low-coordinated Au atoms at step and kink sites, which are abundant on np-Au, are present in the Au(321) surface, rendering it a reasonable model for the surface of np-Au.[53-54, 85-88] We carried out AIMD simulations and static DFT computations to address current chapter's objectives: (i) to study oxygen vacancy formation in the supported CeO_2 NPs and charge transfer between the ceria particles and the Au support for stoichiometric and reduced ceria NPs; (ii) to characterize structural rearrangements and dynamics in the surface region as well as the electronic structure of the CeO_x/Au(111) system and defect chemistry.

3.1 Oxygen Vacancy Formation and Structural Dynamics of the Composite Catalyst

Ceria NPs supported on np-Au were found to be rich in oxygen vacancy (O_V) defects. These defects most likely play important roles in catalysis, such as facilitating the binding of reactants and intermediates, providing active sites, reversibly accepting and releasing O atoms produced, or consumed in various elementary steps. Exploring possible defect formation sites and mechanisms, and studying the structural dynamics of ceria NPs supported on gold are fundamental steps on the way to understand and explore the reactivity of such two-component catalysts.

3.1.1 Ceria Nanoparticles Supported on Au(111)

As mentioned above, when constructing our computational models to study the interaction between np-Au and ceria in a composite catalyst, we made use of two types of gold surfaces: Au(111) and Au(321). These two surfaces represent two extremes of a very flat and a very rough motif. Both types of structural fragments have been identified on the surface of the ligaments of np-Au.[44] First, we discuss the results obtained from an AIMD simulation using Au(111)-supported stoichiometric ceria NPs ($Ce_{10}O_{20}$). Selected snapshots (from 0 ps to 24 ps) of the structural evolution of $Ce_{10}O_{20}$/Au(111) in a dynamic equilibration at 700 K are shown in **Fig**. **3.1**. The supported ceria nanocluster ($Ce_{10}O_{20}$) keeps its pyramidal shape unchanged on the Au(111) surface during the thermodynamic equilibration, indicating that the nanoparticle is rigid and thermally stable, which is in line with the transmission electron microscopy (TEM) observations.[66] In this regard, it is interesting to compare with the ceria-supported Au NPs (an inverse system with respect to the current ceria/Au catalyst), in which both experimental and theoretical investigations demonstrate that small Au NPs supported on the ceria (<2 nm) were significantly changing their shape under the exposure to a reactive CO + O_2 gas mixture.[70, 89] In contrast, the computational model $Ce_{10}O_{20}$/Au(111) considered to represent the catalyst under oxidizing conditions, showed dynamic stability. Neither the ceria cluster nor the Au(111) support showed restructuring. The structural dynamics of a partially reduced ceria particle $Ce_{10}O_{19}$/Au(111) was also explored using an AIMD simulation. Before turning to the results of these simulations, we will discuss the formation and migration of O vacancies
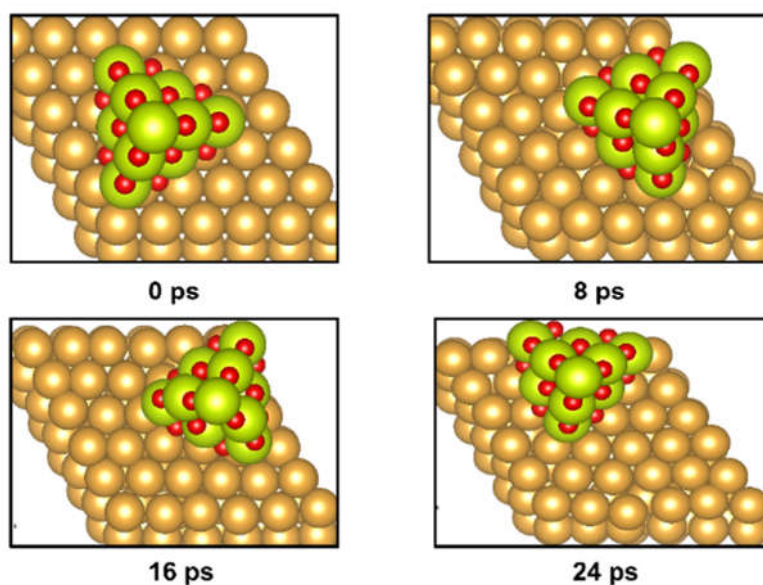
in a supported ceria nanoparticle.

Fig. 3.1 AIMD simulation of $Ce_{10}O_{20}$/Au (111) chemical model for 24 ps at 700 K. (Reproduced from Publication III, with permission from the American Chemical Society.)

According to an experimental characterization, ceria NPs in freshly synthesized ceria-functionalized np-Au are rich with O_V defects.[66] We employed static DFT computations to study the O_V defect formation at different sites of the $Ce_{10}O_{20}$ cluster supported on Au(111), as shown in **Fig**. **3.2**. Under real catalytic conditions, oxygen vacancies are probably either generated through O_2 desorption or produced via a reduction reaction, such as $CO + O \rightarrow CO_2$. In our model, four different types of O vacancies (excluding inner sites) were determined by the symmetry (C_{3v}) of the adsorbed $Ce_{10}O_{20}$ cluster on the Au(111) surface. The formation energies of O_V at four different sites are shown in **Fig**. **3.2a** and designated as **I, II, III, IV**, respectively. The energetically most favorable O_V formation site (**I**) is located at the perimeter edge site of the $Ce_{10}O_{20}$ cluster. After the O vacancy formation, a reduced $Ce_{10}O_{19}$/Au(111) model has two Ce^{3+} centers, in other words 20% of Ce^{3+}, which is close to the Ce^{3+} content in ceria NPs supported on silica aerogel (18%), as determined by electron magnetic resonance spectroscopy and magnetization studies.[69]

The computed spin density of **I**-O_V with the spin population value of 1.84 μ_B is shown in **Fig**. **3.2c**. The spin density implies that the O_V formation will leave two electrons to localize on Ce^{4+} ions resulting in the formation of $Ce-4f^1$ (Ce^{3+}) electronic configuration of these reduced Ce centers. The low-spin state of the **I**-O_V structure

without spin density was computed as well. It has higher energy than the high-spin state by 0.98 eV.
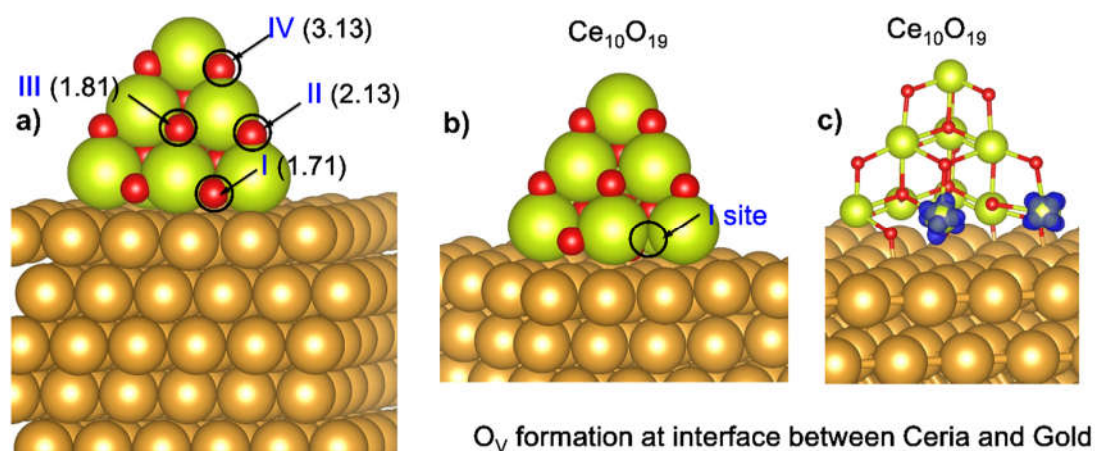

Fig. 3.2 a) The computed O_V formation energy $E(O_V)$ (in eV) at different sites of $Ce_{10}O_{20}$. **b)** The geometry of the $Ce_{10}O_{19}$ cluster with the most favorable O vacancy, **c)** Distribution of the spin density on two adjacent Ce atoms. (Reproduced from Publication III, with permission from the American Chemical Society.)

Next, we further evaluated the structural dynamics and stability of the reduced $Ce_{10}O_{19}$ nanoparticle supported on Au(111) with the O_V defect (**I**) at the ceria/gold perimeter. In the AIMD simulation, it was observed that O_V migrates from the perimeter site **I** to the inner bottom site **V** of the $Ce_{10}O_{19}$ nanoparticle after 1.2 ps of thermodynamic evolution, as shown in **Fig**. **3.3**. Interestingly, the spin density vanishes with the spin population value decreasing from 1.84 to 0 μ_B once O_V migration has been completed, indicating that electron delocalization or transfer is facilitated by the O_V migration. The AIMD simulation confirms that the Au-supported $Ce_{10}O_{19}$ cluster with a **V**-type oxygen vacancy at the gold-ceria interface is thermodynamically stable, as illustrated in a series of snapshots (**Fig**. **3.4**). The ceria particle is found to be rigid, as it maintains its original shape during the thermodynamic simulation.

To find out whether the vacancy migration from the perimeter to the inner interface is reversible, another AIMD simulation was carried out to evaluate whether added O atoms at the particle perimeter would be able to spontaneously refill the **V**-type of vacancy in $Ce_{10}O_{19}$/Au(111) system. Therefore, two O atoms were placed near two bottom corner Ce atoms and the system was thermalized at 700 K for 24 ps (**Fig**. **3.5)**. During the whole course of the simulation, no O atom diffusion to the inner O vacancy site of type **V** was observed, while the O vacancy remained at the same position within the cluster. Therefore, it was concluded that a spontaneous filling of the **V**-type

vacancy should be a low-probability event, probably due to a high barrier for O atom diffusion into the **V** site. The computed formation energy of the second O_V created at the perimeter in a ceria particle with an existing O_V at position **V** was found larger than 4.5 eV implying that the spontaneous formation of more than one O_V per particle in this size is a low-probability event.
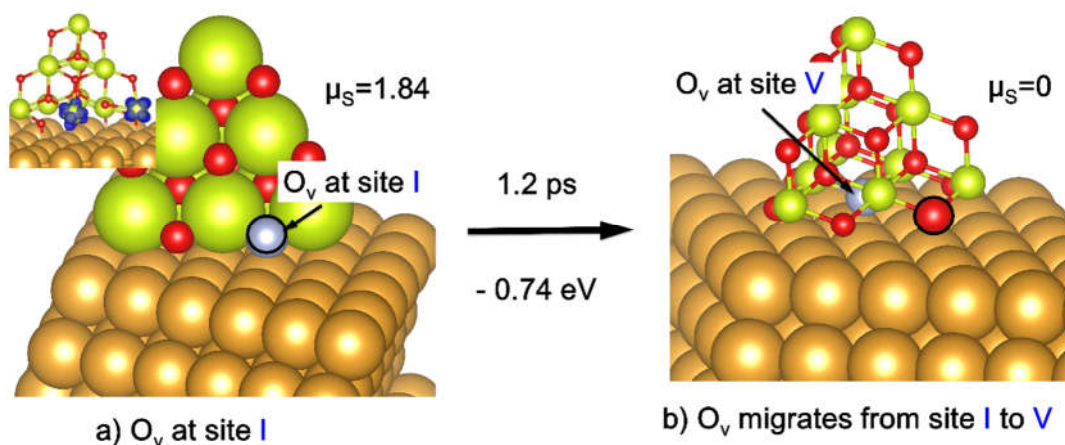
Fig. **3.3** O_V migration from site **I** to the bottom face-centered site **V** promotes an electron transfer from ceria to Au. **a)** Geometric structure and spin density of the Au-supported $Ce_{10}O_{19}$ cluster with O_V (shown in gray) at the position **I**, two unpaired Ce-4f electrons are localized on two Ce atoms. **b)** after 1.2 ps of an AIMD simulation, O_V is transferred to the inner face-centered site **V**, while the magnetic moment changes from 1.84 to 0 μ_B. (Reproduced from Publication III, with permission from the American Chemical Society.)

Fig. **3.4** AIMD simulation of $Ce_{10}O_{19}$/Au (111) chemical model with the O vacancy of type **I** for 24 ps at 700 K. (Reproduced from Publication III, with permission from the American Chemical Society.)

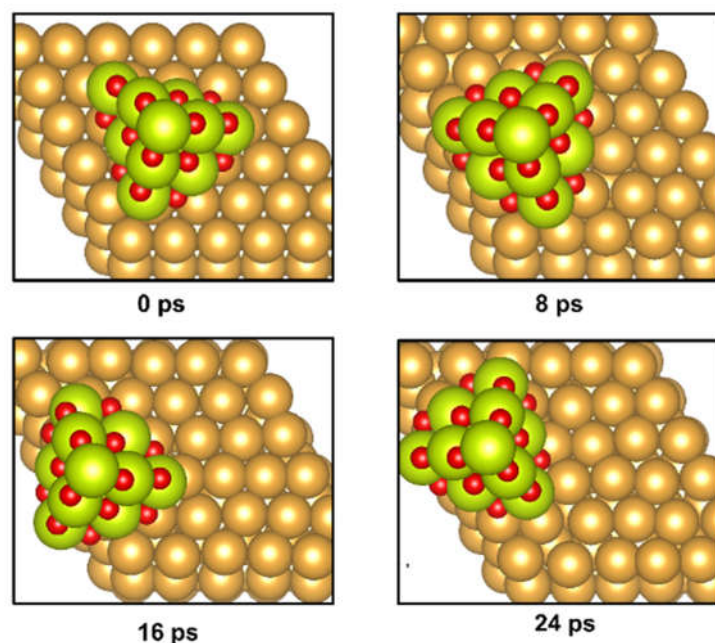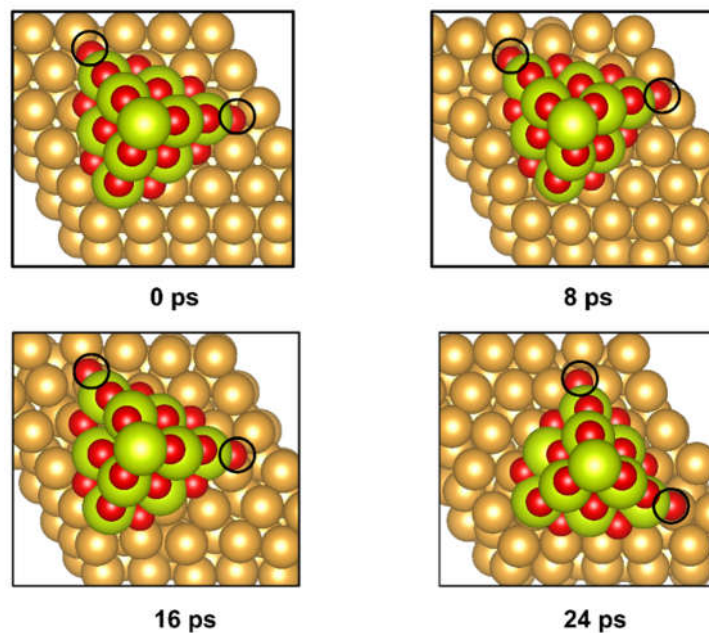**Fig. 3.5** Snapshots from an AIMD simulation at 700 K of the $Ce_{10}O_{19}$/Au(111) model with **V**-type oxygen vacancy and two added O atoms at the corners of the ceria cluster. (Reproduced from Publication III, with permission from the American Chemical Society.)

3.1.2 Ceria Nanoparticles Supported on Au(321)

In this section, we present the study of structural dynamics of model ceria nanoclusters supported on the Au(321) surface. The stepped Au(321) surface contains all important structural motifs, such as kinks, low-coordinated Au atoms and steps, which are abundant on np-Au, rendering it a reasonable model for the rough surface relief of np-Au. Like for the ceria/Au(111) model discussed above, here we also used AIMD simulations to study the O vacancy formation in a ceria cluster supported on Au(321), the structural dynamics, and interface interaction between gold and ceria for a more comprehensive understanding of the structure and surface dynamics of the ceria-coated np-Au catalyst.

First of all, most probable sites of O_V defect formation at the $Ce_{10}O_{20}$/Au(321) interface and at various locations of the $Ce_{10}O_{20}$ cluster were probed, as shown in **Fig. 3.6**. We investigated 10 different possibilities of O_V formation determined by the symmetry of the $Ce_{10}O_{20}$ cluster and by the inequality of the perimeter sites between the ceria cluster and Au(321) surface. The O_V formation energies at different sites numbered from **1** to **10** are listed in **Fig. 3.6d** (where **1** was assigned to an inner interfacial site, similar to the **V**-type of O vacancy in the ceria $Ce_{10}O_{19}$/Au(111) system discussed above). The calculated formation energies (E_v) of O vacancies at the

interfacial perimeter (2.41 to 2.76 eV) are smaller than for the upper sites not directly contacted to the Au surface (2.73 to 3.28 eV). The energetically most favorable O_V formation site (**1**) with the lowest E_v (1.63 eV) is located at the center of the interfacial area between the $Ce_{10}O_{20}$ cluster and the Au(321) surface (**Fig**. **3.6c**), similarly to what was found for the $Ce_{10}O_{19}$/Au(111) system. Therefore, we expect that O vacancy formation in ceria NPs supported on np-Au will most likely create O_V at the particle perimeter sites; eventually, the vacancy should migrate to the inner part of the interface due to lower energy of such O vacancies.
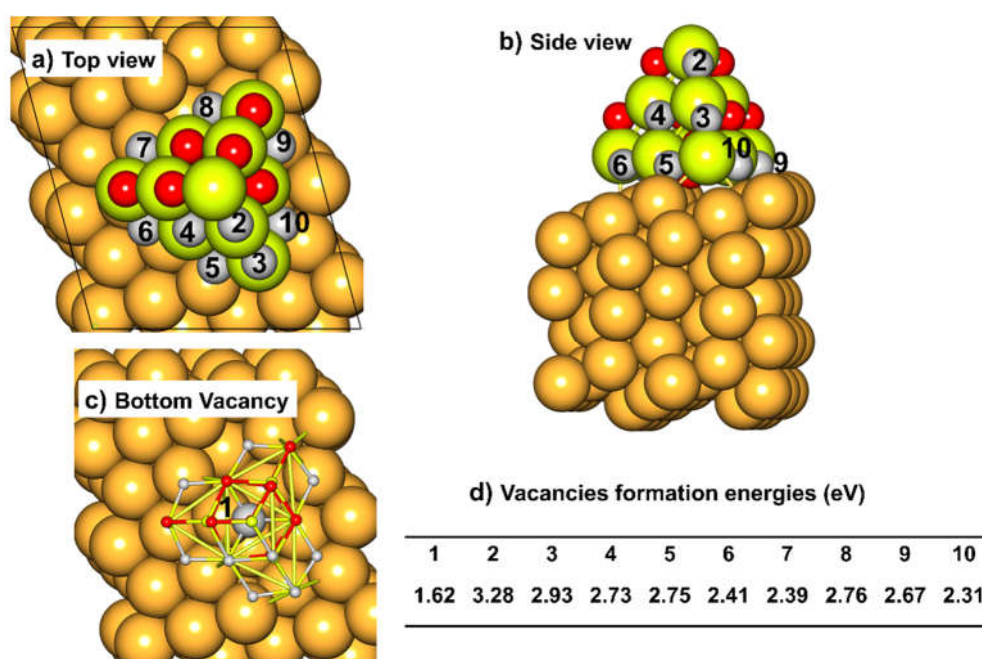
Fig. 3.6 Computed O_V formation energy (in eV) at different sites (gray spheres, numbered from 1 to 10) of $Ce_{10}O_{20}$. **a)** Top view and **b)** side view of the supported $Ce_{10}O_{20}$ cluster. **c)** The energetically most favorable site **1** (corresponding to type **V** O vacancy in ceria/Au111)) is located at the bottom center of the interface between the $Ce_{10}O_{20}$ cluster and the Au(321) support. **d)** Vacancy formation energies at various sites. Color coding: orange, Au; lime, Ce; red/gray, O. (Reproduced from Publication IV, with permission from the American Chemical Society.)

For each of the systems, the $Ce_{10}O_{20}$/Au(321) and $Ce_{10}O_{19}$/Au(321) 30-ps AIMD simulations at 700 K were carried out to thermalize and equilibrate them. In both cases the ceria cluster retained its pyramidal shape and atomic connectivity. In the case of the stoichiometric particle $Ce_{10}O_{20}$, the support also remained almost unchanged during the simulation (**Fig**. **3.7a**), whereas the surface with a reduced cluster $Ce_{10}O_{19}$ was strongly deformed and restructured during the simulation (**Fig**. **3.7c**). In the final structure after a 30 ps equilibration, the $Ce_{10}O_{19}$ particle is found to be partially sunk

into the Au support implying a strong particle-support interaction. This can be seen from the side view of the structure at the end of the AIMD simulation (**Fig**. **3.7c**) and from the increased G(r) of Au-Ce distance in the range of a covalent bond, as shown in **Fig**. **3.7d**.
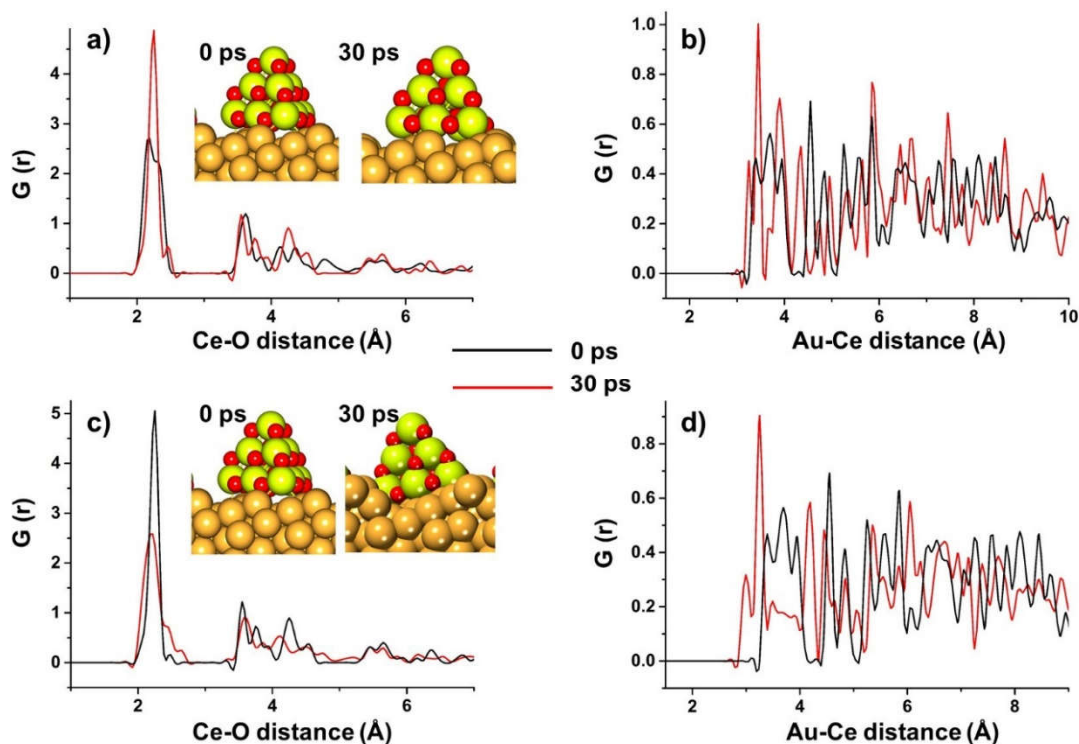
Fig. **3.7** The Ce-O and Ce-Au radial distribution function G(r) at 0 ps and 30 ps. Insets show selected images from AIMD trajectories at 0 ps and 30 ps. **a)** and **b)** are the G(r) of Ce-O and Ce-Au distances of $Ce_{10}O_{20}/Au(321)$; **c)** and **d)** are the G(r) of Ce-O and Ce-Au distances of $Ce_{10}O_{20}/Au(321)$. (Reproduced from Publication IV, with permission from the American Chemical Society.)

3.2 The Particle-Support Interaction and Charge Transfer between Ceria and Gold

As we discussed at the beginning of this chapter, ceria NPs can prevent coarsening of the ligaments of np-Au, so that one can expect that such enhancement in thermal stability is probably attributed to the strong interaction and charge transfer between the oxide NPs and np-Au surface. Therefore, we systematically investigated the interaction and charge transfer between nano-sized ceria particles and the gold support based on the models composed of either the stoichiometric $Ce_{10}O_{20}$ or partially reduced $Ce_{10}O_{19}$ cluster adsorbed on the Au(111) and Au(321) surfaces. The adsorption energies of

$Ce_{10}O_{20}$ and $Ce_{10}O_{19}$ on the Au(111) and Au(321) surfaces, as well as the charge transferred from ceria to Au have been computed and can be found in Table 3.1. For the $Ce_{10}O_{19}$ cluster we assumed the energetically most favorable vacancy position in the center of the bottom facet (**V**-type of vacancy) of the pyramidical ceria cluster (Table 3.1). The binding energies of $Ce_{10}O_{20}$ and $Ce_{10}O_{19}$ on Au(111) were computed as -2.28 and 3.03 eV. The adsorption is accompanied by ceria-to-Au charge transfer of 0.50 and 1.52 e, respectively, as obtained from Bader charge analysis. The calculated adsorption energies for $Ce_{10}O_{20}$ and $Ce_{10}O_{19}$ on the Au(321) surface are -2.76 and -3.56 eV, larger than the respective values calculated for ceria NP adsorption on Au(111) surface by around ~0.5 eV. A Bader charge population analysis shows that the $Ce_{10}O_{20}$ cluster transfers 0.56 e and the $Ce_{10}O_{19}$ cluster transfers 1.51 e to the Au(321) surface, similar to the values computed for the ceria/Au(111) surface system, implying a strong interaction between the gold support and the ceria clusters, which becomes stronger for reduced ceria particles. During the dynamic thermalization of ceria on Au at 700 K, the adsorption energies and charge transfer in the $Ce_{10}O_{20/19}$/Au(111) systems remain unchanged. Similarly, it was found that in the case of a stoichiometric particle $Ce_{10}O_{20}$/Au(321), the adsorption energy and charge transfer from the particle to the support remained unchanged by the end of the simulation (**Fig**. **3.8a**). However, the reduced $Ce_{10}O_{19}$/Au(321) model increases its adsorption energy by 0.53 eV. At the same time the Au substrate adapts its shape to better accommodate the ceria cluster. At the same time, the charge transfer from ceria to Au also increases by 0.12 e after the thermal equilibration (**Fig**. **3.8b**). We suggest that the strong binding energies between ceria and np-Au associated with the strong ceria-to-Au charge transfer are responsible for the enhanced stability of np-Au preventing the coarsening of Au nanostructured ligament.

Table 3.1 Calculated adsorption energies of ceria nanoparticle and transferred charge from ceria to Au (from Bader charge analysis) on Au(111) and Au(321) surfaces.

	Adsorption energies (eV)		Transferred Charge (e)	
	Au(111)	Au(321)	Au(111)	Au(321)
$Ce_{10}O_{20}$	2.28	2.76	0.50	0.56
$Ce_{10}O_{19}$	3.03	3.56	1.52	1.51

In the investigated inverse CeO_x/Au catalyst, the charge transfer direction between gold and ceria is different from the ceria supported Au nanoparticles

(Au$_n$/ceria), where the charge transfer direction was found to depend on the redox state of the ceria support, nanoparticle size, and presence of electron-donating or withdrawing adsorbates (e.g. CO, O$_2$).[21, 23, 70, 90-93] In general, earlier theoretical studies have found that on defect-free ceria surfaces without adsorbates the charge transfer is always from Au$_n$ to ceria, so that Au atoms or small clusters are (partially) oxidized. If an Au$_n$ cluster adsorbs at an O vacancy site, some of its atoms (those in contact with the oxide surface) acquire a partial negative charge, but the overall charge on Au$_n$ (for n>4) is positive.[21]
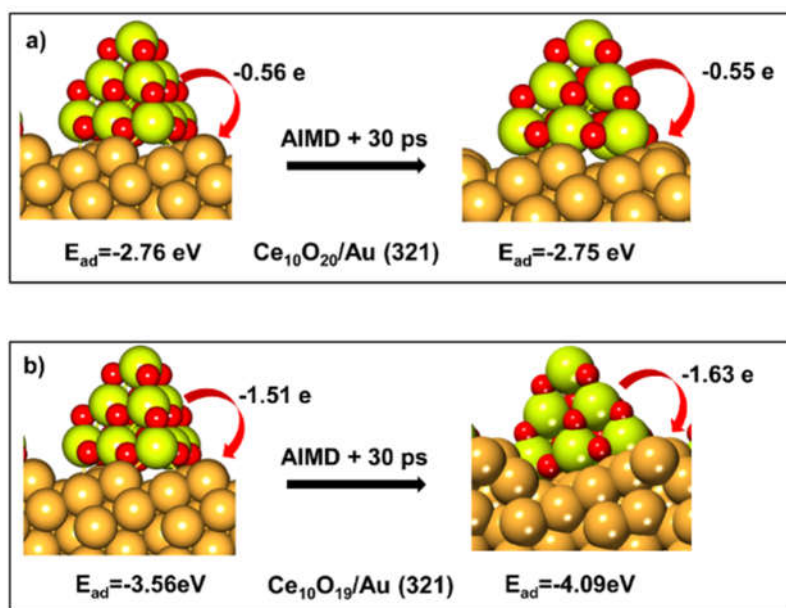

Fig. **3.8** Adsorption energies E_{ad} and partial charge transfer from ceria to gold for the oxidized and reduced ceria NPs in the initial and final structure of the AIMD thermal equilibration at 700 K. **a)** The Ce$_{10}$O$_{20}$ nanocluster on Au(321). Both support and ceria retain the original shape after 30 ps thermalization at 700 K. **b)** The Ce$_{10}$O$_{19}$ nanocluster on Au(321) embeds itself in the Au(321) surface, and the Au surface restructures during thermalization. Color coding of elements: orange, Au; lime, Ce; red, O.

To further elucidate the strong particle-support interaction between the Au support and the Ce$_{10}$O$_{19}$ cluster, we computed one-dimensional potential energy curves for the adsorption of a defective Ce$_{10}$O$_{19}$ cluster onto the Au(111) surface in different spin states. By computing the energy and electronic structure changes along the reaction coordinate (defined for the cluster-surface distance), the potential curves were obtained, as shown in **Fig**. **3.9**. Initially, the Ce$_{10}$O$_{19}$ cluster with the O$_V$ located at the center of its bottom facet was placed 6.5 Å away from the Au surface. The cluster approached the Au(111) surface with a facet directed towards the Au surface (**Fig**. **3.9**), so that the final

geometry corresponded to the lowest-energy $Ce_{10}O_{19}/Au(111)$ system with O_V in the inner interface position (type **V**). The structure of the $Ce_{10}O_{19}$ cluster far from the surface had a spin magnetic moment $\mu_s = 2\ \mu_B$ corresponding to two unpaired 4f electrons spreading over three Ce centers at the corners of the defected bottom facet, **Fig**. **3.9**. In Marcus electron-transfer theory, electron transfer occurs when the potential energy surfaces of two different electronic states cross. Two energy curves (for the high- and low-spin states) were obtained by varying the distance between the $Ce_{10}O_{19}$ cluster and the Au support as shown in **Fig**. **3.9**. Two potential energy curves corresponding to the two different electronic states, Ce-4f^2 (black curve) and Ce-4f^0 (red curve) cross at the distance of 4.3 Å from the surface indicating electron transfer from ceria to the Au surface. Based on such simple chemical model, a picture of the electron transfer from a ceria NP to the Au support is directly demonstrated and observed.
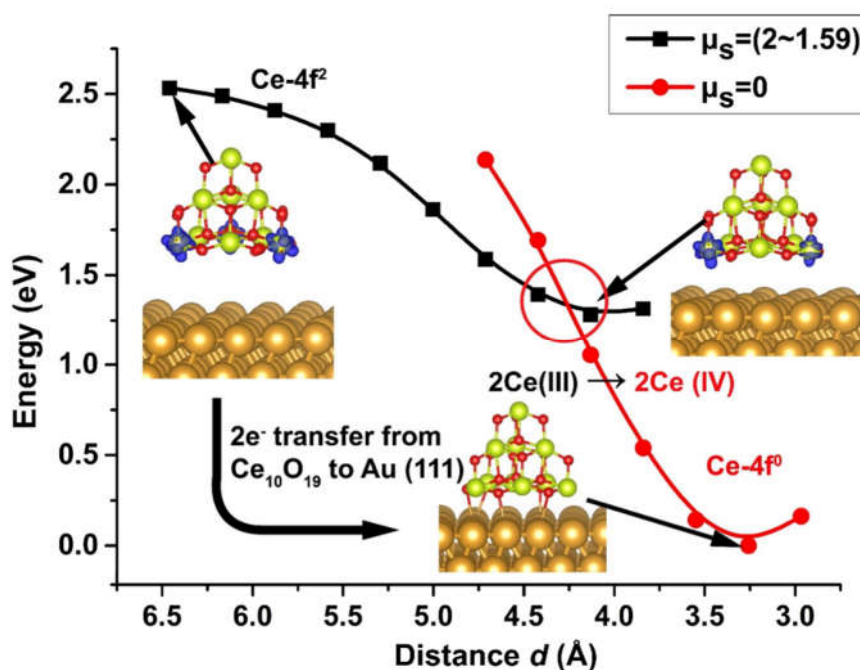
Fig. **3.9** Potential energy surface scans. Two potential energy curves for the high-spin and low-spin states denoted Ce-4f^2 and Ce-4f^0 were obtained by varying the distance *d* between Au(111) and the bottom surface of the $Ce_{10}O_{19}$ particle. These curves cross when the ceria particle approaches the Au surface at *d* around ~4.3 Å allowing the transfer of two electrons to Au. The spin magnetic moment μ_s changes from ~2 to 0 μ_B in the overall process. (Reproduced from Publication III, with permission from the American Chemical Society.)

Chapter 4   The Mechanism of O$_2$ Adsorption and Activation

This chapter builds on the results from publications III and IV, on the computationally revealed mechanism of O$_2$ adsorption and activation on a composite ceria/Au catalyst. Although the O$_2$ molecule in its triple-state is a diradical, it is not particularly reactive, which is attributed to a strong static MO (molecular orbital) correlation, or VB (valence bond) resonance stabilization of the $\pi_u^4 \pi_g^{*2}$.[94-95] An aerobic oxidation reaction requires pre-adsorption and activation of O$_2$ on the catalyst to lower the activation barrier. Although O$_2$ does not adsorb on the Au(111) surface and on stoichiometric ceria, and only weakly adsorbs on the stepped Au(321) surface, it strongly adsorbs at the interface of the composite catalysts ceria/Au(111) and ceria/Au(321) due to the charge density accumulation at the interface caused by the strong support-particle interaction. Our studies demonstrated that the charge accumulation at the interface can provide excess electrons to facilitate the adsorption and activation of the O$_2$ molecule for aerobic oxidation reactions. The electrons transferred from reduced ceria to Au delocalize at the gold-ceria interface, as revealed by a charge density difference analysis, **Fig**. **4.1** and **Fig**. **4.2**. For a stoichiometric Ce$_{10}$O$_{20}$ cluster on Au(111) and Au(321), the charge density polarization has also been found, as shown in **Fig**. **4.1b** and **Fig**. **4.2a**.

a) Ce$_{10}$O$_{19}$/Au(111)   **b) Ce$_{10}$O$_{20}$/Au(111)**
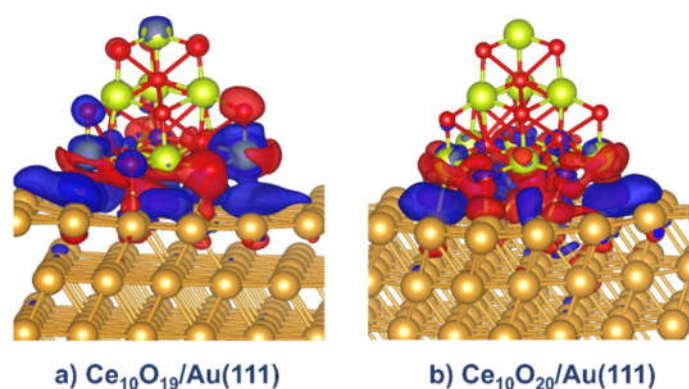
Fig. **4.1** Charge density difference analysis for Au-supported ceria NPs: a) a reduced Ce$_{10}$O$_{19}$ particle with a **V**-type vacancy, b) perfect stoichiometric Ce$_{10}$O$_{20}$ model without a vacancy. The charge density difference was computed according to $\Delta\rho = \rho_{AB} - \rho_A - \rho_B$, where A and B stand for Au(111) and Ce$_{10}$O$_{19/20}$. Electron density increase is shown in blue, electron density decrease is shown in red (isovalue: 0.01 au). (Reproduced from Publication III, with permission from the American Chemical Society.)
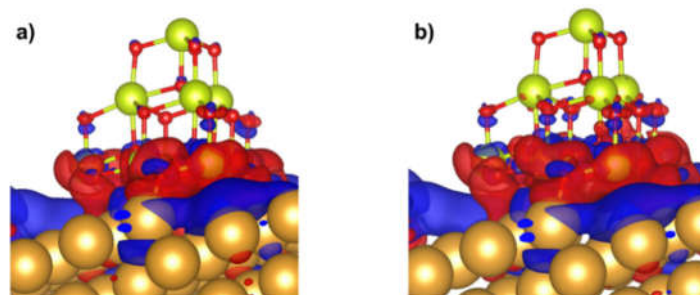
Fig. **4.2** Charge density difference analysis for ceria NPs supported on Au(321): (a) perfect stoichiometric $Ce_{10}O_{20}$ model without a vacancy, (b) a reduced $Ce_{10}O_{19}$ particle with the type-**V** O_V.

First, we studied the adsorption of O_2 on the reduced ($Ce_{10}O_{19}$, O_V in position **V**) and oxidized ($Ce_{10}O_{20}$) models of ceria NPs supported on Au(111). Possible adsorption sites and geometric configurations of the adsorbed O_2 molecule have been investigated for both models. The O_2 adsorption on $Ce_{10}O_{19}$/Au(111) is illustrated in **Fig**. **4.3**. The probed O_2 adsorption sites are the same for the $Ce_{10}O_{19}$ and $Ce_{10}O_{20}$ clusters supported on Au(111). In all cases, the O_2 binds to ceria, or to both gold and ceria, while there is no O_2 adsorption on the gold support, which is consistent with previous reports of very weak or even repulsive interaction between O_2 and Au(111).[96]

Fig. **4.3** The O_2 adsorption on Au(111)-supported $Ce_{10}O_{19}$. Blue spheres represents O_2 molecule. (Reproduced from Publication III, with permission from the American Chemical Society.)

33

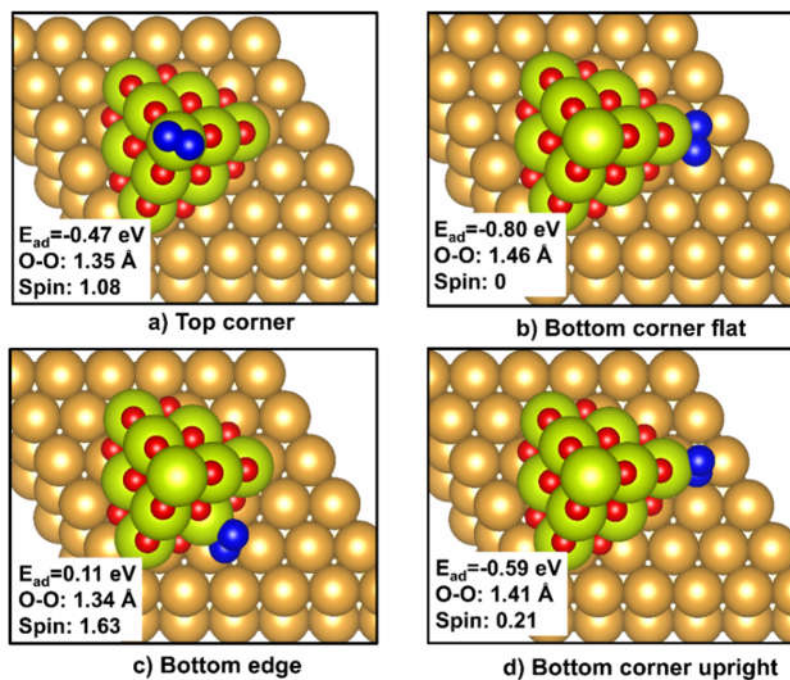The energetically most favorable adsorption site is the same for the reduced ($Ce_{10}O_{19}$/Au) and stoichiometric ($Ce_{10}O_{20}$/Au) models. O_2 adsorbs most strongly at the bottom corner sites of the pyramidal ceria cluster, at the interface between the cluster and the Au(111) surface, as shown in **Fig**. **4.4**. The adsorbed O_2 chemically binds to one unsaturated Ce atom (with the coordination number 4) and two Au atoms. We note that in a previous theoretical study by Wang et al. of CO oxidation on ceria supported Au_n clusters the oxygen molecule was suggested to preferentially adsorb at O vacancies of the oxide support in the case of ceria-supported gold nanoparticles.[70] It was also found that the adsorption of O_2 on a perfect ceria surface and the gold-ceria interface is relatively weak.[70] The spin population values on O atoms in the energetically most favorable adsorption geometry of O_2 in both cases ($Ce_{10}O_{19}$ or $Ce_{10}O_{20}$ clusters) are 0, implying a change from a triplet O_2 to a singlet O_2^{2-}. The O-O bonds are lengthened from 1.26 to 1.46 and 1.44 Å, respectively, as illustrated in **Fig**. **4.4**. The adsorption energies are -0.80 eV and -0.75 eV, for the $Ce_{10}O_{19}$ and $Ce_{10}O_{20}$ clusters, respectively. A previous study has shown that the O_2 adsorption energies on Au_{20} or at perimeter sites of ceria supported gold clusters are weaker than -0.2 eV,[70] indicating much weaker adsorption than found in this work. The O_2 adsorption on the defective $Ce_{10}O_{19}$/Au(111) model is slightly more energetically favorable than on the perfect model by 0.05 eV. This study shows that the presence of oxygen vacancies in the gold-supported ceria particles is not the decisive factor for the oxygen molecule adsorption and activation. Indeed, the O_2 adsorption energy at the O_V site of type **I** (-0.48 eV) is even weaker than in the case of a stoichiometric cluster $Ce_{10}O_{20}$. Furthermore, we have also found that the O_2 adsorbs very weakly on the free $Ce_{10}O_{20}$ cluster, while its adsorption energy on $Ce_{10}O_{19}$ is -0.60 eV. The dissociation energy of O_2 on $Ce_{10}O_{19}$ is predicted as 1.02 eV implying a high activation barrier of O_2 dissociation. We thus conclude that it is the electron density accumulating at the interface between ceria and gold that promotes O_2 adsorption and activation. This is a synergistic effect resulting from the interaction of the ceria cluster and Au support.

Various possible geometric configurations of O_2 adsorption on the Au(321)-supported $Ce_{10}O_{19}$ and $Ce_{10}O_{20}$ models were predicted as well, as shown in **Fig**. **4.5**. The energetically most favorable sites for O_2 adsorption (**e** adsorption configuration in **Fig**. **4.5** and Table 4.1) are the same for both models, namely, at the bottom corner positions of the pyramidal ceria cluster at the interface between the ceria cluster and the Au(321) surface, as shown in **Fig**. **4.5** and **Table 4.1**. The adsorbed O_2 chemically binds

to one unsaturated Ce atom (with the coordination number 4) and to two Au atoms. The spin population values on O atoms in the energetically most favorable adsorption geometry in both cases ($Ce_{10}O_{19}$ or $Ce_{10}O_{20}$ clusters) are 0, implying a change from the triplet O_2 to the singlet O_2^{2-}. The O-O bond in the activated O_2 molecule elongates from 1.26 (in the gas phase) to 1.47 or 1.43 Å, respectively. The adsorption energies of O_2 are -1.62 eV and -1.57 eV, which indicates a significantly stronger O_2 adsorption than in the case of the ceria/Au(111) system. In line with previous reports of weak adsorption of O_2 (-0.16 eV) on pure Au(321)[49], our computations predicted weak adsorption of the O_2 molecule (weaker than -0.24 eV) on Au atoms other than the perimeter sites in contact with the $Ce_{10}O_{19}$ or $Ce_{10}O_{20}$ NPs. The adsorption energy of O_2, the O-O bond length, and the net spin population on the O_2 molecule adsorbed on pure gold surfaces, ceria NPs, and gold-supported ceria NPs are given in **Table 4.2**.
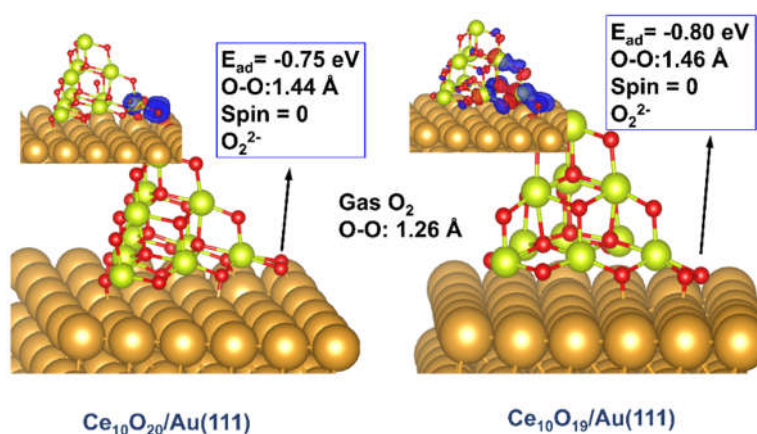
Fig. 4.4 The energetically most favorable O_2 adsorption sites at the Au-supported $Ce_{10}O_{19}$ and $Ce_{10}O_{20}$ clusters. The charge density difference was computed according to $\Delta\rho = \rho_{AB} - \rho_A - \rho_B$, where A and B stand for $Ce_{10}O_{19/20}$/Au(111) and O_2. Electron density increase is shown in blue, electron density decrease is shown in red (isovalue: 0.02 au). (Reproduced from Publication III, with permission from the American Chemical Society.)

To summarize, we have found that O_2 strongly adsorbs at the perimeter interface between ceria and gold in both oxidized and reduced systems with a significantly weakened O-O bond preparing it for a low-barrier reduction by a CO molecule.
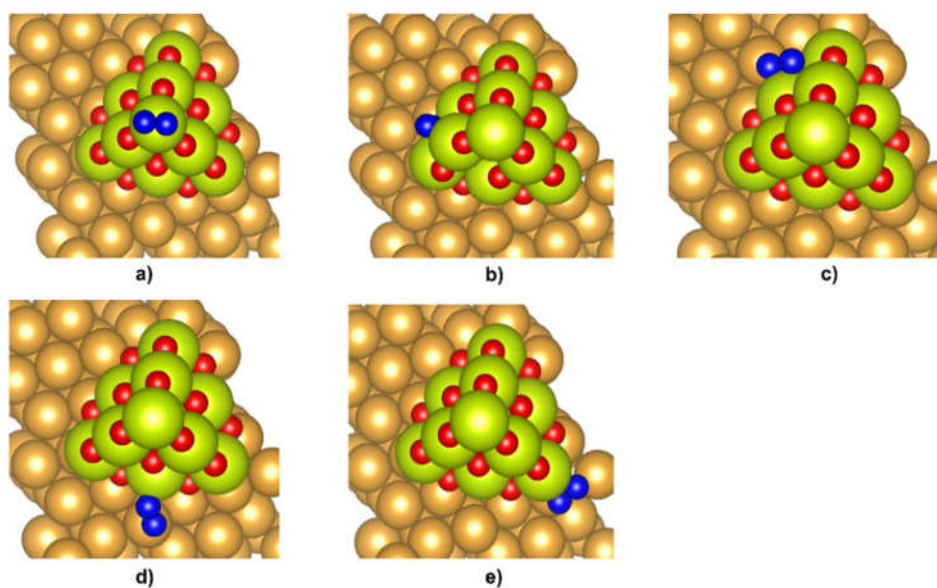
Fig. 4.5 Possible geometric configurations of O_2 adsorption on the $Ce_{10}O_{19}$/Au(321) model catalyst. Color coding of elements: orange, Au; lime, Ce; red, O; blue, adsorbed O_2; gray, C.

Table 4.1 The adsorption energies and spin population on O atoms of O_2, the O-O bond lengths for O_2 adsorbed on $Ce_{10}O_{20/19}$/Au(321).

Configuration	E_{ad} (eV)	Spin population	O-O bond length (Å)
		$Ce_{10}O_{19}$/Au(321)	
a	-0.41	0.51, 0.49	1.37
b	-0.64	0.51, 0.49	1.37
c	-0.86	0.0, 0.0	1.44
d	-0.66	0.10,0.13	1.36
e	-1.62	0.0, 0.0	1.47
		$Ce_{10}O_{20}$/Au(321)	
a	-0.11	101, 0.97	1.29
b	-0.03	0.93, 0.96	1.27
c	-0.31	0.58,0.71	1.30
d	-0.29	0.78,0.61	1.30
e	-1.57	0.0, 0.0	1.46

Table 4.2 The most favorable O_2 adsorption energy, spin population and O-O bond lengths in different systems

O_2 adsorption	E_{ad}	Spin population	O-O bond length (Å)
Au(111)	-0.08	1.0, 1.0	1.26
$Ce_{10}O_{20}$/Au(111)	-0.75	0.0, 0.0	1.43
$Ce_{10}O_{19}$/Au(111)	-0.80	0.0, 0.0	1.45
Au(321)	-0.16	0.52, 0.53	1.33
$Ce_{10}O_{20}$/Au(321)	-1.57	0.0, 0.0	1.43
$Ce_{10}O_{19}$/Au(321)	-1.62	0.0, 0.0	1.47
$Ce_{10}O_{20}$	-0.07	1.0, 1.0	1.26
$Ce_{10}O_{19}$	-0.60	0.48, 0.51	1.34

Chapter 5   CO Oxidation via a Mars-van Krevelen Mechanism

This chapter summarizes a new CO oxidization mechanism on a two-component inverse ceria/Au(111) catalyst from publication III. In Chapter 3, we highlighted the finding that the deposition of nano-sized CeO_2 particles on np-Au drastically improved its thermal stability and also increased its catalytic activity. However, the mechanistic details of how ceria may increase the catalytic activity of an oxidation reaction on such an inverse catalyst remain unclear. By contrast, the catalytic mechanism of CO oxidation by O_2 on more traditional catalysts composed of Au NPs supported on TiO_2 or CeO_2 has been much more intensively studied in the literature.[70-73, 97-100] In this chapter, we present the results of *ab initio* molecular dynamics (AIMD) simulations along with "static" DFT computations using $Ce_{10}O_{19/20}$ clusters supported on Au(111) as a model system revealing the mechanism and dynamics of catalytic CO oxidation at the molecular and atomic scale.

An earlier theoretical study reported a very weak binding of CO on the ceria (111) surface with the adsorption energy of -0.25 eV.[101] In this work, we found no binding of CO to free $Ce_{10}O_{19/20}$ clusters. The adsorption energy of CO on the Au terrace of the $Ce_{10}O_{19}$/Au(111) model is -0.80 eV for each CO molecule (see **Fig 5.1,** top left snapshot). In the absence of the ceria nanoparticle, the adsorption energy of CO on the bare Au(111) surface is weaker, -0.67 eV (**Table 5.1**). The presence of the $Ce_{10}O_{19}$ cluster on Au(111) increases the magnitude of CO adsorption energy by ~0.11 eV, and the co-adsorption with O_2 in addition slightly increases it by 0.02 eV. When comparing this calculated CO adsorption energy on Au(111) with experimental and other theoretical values,[102-103] one can expect that the PBE+D3 method likely overestimates it.

Table 5.1 Computed CO adsorption energy on Au (111) surface with different adsorbates. Au represent Au(111) surface; Au-Ceria: $Ce_{10}O_{19}$/Au(111).

	CO/Au	2CO/Au	CO/Au-Ceria	2CO/Au-Ceria	2CO, O_2/Au-Ceria
PBE	-0.42	-0.45			
PBE+D3	-0.59	-0.67	-0.67	-0.78	-0.80

The initial structure was prepared for an AIMD simulation with two CO and two O_2 molecules adsorbed on the $Ce_{10}O_{19}$/Au(111) model as shown in **Fig. 5.1** (top left). The average adsorption energy of O_2 in this initial structure is -0.78 eV per O_2 molecule, ~0.2 eV stronger than on a free $Ce_{10}O_{19}$ cluster (**Table 4.2**). Starting from this initial structure, an AIMD simulation (**Fig. 5.1**) was carried out to explore the catalytic reaction between CO and O_2 at 700 K. Interestingly, the first CO molecule reacts with a lattice O atom rather than with the activated O_2^{2-} species, leaving an oxygen vacancy at the perimeter of the ceria cluster (the cluster reduces to $Ce_{10}O_{18}$). During the next 10 ps of the simulation, the second CO molecule reacts with O_2^{2-} forming a CO_2 molecule and generating an O atom coordinated to the corner Ce atom. Finally, the O atom migrates to fil the oxygen vacancy site at the perimeter recovering the complete framework of $Ce_{10}O_{19}$ during next 8 ps of the simulation. A more accurate reaction energy profile including the reactants, transition states, intermediates, and products of all elementary steps revealed during the AIMD simulation was subsequently refined using static DFT calculations and is shown in **Fig**. **5.2**.
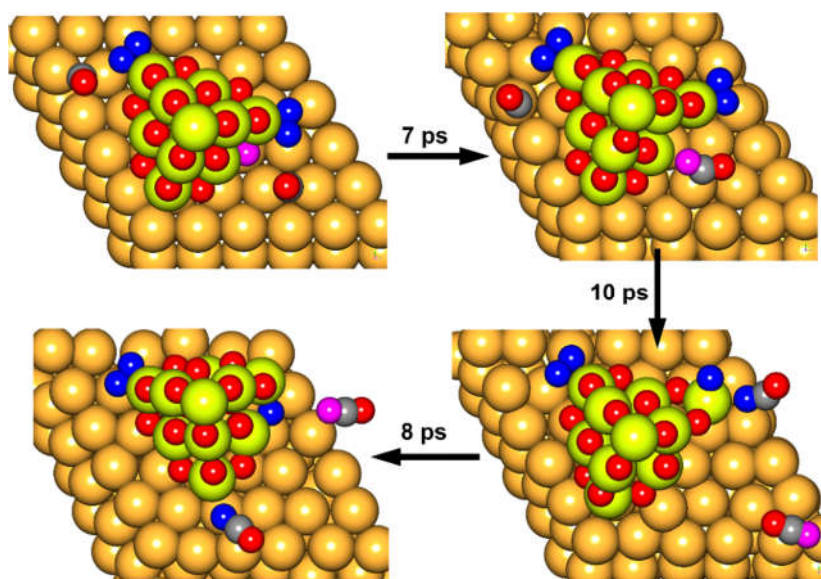
Fig. **5.1** The AIMD simulation of CO oxidation reaction on Au-supported $Ce_{10}O_{19}$. Color coding of elements: orange, Au; lime, Ce; red and magenta, O; blue, adsorbed O_2; gray, C. (Reproduced from Publication III, with permission from the American Chemical Society.)

In the first step (denoted **I-ts1-II** in **Fig**. **5.2**), one of the CO molecules reacts with a lattice O atom located at the edge perimeter site of ceria nanoparticle to form a CO_2 molecule with an activation energy of only 0.21 eV and reaction energy of -1.16 eV. The generated CO_2 with a slightly bent O-C-O angle adsorbs in a monodentate

fashion with an O atom coordinated to one of the perimeter Ce atoms adjacent to the O vacancy created in the previous step. CO_2 can desorb with desorption energy of 0.52 eV. The corresponding reaction path is denoted **II-III** in the energy diagram of **Fig. 5.2**. The second CO molecule is oxidized by the activated O_2^{2-} species forming CO_2 and an O atom coordinated to a corner Ce atom in the **III-ts2-IV** reaction step. The corresponding activation barrier and reaction energy were predicted to be 0.30 eV and -3.04 eV, respectively. The formed CO_2 molecule directly desorbs into the gas phase implying very weak adsorption. The remaining O atom, left behind as a result of CO oxidation is thermodynamically unstable, and thus migrates to the O_V site filling the vacancy in the **IV-ts3-V** reaction step with the barrier and reaction energy of 0.20 eV and -1.25 eV, respectively. Based on the theoretically predicted low-energy reaction path, we propose a Mars-van-Krevelen mechanism for the catalytic CO oxidation on a ceria/Au catalyst.
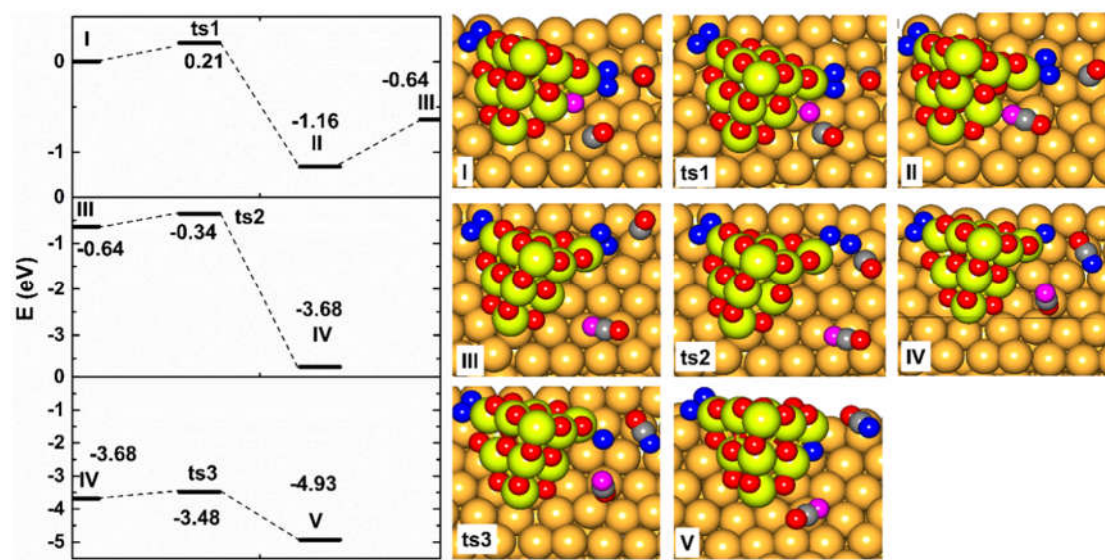
Fig. 5.2. CO oxidation mechanism calculated using DFT for the $Ce_{10}O_{19}$/Au(111) system, predicted with the help of AIMD simulations. The left panel shows the reaction energy profile. The right panel depicts the reactants, intermediates, transition states and products. The reaction includes three main steps: oxidation of the first CO molecule by an O atom of the ceria nanoparticle and the CO_2 desorption **I-ts1-II-III** (*CO + $O_{lattice}$ → *CO_2, *CO_2 → CO_2), oxidation of the second CO molecule by O_2^{2-} **III-ts2-IV** (*CO + O_2 → *O +*CO_2), and O atom migration to the O vacancy **IV-ts3-V** (*O → $O_{lattice}$). Asterisk symbol indicates adsorbed species. Color coding of elements: orange, Au; lime, Ce; red and magenta, O; blue, adsorbed O_2; gray, C. (Reproduced from Publication III, with permission from the American Chemical Society.)

For comparison, we have also studied CO oxidation on the Au-supported stoichiometric $Ce_{10}O_{20}$ cluster. The reaction path is shown in **Fig. 5.3**, in which the first

CO oxidation with lattice O has an activation barrier of only 0.12 eV; that is even lower than the barrier for the same step on the Au-supported $Ce_{10}O_{19}$ system. This is not unexpected, because the fully oxidized Au-supported $Ce_{10}O_{20}$ cluster has a stronger oxidizing ability than the partially reduced $Ce_{10}O_{19}$ cluster. After the oxidation of the first CO molecule, the $Ce_{10}O_{20}$ cluster becomes $Ce_{10}O_{19}$ with one O vacancy of type **I**. The calculated activation barrier for the following $CO + O_2$ reaction, 0.41 eV, is slightly higher than that calculated above for the same step on the $Ce_{10}O_{18}/Au(111)$ nanoparticle with two O vacancies. Although the idealized stoichiometric ceria particles on Au support probably do not exist, this model may well describe CO oxidation in an oxygen-rich environment. Our calculation shows that the same low-energy mechanism should also be viable on oxidized ceria particles.

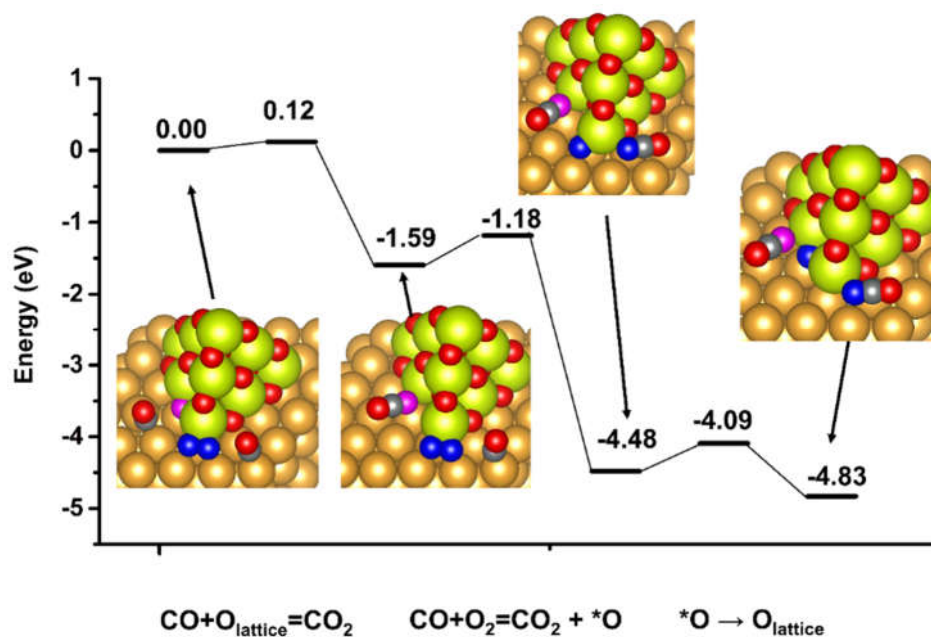**Fig. 5.3** The reaction path of CO oxidation on Au(111)-supported $Ce_{10}O_{20}$ particle. The O atom formed in the second oxidation step migrates to fill the O vacancy. Color coding of elements: orange, Au; lime, Ce; red and magenta, O; blue, adsorbed O_2; gray, C. (Reproduced from Publication III, with permission from the American Chemical Society.)

Chapter 6 CO Oxidation Promoted by a Dynamic Au-CO Complex

Interestingly, recent *ab initio* molecular dynamics (AIMD) simulations by Wang, Li et al. [70, 104] predicted a dynamical extraction of Au single atoms capped by a CO ligand (i.e. Au-CO monocarbonyl species) from Au NPs supported on ceria during CO oxidation. The *in situ* generated Au-CO species diffuse to the ceria support, where it reacts with lattice O of ceria releasing CO_2. Similarly, a formation of mobile Au single atoms presumably in the form of Au-CO complexes was earlier reported in a surface-science study (in an ultra-high vacuum) of CO adsorption on a pitted Au(111) surface aided by DFT calculations.[105] The possibility of a single transition metal atom serving as an active site in heterogeneous catalysts received high attention recently and has been controversially discussed in the literature.[93, 106-107] Remarkably, in our publication IV, an AIMD simulation described below also revealed the formation of a reactive Au-CO complex during CO oxidation on a model catalyst composed of $Ce_{10}O_{19}$ clusters supported on a stepped Au(321) surface.

An initial structure (**Fig**. **6.1a**) for the AIMD simulation was constructed in line with the most favorable O_2 adsorption geometry at a vertex Ce site at the interface. Two CO molecules were placed on top of a 9-fold and 6-fold coordinated Au atom of the Au(321) support. The adsorption energies of the two CO molecules on the Au(321) surface in the presence of the $Ce_{10}O_{19}$ cluster and an adsorbed O_2 molecule were calculated to be -0.84 and -1.11 eV at the 9-fold and 6-fold site, respectively. Starting from this initial structure (**Fig. 6.1a**), we simulated a catalytic reaction between CO and O_2, at 700 K. We found that after 3 ps of the simulation, one of the Au atoms with the adsorbed CO molecule on it was lifted above the Au(111) terrace, forming a mobile linear gold carbonyl species (Au-CO) (**Fig**. **6.2a** and **Fig**. **6.1b**). At 9 ps, the CO ligand of the Au-CO complex was oxidized to CO_2 by a lattice O atom of the $Ce_{10}O_{19}$ nanocluster, creating an oxygen vacancy at the cluster perimeter. The formed CO_2 desorbed within the next 3 ps of the simulation. However, the rest of the simulation of the second CO oxidation reaction failed; thus, we will not dwell on the details here. For the second part of the cycle, we adopted static DFT computation to explore the mechanism as we did for the CO oxidation on the ceria/Au(111) model.
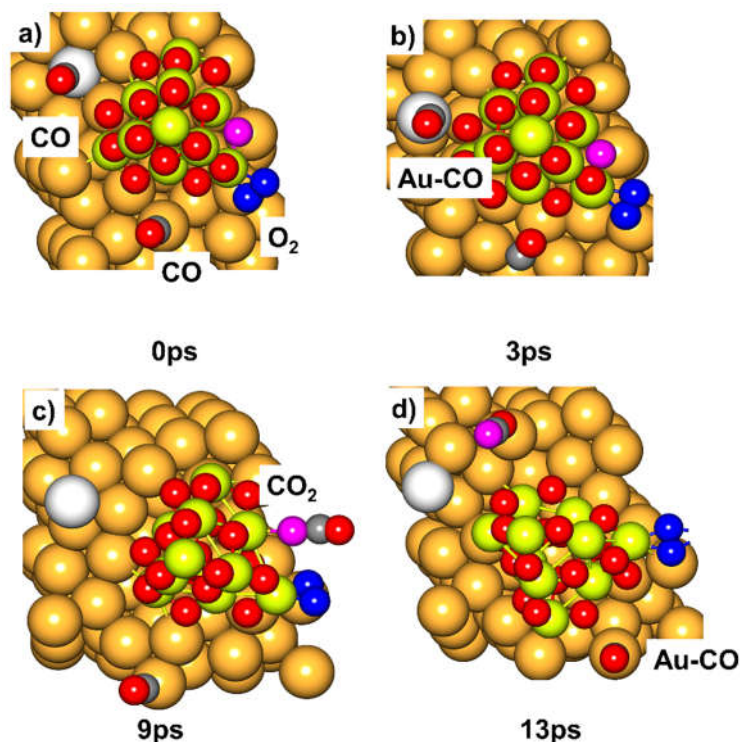
Fig. **6.1** AIMD simulation of Au(321)/Ce$_{10}$O$_{19}$ chemical model for 24 ps at 700 K. Color coding of elements: orange and white, Au; lime, Ce; red and magenta, O; blue, adsorbed O$_2$; gray, C.

We monitored the coordination number (CN) of the extracted Au atom during the first 9-ps simulation, as shown in **Fig**. **6.2**. The CN varies from initially 9 to around 3-4 confirming the formation of the Au-CO fragment lifted above the (111) surface plane and reattachment of the Au atom to a step edge after the CO oxidation (**Fig**. **6.2b**). Furthermore, we compared the charge on the extracted Au atom with adsorbed CO on it before and after Au extraction from the terrace and of the bare Au atom. In **Fig**. **6.2a** and **c**, this Au atom is marked in white. The presence of the reduced ceria particle on the Au surface induces a significant charge transfer from ceria to Au, so that electron density accumulates on the Au surface at the perimeter to the ceria particle, as inferred from a charge density difference analysis (**Fig**. **4.2**). Interestingly, the degree of this charge transfer increases from about -0.08 to -0.23 e due to the adsorption of a CO molecule despite that no significant amount of charge is transferred from the adsorbates to Au. The Au atom becomes positively charged (+0.11 e) after being extracted from the terrace to become an Au-CO complex on the surface. The charge on Au decreases to 0.05 e after the first CO oxidation.

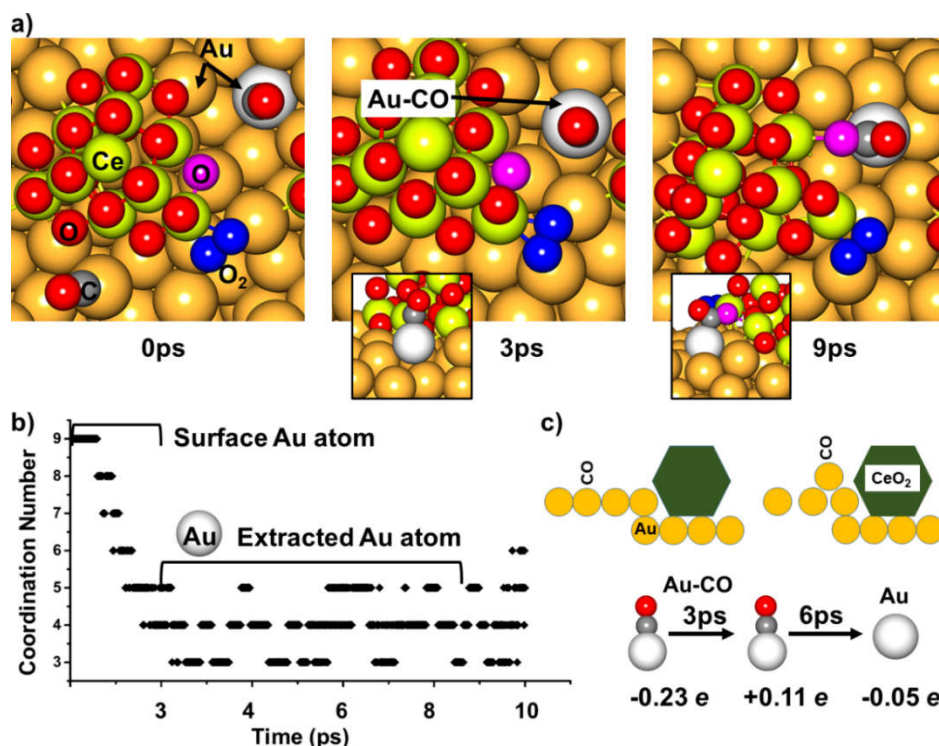**Fig**. **6.2** The extraction of the Au-CO unit during the first CO oxidation. **a)** Selected snapshots of Au-CO unit formation during the AIMD simulation process. **b)** The coordination number (CN) of the dynamic low-coordinated Au atom during AIMD simulation. We only consider Au-to-Au coordination when calculating the CN. **c)** Schematic illustration of Au-CO unit formation and charges on the extracted Au atom during various stages: when it is part of the Au(111) terrace (CN=9), when it is extracted (CN=3~4), and after the CO oxidation by lattice O (CN=5~6).

The energy required for the Au-CO complex extraction from the Au surface on the present $Ce_{10}O_{19}/Au(321)$ model is computed to be -0.51 eV, indicating a thermodynamically favorable process. However, the energy of the same process on the bare gold surface is positive, +0.42 eV. Therefore, the presence of the ceria cluster facilitates the formation of a mobile Au-CO complex.

Based on the reaction mechanism for the first half of the cycle derived from the AIMD simulation and assuming the $CO + O_2$ reaction for the second half of the cycle (as found on the ceria/Au(111) catalyst) we performed "static" DFT computations of the minimum energy reaction path (**Fig**. **6.3**) to determine reaction energies, and activation barriers, which are essential to assess the thermodynamic and kinetic plausibility of the proposed reaction mechanism. We have also considered two other possibilities for the first CO oxidation. Overall, there are three possible pathways: (i) direct oxidization of CO by lattice O of the $Ce_{10}O_{19}$ cluster (**Fig**. **6.4**), (ii) a reaction of CO with the adsorbed O_2 molecule (**Fig**. **6.4**), and (iii) a reaction of the Au-CO complex extracted from the Au terrace with lattice O of the ceria nanoparticle as suggested by

our AIMD simulation (**Fig**. **6.2**). The corresponding transition states for the last possibility are shown in **Fig**. **6.5**. The energetics of the three pathways are compared in **Fig. 6**.**3**. The third pathway including the formation of gold carbonyl and its subsequent oxidation with lattice O of the ceria nanoparticle (**II-ts1-III**) has a very low activation barrier (0.08 eV), implying that this pathway should be kinetically preferable compared to a direct reaction of CO with the adsorbed O atom or O_2 molecule.
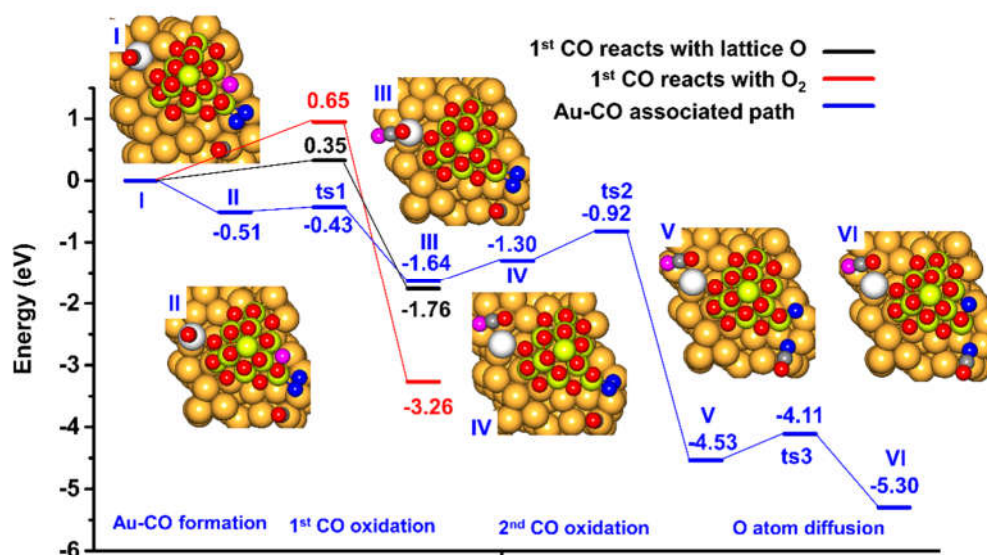

Fig. **6.3**. Theoretically predicted energy profile of the reaction path, geometries of the reactants, intermediates, and products for Au-CO formation, first and second CO oxidation, and O atom diffusion mechanism in the system of the $Ce_{10}O_{19}$ cluster supported on Au(321). The reaction mechanism includes three main steps as follows: **I-II** Au-CO formation; **II-ts1-III** (Au-*CO + $O_{lattice}$ → *CO_2), the first CO oxidation with a lattice O atom of ceria NP; **III-IV-ts2-V** (*CO + *O_2 → *O +*CO_2), the second CO oxidation by activated O_2^{2-}; **V-ts3-VI** (*O → $O_{lattice}$), O atom migrates to O vacancy. Color coding of elements: orange, Au; lime, Ce; red and magenta, O; blue, adsorbed O_2; gray, C.

Next, in the **III-IV-ts2-V** reaction step, the remaining CO molecule is oxidized by the activated O_2^{2-} species forming CO_2 and an O atom coordinated to a corner Ce atom. The activation barrier and reaction energy of this step was computed to be 0.38 eV and -3.23 eV, respectively. The formed CO_2 molecule binds weakly and directly desorbs into the gas phase. The remaining O ad-atom bonding with the corner Ce migrates to the O_V site in the **V-ts3-VI** reaction step with the barrier and reaction energy of 0.42 eV and -0.77 eV, respectively. Our study revealed that CO oxidation catalyzed by ceria NPs supported on np-Au could be facilitated by the formation of transient Au-CO species. Such new finding shows again that the CO oxidation reaction on ceria coated np-Au is far more complicated than might be anticipated.

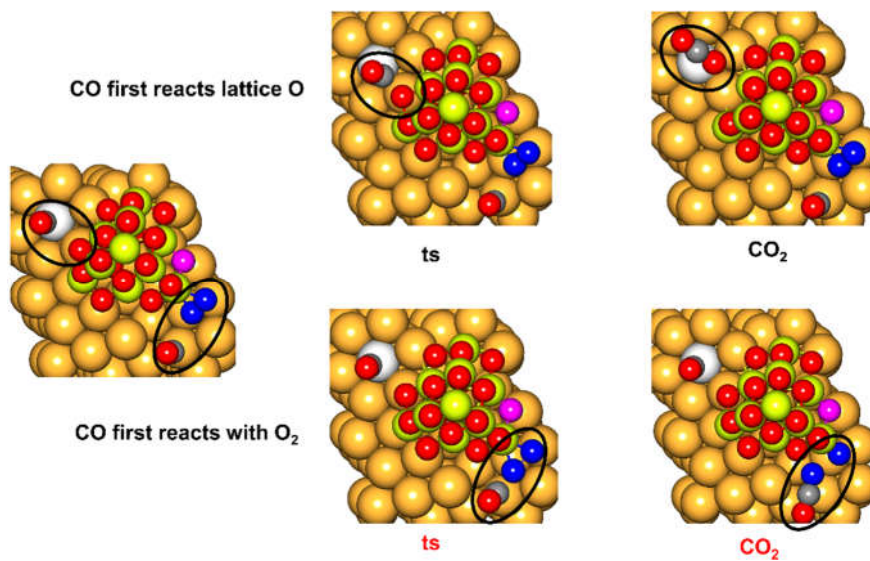**Fig**. **6.4** Alternative reaction paths for the first half-cycle: top, the first CO is oxidized directly by a lattice O atom; bottom, CO reacts with the adsorbed O_2 molecule.
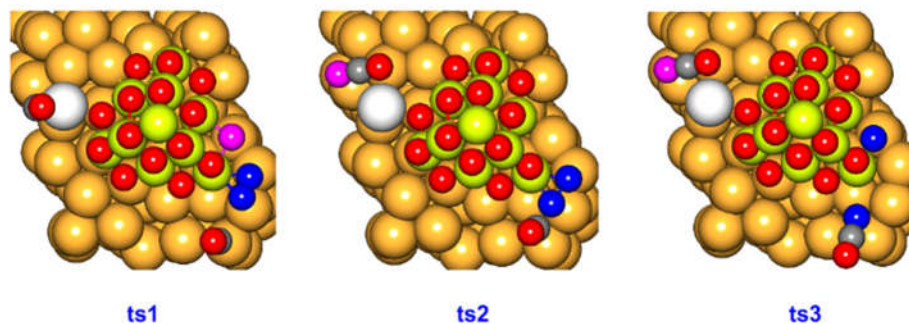

Fig. **6.5** Transition state structures corresponding to the lowest energy (blue) path of **Fig. 6.3**: ts1, Au-CO reacts with a lattice O atom; ts2, CO is oxidized by adsorbed O_2; ts3, O atom diffusion.

46

Chapter 7 Summary and Outlook

In the first part of this dissertation (Chapters 2), AIMD simulations and static DFT computations were carried out to study the dynamics of O-driven surface restructuring, the surface diffusion of Ag, and the formation of 1D and 2D –(Au-O)- chains with the partially covalent character of Au-O bonds. We expect that these processes, which we observed on the stepped Au and AuAg surfaces taken as computational models are relevant to the surface chemistry and reaction dynamics of the nanoporous gold material. In the second part (Chapters 3-6) computational modeling based on conventional static DFT and using AIMD simulations was carried out to interpret the origin of the thermal stability, surface dynamics, and CO oxidation mechanism of ceria-coated nanoporous gold catalyst.

In Chapter 2, the AIMD simulations revealed that the adsorbed surface O atoms dynamically form –(Au–O)– chain structures and lead to surface reconstruction. Ag impurities at a low concentration lower the activation barrier for the gold-oxygen chain formation, whereas the formation of pure Ag-O (–O–Ag–O–) links is energetically slightly unfavorable, especially at high Ag concentration. Besides, the work predicted oxygen-induced segregation of subsurface Ag atoms onto the surface, which tend to migrate to the O-rich areas. A complimentary Auger electron spectroscopy study confirmed this successful prediction.

Chapter 3 introduces a computations study (based on AIMD simulations and static DFT) of the particle-support interaction and redox chemistry of an "inverse" catalyst in which ceria nanoparticles are supported on an extended gold surface. As a computational model, we used ceria clusters with 10 Ce atoms supported on Au(111) and Au(321) model surfaces. It was found that a reduced $Ce_{10}O_{19}$ (with one inner O vacancy at the inner ceria-gold interface), as well as a stoichiometric $Ce_{10}O_{20}$ cluster, are thermodynamically stable on the gold surface, as inferred from AIMD simulations. The most favorable position for O_V formation on the perfect tetrahedral Au-supported $Ce_{10}O_{20}$ cluster is at the center of its bottom facet in contact with the Au surface. This was found on both Au(111) and Au(321) surfaces. This energetically favored O_V formation site is, however, buried inside the ceria/Au interface and, presumably, an O_V at such position cannot be formed directly as a result of O_2 formation or lattice O consumption during a catalytic reaction (e.g. CO + $O_{lattice}$). The formation of an O_V site

at a particle perimeter generates two Ce^{3+} ions with two $4f^1$ unpaired electrons, which are initially localized on ceria rather than get transferred to gold. Nevertheless, the vacancy at this perimeter position is predicted to eventually migrate to a more thermodynamically stable inner interfacial site. This rearrangement is accompanied by a transfer of two unpaired $4f^1$ electrons to gold, which becomes delocalized mainly at interfacial Au atoms. This work also found that both the reduced ($Ce_{10}O_{19}$) and oxidized ($Ce_{10}O_{20}$) ceria clusters supported on Au(111) or Au(321) remain structurally stable during a thermalizing AIMD simulation. The Au(321) surface undergoes restructuring to maximize its favorable interaction with the reduced ceria cluster. We conclude that the overall ceria-to-Au charge transfer and strong adsorption are responsible for the strong particle-support interaction. In contrast, in the conventional catalysts consisting of Au_n nanoparticles supported on a CeO_2 surface, theoretical studies predict that the direction of charge transfer should depend on the reducing or oxidizing environment.[70, 108-110]

Chapter 4 reveals that the charge polarization between the ceria NPs and the Au support leads to an increased electron density at the interface, implying that the ceria-to-Au electron transfer provides electron-rich sites for facile O_2 adsorption and activation. The preferable adsorption site of the O_2 molecule is the bottom corner of the tetrahedral ceria cluster, i.e. at the interface between ceria and gold; the adsorption energies of O_2 are similar on the reduced and stoichiometric ceria cluster models. The CO molecule barely adsorbs on a ceria nanoparticle, instead it binds to a Au support.

Chapter 5 highlights the importance of the perimeter interface between Au and ceria playing a crucial role for CO oxidation in two ways: by supplying active oxygen atoms from the ceria lattice and by providing adsorption sites for O_2 adsorbates. Similar to the findings of Kim and Henkelman for Au_n/CeO_2,[71, 74] the CO oxidation on the inverse catalyst also proceeds according to the Mars-van-Krevelen mechanism, where the CO oxidation with lattice O in the first half of the cycle creates an O vacancy at a perimeter site and the O_2 reaction with CO in the second half of the cycle generates an O atom at a different active site. The generated O atoms migrate to fill-up the formed O vacancies recovering the complete framework of the $Ce_{10}O_{19}$ and closing the catalytic cycle.

In Chapter 6 we report an exciting finding revealed by an AIMD simulation that negative charge accumulation on a stepped Au(321) surface (at the interface region) due to the adsorbed ceria cluster and CO adsorption facilitates the extraction of

individual Au atoms from the Au surface in the form of mobile Au-CO gold carbonyl complexes. The reaction of a Au-CO species with a lattice O atom of ceria at the perimeter of the ceria NP has a very low barrier, efficiently promoting the oxidation reaction. After the CO oxidation, the extracted Au atom quickly attaches to a step edge. Therefore, our work proposes a Mars-van-Krevelen type of mechanism for CO oxidation on a ceria/Au(321) model catalytic system, assisted by the formation of a transient Au-CO complex. In the second step, an O_2 molecule adsorbed at a perimeter interface site of the reduced ceria cluster ($Ce_{10}O_{18}$) reacts with CO, and the generated O atom fills up the previously formed O vacancy at the perimeter to complete the catalytic cycle.

While this work revealed interesting mechanistic details of the O induced surface restructuring, such as –(Au-O)– chain formation and Ag diffusion at the atomic level using AIMD simulations, it only gives a microscopic insight at the level of quantum mechanical modeling and on a short time scale of several tens of ps. Therefore, studies of surface and bulk diffusion processes on a longer time scale and modeling on a meso- and nano-scale are required for a more comprehensive understanding of these diffusion and segregation processes. We should expect a similar effect of CO adsorption (possibly involving a formation of mobile Au-CO species) facilitating Au diffusion and coarsening of nanoporous gold. The atomic-level details of CO-induced surface restructuring remained beyond the scope of the current work but are potentially interesting.

Although the chosen high-index Au(321) surface is characteristic of all possible structural features (steps and kinks) expected on the surfaces of np-Au, and the ceria/Au(321) model provides the first informative insight into the chemistry of np-Au functionalized by ceria, the step density on this surface is rather high, which may not reflect the surface relief everywhere on the np-Au ligaments. Surface models with larger terrace size could provide a better model for np-Au in certain cases, specifically, to model ceria nanoparticles supported on flat parts of np-Au ligaments. A further limitation of the current computational model is that the presence of impurities of a less noble metal (Ag, Cu) in np-Au has not been included in this study, though these species might potentially play important roles in catalysis on np-Au.

As a next step, further extending this work to other important related catalytic systems, we envision studies on composite catalysts comprising other reducible oxides supported on Au surfaces, such as one-component oxides Pr_2O_3 and TiO_2, as well as

mixed oxides (Pr_2O_3/TiO_2, Pr_2O_3/CeO_2, and TiO_2/CeO_2). Expanding the mechanistic studies of inverse oxide-Au catalysts on the basis of electronic-structure calculations to more complex chemical transformations, such as the water-gas shift reaction and oxidation of alcohols and other organic compounds are highly desirable as an important next step addressing problems of current interest related to chemical synthesis.

Chapter 8 Theory and Computational Details

8.1 Density Functional Theory

Quantum mechanics was officially born after the discovery of the Schrödinger equation and matrix mechanics, and their subsequent application to interpret the bonding mechanism of the hydrogen molecule in 1927, marking the birth of quantum chemistry. The application of wavefunction theory and density functional theory (DFT) to solve the Schrödinger equation of many-body systems, along with the rapid development of supercomputers and advances in software development, made computational studies of chemical reactions, chemical and physical properties of various molecules and extended systems at the atomic and molecular level affordable and routinely performed by hundreds of thousands of scientists worldwide. In this dissertation, DFT-based methods including molecular dynamics and static computations were applied to investigate structural and chemical properties of nanoporous gold catalysts.

The most important task of computational chemistry is to obtain the many-electron wavefunction of a model system under consideration by solving the Schrödinger equation. The nonrelativistic time-independent Schrödinger equation of a single particle in its most general form is given as follows:

$$E\psi_E(r) = \left[-\frac{\hbar^2}{2m}\nabla^2 + V(r)\right]\psi_E(r) \tag{8.1}$$

where, E is energy, $\hbar$ is reduced Planck constant, ψ_E is the state vector, ∇^2 is the Laplacian, V is the potential due to a uniform electric field. In quantum chemistry, three major simplifications are usually applied to the Schrödinger equation: the adiabatic (Born-Oppenheimer) approximation, nonrelativistic approximation, and mean-field approximation in a so-called Hartree-Fock solution.[111] Due to adopting the mean-field approximation in the Hartree-Fock method, the computed energy is always higher than the true energy of a many-body system. A deviation originates from omitting the "electron correlation", a term that collectively describes all effects neglected due to the use of the mean-field approximation. These effects refer to the interaction between electrons, specifically, Coulomb correlation neglected in the Hartree-Fock method. To more accurately describe physical and chemical properties of systems, so-called "post-Hartree-Fock methods", such as configuration interaction, many-body perturbation theory, coupled-cluster theory, and multi-configurational self-consistent field have been

developed. These more computationally expensive methods are able to approximately include electron correlation effects.

Compared to the Hartree-Fock method, the density functional theory (DFT) can greatly reduce the computational cost of solving the Schrödinger equation for many-body systems. The DFT is being broadly used in physics, chemistry and material science to investigate the electronic structure of atoms, molecules, and condensed matter. According to the Hohenberg-Kohn theorem,[112-113] the total ground-state energy of a many-electron system E_0 is a functional of its electron density:

$$E_0[\rho_0] = T[\rho_0] + E_{ee}[\rho_0] + E_{Ne}[\rho_0] \qquad (8.2)$$

where T is the kinetic energy, whereas E_{ee} and E_{Ne} denote the potential energy due to electron-electron and nuclei-electron interaction, respectively. In other words, the ground state density uniquely determines the potential and thus all properties of the system, including the many-body wave function.

The next crucial step comes from (re)-introducing single-particle wave functions (orbitals). Kohn and Sham (KS) suggested an approach,[113] in which one defines a set of fictitious non-interacting electrons that by definition have the same density as the actual interacting problem. Like in the Hartree-Fock theory, the wavefunction of such a non-interacting system of KS electrons is a Slater determinant. The KS electrons thus satisfy a non-interacting Schrödinger equation:

$$\left\{-\frac{1}{2}\nabla^2 + v_S(\boldsymbol{r})\right\}\psi_\mu(\boldsymbol{r}) = \epsilon_\mu\psi_\mu(\boldsymbol{r}) \qquad (8.3)$$

where $v_S(\boldsymbol{r})$ is the effective KS potential, and $\psi_\mu(\boldsymbol{r})$ are the KS orbitals. The connection of this fictitious system to our real system of interacting electrons is now established by choosing the effective potential $v_S(\boldsymbol{r})$ such that the density resulting from the summation of the moduli of the squared orbitals $\psi_\mu(\boldsymbol{r})$ exactly equals the ground state density of our real target system of interacting electrons:

$$\rho(\boldsymbol{r}) = 2\sum_\mu^{occ}|\psi_\mu(\boldsymbol{r})|^2. \qquad (8.4)$$

The total energy E is the sum of ϵ_μ. If we write the energy in terms of KS quantities, we get (compare with eq. (8.2)):

$$E[\rho] = T_S[\rho] + J[\rho] + E_{Ne}[\rho] + E_{xc}[\rho] \qquad (8.5)$$

where T_S is the kinetic energy of non-interacting electrons, J is the interelectron repulsion approximated by the classical electrostatic energy of a charge distribution with itself, called the Hartree energy:

$$J[\rho] = \frac{1}{2}\int \frac{\rho(r)\rho(r\prime)}{|r-r\prime|}\,dr\,dr' \tag{8.6}$$

The nuclear-electron repulsion term E_{Ne} is the same as in eq. (8.2) and the last term E_{xc} called *exchange-correlation energy* accounts for the difference ($T[\rho] - T_S[\rho]$) + ($E_{ee}[\rho_0] - J[\rho]$), i.e. the difference between the true and KS kinetic energy and the difference between the true electron-electron interaction energy and the Hartree energy.

The Kohn-Sham Hamilton is represented as:

$$\hat{H} = -\frac{1}{2}\nabla^2 - \sum_A \frac{Z_A}{|r-R_A|} + \int \frac{\rho(r')}{|r-r'|}\,dr' + V_{XC}[\rho(r)] \tag{8.7}$$

where, $V_{XC}[\rho(r)]$ is the exchange-correlation potential. Unfortunately, the exact form of the exchange-correlation energy and the corresponding potential is unknown. Various approximate functionals have been developed. The generalized gradient approximation (GGA) provides a very good compromise between computational cost and accuracy. In its general form a GGA functional is expressed as:

$$E_{XC}^{GGA}[\rho] = \int f(\rho, \nabla\rho)d^3r \tag{8.8}$$

By using the GGA approximation, quite accurate computation of exchange-correlation energy for chemical systems in the ground-state can be achieved. In this dissertation, the GGA approximation has been applied in the parameterization of Perdew-Burke-Ernzerhof (PBE).

The treatment of strongly correlated *f*-block elements (such as Ce) is beyond the accurate computation of DFT due to the mean-field approximation of used in solving the Kohn-Sham equation of the system. The strongly correlated and strongly coulomb repulsive *f*-electron shells with narrow energy bands are incorrectly described by conventional density functional methods. The GGA+U approach with an additional Hubbard *U* term can be introduced in DFT calculations to treat the strong on-site Coulomb interaction of localized *f*-electrons,[114] which is not correctly described by a GGA functional. The strength of this interaction is usually described by two parameters: the on-site Coulomb term *U* and the site-exchange term *J* that can be estimated from ab-initio calculations, or usually obtained by fitting to experimental data.

8.2 Bloch's Theorem

For a many-body system, the potential $V(r)$ of the Hamiltonian (cf. **Eq. 8.1**) is expressed in terms of the Kohn-Sham theory as:

$$V(\mathbf{r}) = -\sum_A \frac{Z_A}{|\mathbf{r}-\mathbf{R}_A|} + \int \frac{\rho(\mathbf{r}')}{|\mathbf{r}-\mathbf{r}'|} d\mathbf{r}' + V_{XC}(\mathbf{r}). \qquad (8.9)$$

In a periodic system, directly computing the electron density $\rho(\mathbf{r})$ and the potential $V(\mathbf{r})$, or solving KS equations is impossible because the system extends infinitely in three dimensions. However, by bringing the assumption of a periodic potential:

$$V(\mathbf{r}) = V(\mathbf{r} + \mathbf{R}) \qquad (8.10)$$

where $\mathbf{R}$ is the lattice translation vector, the description of the system is therefore reduced to a finite unit cell. The wave function of electrons can be written as a modulated plane wave:

$$\psi_n(\mathbf{r}) = u_k(\mathbf{r})e^{ikr} \qquad (8.11)$$

where $\mathbf{k}$ is a vector, $u_k(\mathbf{r})$ is a periodic function that is expressed as:

$$u_k(\mathbf{r}) = u_k(\mathbf{r} + \mathbf{R}). \qquad (8.12)$$

The solutions of the Schrödinger equation for a periodic system are characterized by an integer number n (band index) and a vector $\mathbf{k}$:

$$\left[-\frac{1}{2}\nabla^2 - V(\mathbf{r})\right]\psi_{n,k}(\mathbf{r}) = E_{n,k}\psi_{n,k}(\mathbf{r}). \qquad (8.13)$$

The electronic structure and other properties of extended systems can be accurately computed through solving the Kohn-Sham equations for a periodic Kohn-Sham potential.

8.3 *Ab Initio* Molecular Dynamics

Molecular dynamics (MD) is a computational approach in which a system of atoms is forced to motion. The simulation of the motion is technically accomplished by numerically solving Newton's equations of motion of interacting particles. MD describes interaction of atoms and molecules and their motion in space as a result of these interactions. The system is propagated to generate a trajectory describing its evolution over the course of the simulation. Relevant properties can be calculated for each "snapshot" (a stored configuration of the system) and averaged over the entire trajectory to compute estimates of desired properties. An MD simulation can provide information on thermodynamic and dynamic properties of a system. If a quantum mechanical description of matter is used, electrons are explicitly represented in the model and interaction energy is calculated at each time step by performing a full quantum-chemical calculation of the electronic structure of the system. This type of

MD simulation is called *ab initio* molecular dynamics (AIMD). AIMD allows to simulate bong making and breaking processes, i.e. chemical reactions, even electron transfer reactions. While conventional static DFT computations can only predict the geometric, electronic structure, and reaction energy at 0 K, AIMD simulations can predict diffusion, structure evolution, chemical reactions at various temperatures. The method is thus applied in chemical physics, materials science, and biophysics. Its wide application is, however, limited by a very high computational cost. For the same reason, computationally tractable system size is limited to ~100 of atoms and the time scale of such a simulation is limited to a few tens of ps.

In a given potential $V(\mathbf{r}_1, \cdots, \mathbf{r}_N)$ for a system consisting of N particles, the force acting on every particle is determined by the gradient (vector of the first derivatives) of the potential with respect to atomic displacements. The force acting on the *i*-th atom is represented as:

$$F_i = -\nabla_{r_i} V(r_i, \cdots, r_N) = -(\frac{\partial V}{\partial x_i}, \frac{\partial V}{\partial y_i}, \frac{\partial V}{\partial z_i}) \tag{8.14}$$

In an *ab initio* molecular dynamics simulation,[115-116] the forces acting on atoms are given by the gradient of energy obtained from an *ab initio* quantum chemical computation.

The position of a particle at time $t + \Delta t$ can be expressed as:

$$r_i(t + \Delta t) \cong 2r_i(t) - r_i(t - \Delta t) + \frac{F_i(t)}{m_i} \Delta t^2 \tag{8.15}$$

The time step Δt is determined by fast motions in the system; for example, the O-H bond vibrates with periods of several femtoseconds, implying that Δt should be on a sub-femtosecond scale to ensure observation of the O-H bond formation or breaking during an AIMD simulation.

The radial distribution function $g(r) \, dr_i$ defines the probability of finding a particle at a distance r from another reference particle:

$$g(r) = \frac{dN}{4\pi r^2 \rho.\text{dr}} \tag{8.16}$$

where *dN* is the number of particles in the area between r and $r + dr$ and ρ is the average density of the system.

The diffusion coefficient can be calculated using Einstein's relation

$$D = \frac{1}{6nt} \lim_{t \to \infty} < \sum_{i=1}^{n} [(r_i(t) - r_i(0)]^2 > \tag{8.17}$$

where, the $r_i(0)$ is the initial position of the ith atom and $r_i(t)$ represents the ith atom's

position at t moment; n represents the total number of atoms.

8.4 Computational Details

In the publications summarized in this doctoral dissertation, a combination of *ab initio* molecular dynamics (AIMD) simulations and standard (static) DFT methods has been applied. AIMD simulations allow us to explore the time-evolution of complex condensed-phase systems at a given temperature and to find low-energy reaction pathways and the global minimum of geometries; the static DFT was used to compute activation barriers, which are not directly available from AIMD. The AIMD simulations were performed using the CP2K program package.[117] The generalized-gradient approximation in the parameterization of Perdew, Burke, and Ernzerhof (PBE)[118-119] was used to compute the exchange-correlation energy. The choice of the PBE functional was made considering its very good accuracy in describing bulk properties of transition metals.[120-121] The hybrid Gaussian and plane-wave (GPW) basis sets at the level of double-ζ valence plus polarization (DZVP)[122-123] were applied to describe the valence electrons of all elements ($5d^{10}6s^1$ for Au, $4f^1 5s^2 5p^6 5d^1 6s^2$ for Ce, $4d^{10}5s^1$ for Ag, $2s^2 2p^4$ for O, and $2s^2 2p^2$ for C), and auxiliary plane-wave basis sets with the cutoff energy of 500 Rydberg were adopted. Core electrons were described with scalar relativistic norm-conserving pseudopotentials.[124] Brillouin zone integration was performed with a reciprocal space mesh consisting of only the gamma point. In the simulations, the Nose–Hoover thermostat (NVT) was used to sample from the canonical ensemble.[115, 125] The relatively short time scales of AIMD (time step of 1.0 fs and the total time of a simulation run of up to 30 ps) limit the sampling to fast and low-energy-barrier events. To rapidly explore a large phase space volume of surface configurations, statistical sampling was performed at an elevated temperature of 700 K. The applied simulation times and temperature ensure that reactions occurring at room temperature at the time-scale of nanoseconds can be observed on a short time-scale of picoseconds. Assuming a simple Arrhenius rate law and a preexponential factor of 10^{13} s^{-1}, a process with $E_a = 0.3$ eV would occur on a timescale of ~10-15 ps at 700 K, whereas the same process would require >10 ns at 300 K. The structures were relaxed until the force acting on each atom was $\leq 2 \times 10^{-2}$ eV Å^{-1}. Transition states (TSs) were determined by applying the nudged elastic band (NEB) method.[126] Some of the "static" DFT calculations were

performed using the plane-wave based VASP code[127-128] and a projector augmented wave (PAW) method [129-130] with an energy cutoff of 415 eV.
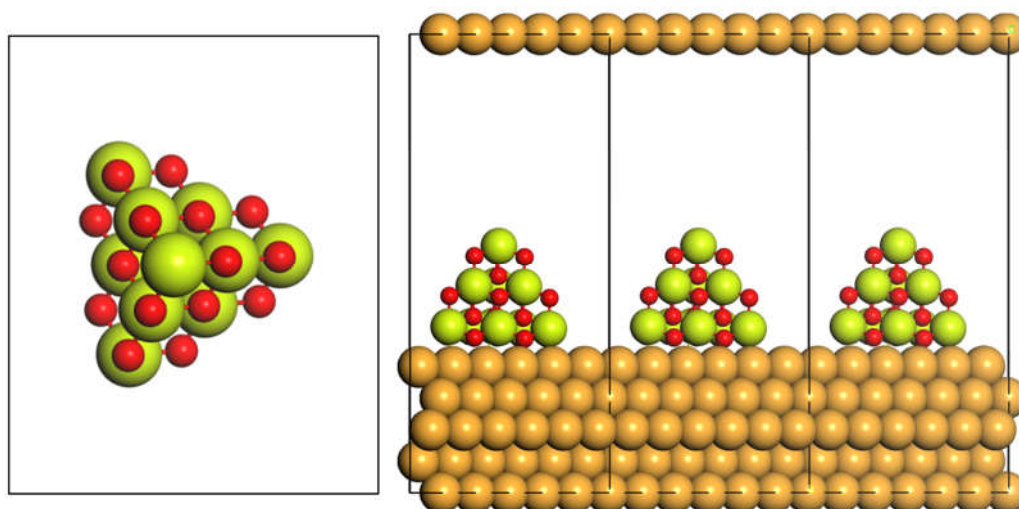

Fig. 8.1 Periodic models. Left: a unit cell used for calculating a free ceria particle. Right: a periodic slab model used for modeling surfaces with adsorbates.

All calculations were performed using periodic models (**Fig. 8.1**). In our modeling, we approximated the np-Au support by periodic single-crystal surfaces Au(111) and Au(321). For such surfaces with well-defined periodicity, "slab models" are used to represent. The surface is modeled by a slab of finite thickness of a few atomic layers parallel to the (*hkl*) crystal plane if interest. A so-called "supercell", such as depicted in **Fig. 8.1**, usually consists of several minimal unit cells along each crystallographic direction parallel to the surface and is periodically repeated in three dimensions along the cell vectors. In the direction orthogonal to the surface crystal plane, empty space called "vacuum" is included to ensure that periodically repeated slabs do not interact with each other. A $p(3\times2)$ unit cell of a regular Au(321) surface with the slab thickness of ~12 Å and ~18 Å vacuum space was employed in publications I and II (Chapter 1). In the studies of ceria functionalized nanoporous gold (publications III and IV) we adopted a tetrahedral cluster $Ce_{10}O_{20}$ model (or its reduced version $Ce_{10}O_{19}$) adsorbed on the Au(111) and Au(321) surfaces. The Au(111) surface was modeled using a $p(5\times5)$ unit cell with a slab thickness of 5 atomic layers and ~24 Å vacuum space. To model the Au(321) surface, a $p(3\times2)$ unit cell with 12 Å slab thickness and a vacuum spacing of 28 Å in the Z direction was used. The $Ce_{10}O_{20/19}$ nanocluster was placed on the Au(111) and Au(321) slab models. In this way, realistic computational models reflecting key local structural features of the ceria-coated np-Au catalyst were constructed.

Here we describe the definitions used in the calculations of vacancy formation and adsorption energies adopted in this thesis. The vacancy formation energies $E(O_V)$ are referenced to one half of the total energy of the O_2 molecule, as it has been widely adopted in theoretical studies, and calculated via the following equation:

$$E(O_V) = E(Ce_{10}O_{20}/Au_{surf}) - 1/2E(O_2) - E(Ce_{10}O_{19}/Au_{surf}) \qquad (8.18)$$

where $E(Ce_{10}O_{20}/Au_{surf})$ and $E(Ce_{10}O_{19}/Au_{surf})$ are the DFT-calculated energies of the stoichiometric and the reduced model with one oxygen vacancy, respectively, and $E(O_2)$ is the energy of the gas-phase O_2 molecule. The Au_{surf} represents Au(111) or Au(321) surface. An analogous expression was used for calculating $E(O_V)$ in a free ceria particle. The adsorption energy E_{ad} of the $Ce_{10}O_{19/20}$ clusters on Au surface was calculated using the following equation:

$$E_{ad} = E(Ce_{10}O_{19/20}/Au_{surf}) - E(Ce_{10}O_{19/20}) - E(Au_{surf}) \qquad (8.19)$$

where $E(Ce_{10}O_{19/20}/Au_{surf})$, $E(Ce_{10}O_{19/20})$, and $E(Au_{surf})$ are the computed total energies of the composite system $Ce_{10}O_{20}/Au_{surf}$, the $Ce_{10}O_{19/20}$ cluster and the Au_{surf} slab, respectively. Similarly, the adsorption energies of O_2 and CO on one or two-component systems were calculated according to the general equation:

$$E_{ad} = E(X\text{-Surf}) - E(\text{Surf}) - E(X) \qquad (8.20)$$

where X stands for CO or O_2, $E(X\text{-Surf})$, $E(\text{Surf})$, and $E(X)$ are the computed total energies of the adsorption complex, catalyst without adsorbate, and of the adsorbate molecule X in the gas phase, respectively.

References

1. Pyykko, P., Relativistic effects in structural chemistry. *Chem. Rev.* **1988,** *88* (3), 563-594.

2. Pyykko, P.; Desclaux, J. P., Relativity and the periodic system of elements. *Acc. Chem. Res.* **1979,** *12* (8), 276-281.

3. Haruta, M.; Kobayashi, T.; Sano, H.; Yamada, N., Novel Gold Catalysts for the Oxidation of Carbon Monoxide at a Temperature far Below 0 ^{o} C. *Chem. Lett.* **1987,** *16* (2), 405-408.

4. Mikami, Y.; Dhakshinamoorthy, A.; Alvaro, M.; Garcia, H., Catalytic activity of unsupported gold nanoparticles. *Catal. Sci. Technol.* **2013,** *3* (1), 58-69.

5. Hvolbæk, B.; Janssens, T. V. W.; Clausen, B. S.; Falsig, H.; Christensen, C. H.; Nørskov, J. K., Catalytic activity of Au nanoparticles. *Nano Today* **2007,** *2* (4), 14-18.

6. Haruta, M., Gold as a novel catalyst in the 21st century: Preparation, working mechanism and applications. *Gold Bull.* **2004,** *37* (1-2), 27-36.

7. Corma, A.; Garcia, H., Supported gold nanoparticles as catalysts for organic reactions. *Chem. Soc. Rev.* **2008,** *37* (9), 2096-2126.

8. Ansar, S. M.; Kitchens, C. L., Impact of gold nanoparticle stabilizing ligands on the Colloidal Catalytic Reduction of 4-Nitrophenol. *ACS. Catal.* **2016,** *6* (8), 5553-5560.

9. Vogel, W.; Cunningham, D. A. H.; Tanaka, K.; Haruta, M., Structural analysis of Au/Mg(OH)$_2$ during deactivation by debye function analysis. *Catal. Lett.* **1996,** *40* (3), 175-181.

10. Lopez, N.; Nørskov, J. K., Catalytic CO oxidation by a gold nanoparticle: A density functional study. *J. Am. Chem. Soc.* **2002,** *124* (38), 11262-11263.

11. Grunwaldt, J.-D.; Maciejewski, M.; Becker, O. S.; Fabrizioli, P.; Baiker, A., Comparative study of Au/TiO$_2$ and Au/ZrO$_2$ catalysts for low-temperature CO oxidation. *J. Catal.* **1999,** *186* (2), 458-469.

12. Hvolbæk, B.; Janssens, T. V.; Clausen, B. S.; Falsig, H.; Christensen, C. H.; Nørskov,

J. K., Catalytic activity of Au nanoparticles. *Nano today* **2007,** *2* (4), 14-18.

13. Lopez, N.; Janssens, T.; Clausen, B.; Xu, Y.; Mavrikakis, M.; Bligaard, T.; Nørskov, J. K., On the origin of the catalytic activity of gold nanoparticles for low-temperature CO oxidation. *J. Catal.* **2004,** *223* (1), 232-235.

14. Lopez, N.; Nørskov, J. K.; Janssens, T.; Carlsson, A.; Puig-Molina, A.; Clausen, B.; Grunwaldt, J.-D., The adhesion and shape of nanosized Au particles in a Au/TiO$_2$ catalyst. *J. Catal.* **2004,** *225* (1), 86-94.

15. Mills, G.; Gordon, M. S.; Metiu, H., Oxygen adsorption on Au clusters and a rough Au (111) surface: The role of surface flatness, electron confinement, excess electrons, and band gap. *J. Chem. Phys.* **2003,** *118* (9), 4198-4205.

16. Chen, M.; Cai, Y.; Yan, Z.; Goodman, D. W., On the origin of the unique properties of supported Au nanoparticles. *J. Am. Chem. Soc.* **2006,** *128* (19), 6341-6346.

17. Wörz, A. S.; Heiz, U.; Cinquini, F.; Pacchioni, G., Charging of Au atoms on TiO$_2$ thin films from CO vibrational spectroscopy and DFT calculations. *J. Phys. Chem. B* **2005,** *109* (39), 18418-18426.

18. Madsen, G. K.; Hammer, B., Effect of subsurface Ti-interstitials on the bonding of small gold clusters on rutile TiO$_2$ (110). *J. Chem. Phys.* **2009,** *130* (4), 044704.

19. Remediakis, I. N.; Lopez, N.; Nørskov, J. K., CO oxidation on rutile-supported Au nanoparticles. *Angew. Chem. Int. Ed.* **2005,** *44* (12), 1824-1826.

20. Wang, J.; Hammer, B., Oxidation state of oxide supported nanometric gold. *Top Catal.* **2007,** *44* (1-2), 49-56.

21. Zhang, C.; Michaelides, A.; King, D. A.; Jenkins, S. J., Positive charge states and possible polymorphism of gold nanoclusters on reduced ceria. *J. Am. Chem. Soc.* **2010,** *132* (7), 2175-2182.

22. Fu, Q.; Saltsburg, H.; Flytzani-Stephanopoulos, M., Active nonmetallic Au and Pt species on ceria-based water-gas shift catalysts. *Science* **2003,** *301* (5635), 935-938.

23. Liu, Z.-P.; Jenkins, S. J.; King, D. A., Origin and activity of oxidized gold in water-gas-shift catalysis. *Phys. Rev. Lett.* **2005,** *94* (19), 196102.

24. Wang, J.; Hammer, B., Role of Au$^+$ in supporting and activating Au$_7$ on TiO$_2$ (110). *Phys. Rev. Lett.* **2006,** *97* (13), 136107.

25.   Wu, H.; Liotta, L. F., Metal-support interaction effects on gold catalysts over reducible oxides. In *Heterogeneous Gold Catalysts and Catalysis*, RSC publishers: Oxfordshire, UK: 2014; pp 462-488.

26. Jin, R., Quantum sized, thiolate-protected gold nanoclusters. *Nanoscale* **2010,** *2* (3), 343-362.

27. Nimmala, P. R.; Yoon, B.; Whetten, R. L.; Landman, U.; Dass, A., $Au_{67}(SR)_{35}$ nanomolecules: Characteristic size-specific optical, electrochemical, structural properties and first-principles theoretical analysis. *J. Phys. Chem. A* **2013,** *117* (2), 504-517.

28. Rambukwella, M.; Sementa, L.; Barcaro, G.; Fortunelli, A.; Dass, A., Organosoluble $Au_{102}(SPh)_{44}$ nanomolecules: synthesis, ssolation, compositional assignment, core conversion, optical spectroscopy, electrochemistry, and theoretical analysis. *J. Phys. Chem. C* **2015,** *119* (44), 25077-25084.

29. Kwak, K.; Thanthirige, V. D.; Pyo, K.; Lee, D.; Ramakrishna, G., Energy gap law for exciton dynamics in gold cluster molecules. *J. Phys. Chem. Lett.* **2017,** *8* (19), 4898-4905.

30. Wang, L.-S., Covalent gold. *Phys. Chem. Chem. Phys.* **2010,** *12* (31), 8694-8705.

31. Liu, W.; Zhu, Y. F.; Jiang, Q., Oxidation behavior of CO catalyzed by several decahedral Au clusters: role of cluster stability and electric field. *J. Phys. Chem. C* **2010,** *114* (49), 21094-21099.

32. Stenlid, J. H.; Brinck, T., Extending the σ-Hole concept to metals: An electrostatic interpretation of the eEffects of nanostructure in gold and platinum catalysis. *J. Am. Chem. Soc.* **2017,** *139* (32), 11012-11015.

33. Liu, X.; He, L.; Liu, Y.-M.; Cao, Y., Supported gold catalysis: from small molecule activation to green chemical synthesis. *Acc. Chem. Res.* **2014,** *47* (3), 793-804.

34. Zielasek, V.; Jürgens, B.; Schulz, C.; Biener, J.; Biener, M. M.; Hamza, A. V.; Bäumer, M., Gold catalysts: nanoporous gold foams. *Angew. Chem. Int. Ed.* **2006,** *45* (48), 8241-8244.

35. Xu, C.; Su, J.; Xu, X.; Liu, P.; Zhao, H.; Tian, F.; Ding, Y., Low temperature CO oxidation over unsupported nanoporous gold. *J. Am. Chem. Soc.* **2007,** *129* (1), 42-43.

36. Biener, M. M.; Biener, J.; Wichmann, A.; Wittstock, A.; Baumann, T. F.; Bäumer, M.; Hamza, A. V., ALD Functionalized nanoporous gold: thermal stability, mechanical properties, and catalytic activity. *Nano Lett.* **2011,** *11* (8), 3085-3090.

37. Yan, M.; Jin, T.; Ishikawa, Y.; Minato, T.; Fujita, T.; Chen, L.-Y.; Bao, M.; Asao, N.; Chen, M.-W.; Yamamoto, Y., Nanoporous gold catalyst for highly selective semihydrogenation of alkynes: remarkable effect of amine additives. *J. Am. Chem. Soc.* **2012,** *134* (42), 17536-17542.

38. Wittstock, A.; Zielasek, V.; Biener, J.; Friend, C. M.; Bäumer, M., Nanoporous gold catalysts for selective gas-phase oxidative coupling of methanol at low temperature. *Science* **2010,** *327* (5963), 319.

39. Takale, B. S.; Feng, X.; Lu, Y.; Bao, M.; Jin, T.; Minato, T.; Yamamoto, Y., Unsupported nanoporous gold catalyst for chemoselective hydrogenation reactions under low pressure: effect of residual silver on the reaction. *J. Am. Chem. Soc.* **2016,** *138* (32), 10356-10364.

40. Chen, A. Y.; Shi, S. S.; Liu, F.; Wang, Y.; Li, X.; Gu, J. F.; Xie, X. F., Effect of annealing atmosphere on the thermal coarsening of nanoporous gold films. *Appl. Surf. Sci.* **2015,** *355*, 133-138.

41. Fujita, T.; Tokunaga, T.; Zhang, L.; Li, D.; Chen, L.; Arai, S.; Yamamoto, Y.; Hirata, A.; Tanaka, N.; Ding, Y.; Chen, M., Atomic Observation of catalysis-induced nanopore coarsening of nanoporous gold. *Nano Lett.* **2014,** *14* (3), 1172-1177.

42. Sun, Y.; Burger, S. A.; Balk, T. J., Controlled ligament coarsening in nanoporous gold by annealing in vacuum versus nitrogen. *Philosophical Magazine* **2014,** *94* (10), 1001-1011.

43. Zugic, B.; Wang, L.; Heine, C.; Zakharov, D. N.; Lechner, B. A. J.; Stach, E. A.; Biener, J.; Salmeron, M.; Madix, R. J.; Friend, C. M., Dynamic restructuring drives catalytic activity on nanoporous gold-silver alloy catalysts. *Nat. Mater.* **2017,** *16* (5), 558-564.

44. Fujita, T.; Guan, P.; McKenna, K.; Lang, X.; Hirata, A.; Zhang, L.; Tokunaga, T.; Arai, S.; Yamamoto, Y.; Tanaka, N., Atomic origins of the high catalytic activity of nanoporous gold. *Nat. Mater.* **2012,** *11* (9), 775-780.

45. Moskaleva, L. V.; Röhe, S.; Wittstock, A.; Zielasek, V.; Klüner, T.; Neyman, K. M.; Bäumer, M., Silver residues as a possible key to a remarkable oxidative catalytic activity of nanoporous gold. *Phys. Chem. Chem. Phys.* **2011,** *13* (10), 4529-4539.

46. Déronzier, T.; Morfin, F.; Lomello, M.; Rousset, J.-L., Catalysis on nanoporous gold–silver systems: Synergistic effects toward oxidation reactions and influence of the surface composition. *J. Catal.* **2014,** *311*, 221-229.

47. Biener, J.; Biener, M. M.; Madix, R. J.; Friend, C. M., Nanoporous gold: understanding the origin of the reactivity of a 21st century catalyst made by pre-columbian technology. *ACS. Catal.* **2015,** *5* (11), 6263-6270.

48. Moskaleva, L. V.; Weiss, T.; Klüner, T.; Bäumer, M., Chemisorbed oxygen on the Au(321) surface alloyed with silver: a first-principles investigation. *J. Phys. Chem. C* **2015,** *119* (17), 9215-9226.

49. Dononelli, W.; Tomaschun, G.; Klüner, T.; Moskaleva, L. V., Understanding oxygen activation on nanoporous gold. *ACS. Catal.* **2019,** *9* (6), 5204-5216.

50. Moskaleva, L. V.; Zielasek, V.; Klüner, T.; Neyman, K. M.; Bäumer, M., CO oxidation by co-adsorbed atomic O on the Au(321) surface with Ag impurities: A mechanistic study from first-principles calculations. *Chem. Phys. Lett.* **2012,** *525-526*, 87-91.

51. Zugic, B.; Wang, L.; Heine, C.; Zakharov, D. N.; Lechner, B. A. J.; Stach, E. A.; Biener, J.; Salmeron, M.; Madix, R. J.; Friend, C. M., Dynamic restructuring drives catalytic activity on nanoporous gold-silver alloy catalysts. *Nat. Mater.* **2017,** *16* (5), 558-564.

52. Schaefer, A.; Ragazzon, D.; Wittstock, A.; Walle, L. E.; Borg, A.; Bäumer, M.; Sandell, A., Toward controlled modification of nanoporous gold. a detailed surface science study on cleaning and oxidation. *J. Phys. Chem. C* **2012,** *116* (7), 4564-4571.

53. Fajín, J. L. C.; Cordeiro, M. N. D. S.; Gomes, J. R. B., Adsorption of atomic and molecular oxygen on the Au(321) surface: DFT study. *J. Phys. Chem. C* **2007,** *111* (46), 17311-17321.

54. Fajín, J. L. C.; Cordeiro, M. N. D. S.; Gomes, J. R. B., DFT study of the Au(321) surface reconstruction by consecutive deposition of oxygen atoms. *Surf. Sci.* **2008,** *602*

(2), 424-435.

55. Shi, H.; Stampfl, C., First-principles investigations of the structure and stability of oxygen adsorption and surface oxide formation at Au(111). *Phys. Rev. B* **2007,** *76* (7), 075327.

56. Landmann, M.; Rauls, E.; Schmidt, W. G., First-principles calculations of clean Au(110) surfaces and chemisorption of atomic oxygen. *Phys. Rev. B* **2009,** *79* (4), 045412.

57. Hiebel, F.; Montemore, M. M.; Kaxiras, E.; Friend, C. M., Direct visualization of quasi-ordered oxygen chain structures on Au(110)-(1 × 2). *Surf. Sci.* **2016,** *650*, 5-10.

58. Zhang, C.; Michaelides, A.; Jenkins, S. J., Theory of gold on ceria. *Phys. Chem. Chem. Phys.* **2011,** *13* (1), 22-33.

59. Paier, J.; Penschke, C.; Sauer, J., Oxygen defects and surface chemistry of ceria: quantum chemical studies compared to experiment. *Chem. Rev.* **2013,** *113* (6), 3949-3985.

60. Shi, J., On the Synergetic catalytic effect in heterogeneous nanocomposite catalysts. *Chem. Rev.* **2013,** *113* (3), 2139-2181.

61. Rodriguez, J. A.; Ma, S.; Liu, P.; Hrbek, J.; Evans, J.; Pérez, M., Activity of CeO_x and TiO_x nanoparticles grown on Au(111) in the water-gas shift reaction. *Science* **2007,** *318* (5857), 1757-1760.

62. Rodriguez, J. A.; Liu, P.; Graciani, J.; Senanayake, S. D.; Grinter, D. C.; Stacchiola, D.; Hrbek, J.; Fernández-Sanz, J., Inverse oxide/metal catalysts in fundamental studies and practical applications: a perspective of recent developments. *J. Phys. Chem. Lett.* **2016,** *7* (13), 2627-2639.

63. Wichmann, A.; Wittstock, A.; Frank, K.; Biener, M. M.; Neumann, B.; Mädler, L.; Biener, J.; Rosenauer, A.; Bäumer, M., Maximizing activity and stability by turning gold catalysis upside down: oxide particles on nanoporous gold. *ChemCatChem.* **2013,** *5* (7), 2037-2043.

64. Bagge-Hansen, M.; Wichmann, A.; Wittstock, A.; Lee, J. R. I.; Ye, J.; Willey, T. M.; Kuntz, J. D.; van Buuren, T.; Biener, J.; Bäumer, M.; Biener, M. M., Quantitative phase composition of TiO_2-coated nanoporous Au monoliths by X-ray absorption

spectroscopy and correlations to catalytic behavior. *J. Phys. Chem. C* **2014,** *118* (8), 4078-4084.

65. Rumancev, C.; von Gundlach, A. R.; Baier, S.; Wittstock, A.; Shi, J.; Benzi, F.; Senkbeil, T.; Stuhr, S.; Garamusx, V. M.; Grunwaldt, J. D.; Rosenhahn, A., Morphological analysis of cerium oxide stabilized nanoporous gold catalysts by soft X-ray ASAXS. *RSC Advances* **2017,** *7* (72), 45344-45350.

66. Shi, J.; Schaefer, A.; Wichmann, A.; Murshed, M. M.; Gesing, T. M.; Wittstock, A.; Bäumer, M., Nanoporous gold-supported ceria for the water–gas shift reaction: UHV inspired design for applied catalysis. *J. Phys. Chem. C* **2014,** *118* (50), 29270-29277.

67. Shi, J.; Mahr, C.; Murshed, M. M.; Zielasek, V.; Rosenauer, A.; Gesing, T. M.; Bäumer, M.; Wittstock, A., A versatile sol–gel coating for mixed oxides on nanoporous gold and their application in the water gas shift reaction. *Catal. Sci. Technol.* **2016,** *6* (14), 5311-5319.

68. Shi, J.; Mahr, C.; Murshed, M. M.; Gesing, T. M.; Rosenauer, A.; Bäumer, M.; Wittstock, A., Steam reforming of methanol over oxide decorated nanoporous gold catalysts: a combined in situ FTIR and flow reactor study. *Phys. Chem. Chem. Phys.* **2017,** *19* (13), 8880-8888.

69. Dutta, P.; Pal, S.; Seehra, M. S.; Shi, Y.; Eyring, E. M.; Ernst, R. D., Concentration of Ce^{3+} and oxygen vacancies in cerium oxide nanoparticles. *Chem. Mater.* **2006,** *18* (21), 5144-5146.

70. Wang, Y.-G.; Mei, D.; Glezakou, V.-A.; Li, J.; Rousseau, R., Dynamic formation of single-atom catalytic active sites on ceria-supported gold nanoparticles. *Nat. Commun.* **2015,** *6*, 6511.

71. Kim, H. Y.; Henkelman, G., CO oxidation at the interface of Au nanoclusters and the stepped-CeO_2(111) surface by the Mars–van Krevelen Mechanism. *J. Phys. Chem. Lett.* **2013,** *4* (1), 216-221.

72. Kim, H. Y.; Henkelman, G., CO oxidation at the interface between doped CeO_2 and supported Au nanoclusters. *J. Phys. Chem. Lett.* **2012,** *3* (16), 2194-2199.

73. Camellone, M. F.; Fabris, S., Reaction mechanisms for the CO Oxidation on Au/CeO_2 catalysts: activity of substitutional Au^{3+}/Au^+ cations and deactivation of

supported Au$^+$ Adatoms. *J. Am. Chem. Soc.* **2009,** *131* (30), 10473-10483.

74. Kim, H. Y.; Lee, H. M.; Henkelman, G., CO Oxidation mechanism on CeO2-supported Au nanoparticles. *J. Am. Chem. Soc.* **2012,** *134* (3), 1560-1570.

75. Rodriguez, J. A., Gold-based catalysts for the water–gas shift reaction: Active sites and reaction mechanism. *Catal. Today* **2011,** *160* (1), 3-10.

76. Zhou, Z.; Kooi, S.; Flytzani-Stephanopoulos, M.; Saltsburg, H., The role of the interface in CO oxidation on Au/CeO2 multilayer nanotowers. *Adv. Funct. Mater.* **2008,** *18* (18), 2801-2807.

77. Longo, A.; Liotta, L. F.; Pantaleo, G.; Giannici, F.; Venezia, A. M.; Martorana, A., structure of the metal–Ssupport interface and oxidation state of gold nanoparticles supported on ceria. *J. Phys. Chem. C* **2012,** *116* (4), 2960-2966.

78. Ta, N.; Liu, J.; Chenna, S.; Crozier, P. A.; Li, Y.; Chen, A.; Shen, W., Stabilized gold nanoparticles on ceria nanorods by strong interfacial anchoring. *J. Am. Chem. Soc.* **2012,** *134* (51), 20585-20588.

79. Yang, F.; Graciani, J.; Evans, J.; Liu, P.; Hrbek, J.; Sanz, J. F.; Rodriguez, J. A., CO oxidation on inverse CeO$_x$/Cu(111) catalysts: high catalytic activity and ceria-promoted dissociation of O2. *J. Am. Chem. Soc.* **2011,** *133* (10), 3444-3451.

80. Montemore, M. M.; Madix, R. J.; Kaxiras, E., How does nanoporous gold dissociate molecular oxygen? *J. Phys. Chem. C* **2016,** *120* (30), 16636-16640.

81. Fajín, J. L. C.; Cordeiro, M. N. D. S.; Gomes, J. R. B., On the theoretical understanding of the unexpected O2 activation by nanoporous gold. *Chem. Commun.* **2011,** *47* (29), 8403-8405.

82. Li, Y.; Dononelli, W.; Moreira, R.; Risse, T.; Bäumer, M.; Klüner, T.; Moskaleva, L. V., Oxygen-driven surface evolution of nanoporous gold: insights from ab initio molecular dynamics and auger electron spectroscopy. *J. Phys. Chem. C* **2018,** *122* (10), 5349-5357.

83. Röhe, S.; Frank, K.; Schaefer, A.; Wittstock, A.; Zielasek, V.; Rosenauer, A.; Bäumer, M., CO oxidation on nanoporous gold: A combined TPD and XPS study of active catalysts. *Surf. Sci.* **2013,** *609*, 106-112.

84. Hoppe, S.; Li, Y.; Moskaleva, L. V.; Muller, S., How silver segregation stabilizes

1D surface gold oxide: a cluster expansion study combined with ab initio MD simulations. *Phys. Chem. Chem. Phys.* **2017,** *19* (22), 14845-14853.

85. Fajin, J. L. C.; Cordeiro, M. N. D. S.; Gomes, J. R. B., On the theoretical understanding of the unexpected O2activation by nanoporous gold. *Chem. Commun.* **2011,** *47* (29), 8403-8405.

86. Moskaleva, L. V., Theoretical mechanistic insights into propylene epoxidation on Au-based catalysts: Surface O versus OOH as oxidizing agents. *Catal. Today* **2016,** *278*, 45-55.

87. Moskaleva, L. V.; Dononelli, W.; Klüner, T., Aerobic oxidation of alcohols on nanoporous gold: Toward a mechanistic understanding of reactivity. In *Encyclopedia of Interfacial Chemistry - Surface Science and Electrochemistry*, Elsevier: 2017.

88. Chang, C.-R.; Wang, Y.-G.; Li, J., Theoretical investigations of the catalytic role of water in propene epoxidation on gold nanoclusters: A hydroperoxyl-mediated pathway. *Nano Res.* **2011,** *4* (1), 131-142.

89. He, Y.; Liu, J.-C.; Luo, L.; Wang, Y.-G.; Zhu, J.; Du, Y.; Li, J.; Mao, S. X.; Wang, C., Size-dependent dynamic structures of supported gold nanoparticles in CO oxidation reaction condition. *Proce. Natl. Acad. Sci.* **2018,** *115* (30), 7700.

90. Song, W.; Hensen, E. J. M., Structure sensitivity in CO oxidation by a single Au atom supported on ceria. *J. Phys. Chem. C* **2013,** *117* (15), 7721-7726.

91. Pan, Y.; Nilius, N.; Freund, H.-J.; Paier, J.; Penschke, C.; Sauer, J., Titration of Ce^{3+} ions in the CeO_2(111) surface by Au adatoms. *Phys. Rev. Lett.* **2013,** *111* (20), 206101.

92. Hernández, N. C.; Grau-Crespo, R.; de Leeuw, N. H.; Sanz, J. F., Electronic charge transfer between ceria surfaces and gold adatoms: a GGA+U investigation. *Phys. Chem. Chem. Phys.* **2009,** *11* (26), 5246-5252.

93. Song, W.; Hensen, E. J. M., Mechanistic aspects of the water–gas shift reaction on isolated and clustered Au atoms on CeO_2(110): a density functional theory study. *ACS. Catal.* **2014,** *4* (6), 1885-1892.

94. Borden, W. T.; Hoffmann, R.; Stuyver, T.; Chen, B., Dioxygen: What makes this triplet diradical kinetically persistent? *J. Am. Chem. Soc.* **2017,** *139* (26), 9010-9018.

95. Li, Y.; Zhang, G.; Eugen Schwarz, W. H.; Li, J., Excited-state chemistry:

photocatalytic methanol oxidation by uranyl@zeolite through oxygen-centered radicals. *Inorg. Chem.* **2020**.

96. Chang, C.-R.; Yang, X.-F.; Long, B.; Li, J., A water-promoted mechanism of alcohol oxidation on a Au(111) surface: understanding the catalytic behavior of bulk gold. *ACS. Catal.* **2013,** *3* (8), 1693-1699.

97. Wang, Y.-G.; Yoon, Y.; Glezakou, V.-A.; Li, J.; Rousseau, R., The role of Reducible oxide–metal cluster charge transfer in catalytic processes: new insights on the catalytic mechanism of CO oxidation on Au/TiO$_2$ from ab initio molecular dynamics. *J. Am. Chem. Soc.* **2013,** *135* (29), 10673-10683.

98. Duan, Z.; Henkelman, G., Calculations of CO oxidation over a Au/TiO$_2$ catalyst: a study of active sites, catalyst deactivation, and moisture effects. *ACS. Catal.* **2018,** *8* (2), 1376-1383.

99. Molina, L. M.; Rasmussen, M. D.; Hammer, B., Adsorption of O$_2$ and oxidation of CO at Au nanoparticles supported by TiO$_2$(110). *J. Chem. Phys.* **2004,** *120* (16), 7673-7680.

100. Schlexer, P.; Widmann, D.; Behm, R. J.; Pacchioni, G., CO oxidation on a Au/TiO$_2$ nanoparticle catalyst via the Au-assisted Mars–van Krevelen Mechanism. *ACS. Catal.* **2018,** *8* (7), 6513-6525.

101. Nolan, M.; Watson, G. W., The surface dependence of CO adsorption on Ceria. *J. Phys. Chem. B* **2006,** *110* (33), 16600-16606.

102. Hussain, A.; Curulla Ferré, D.; Gracia, J.; Nieuwenhuys, B. E.; Niemantsverdriet, J. W., DFT study of CO and NO adsorption on low index and stepped surfaces of gold. *Surf. Sci.* **2009,** *603* (17), 2734-2741.

103. Mehmood, F.; Kara, A.; Rahman, T. S.; Henry, C. R., Comparative study of CO adsorption on flat, stepped, and kinked Au surfaces using density functional theory. *Phys. Rev. B* **2009,** *79* (7), 075422.

104. Liu, J.-C.; Wang, Y.-G.; Li, J., Toward rational design of oxide-supported sSingle-Aatom catalysts: atomic dispersion of gold on ceria. *J. Am. Chem. Soc.* **2017,** *139* (17), 6190-6199.

105. Wang, J.; McEntee, M.; Tang, W.; Neurock, M.; Baddorf, A. P.; Maksymovych, P.;

Yates, J. T., Formation, migration, and reactivity of Au–CO complexes on gold surfaces. *J. Am. Chem. Soc.* **2016,** *138* (5), 1518-1526.

106. Wang, A.; Li, J.; Zhang, T., Heterogeneous single-atom catalysis. *Nat. Rev. Chem.* **2018,** *2* (6), 65-81.

107. Thomas, J. M.; Saghi, Z.; Gai, P. L., Can a single atom serve as the active site in some heterogeneous catalysts? *Top Catal.* **2011,** *54* (10), 588-594.

108. Penschke, C.; Paier, J., Reduction and oxidation of Au adatoms on the CeO2(111) surface – DFT+U versus hybrid functionals. *Phys. Chem. Chem. Phys.* **2017,** *19* (19), 12546-12558.

109. Branda, M. M.; Castellani, N. J.; Grau-Crespo, R.; Leeuw, N. H. d.; Hernandez, N. C.; Sanz, J. F.; Neyman, K. M.; Illas, F., On the difficulties of present theoretical models to predict the oxidation state of atomic Au adsorbed on regular sites of CeO$_2$(111). *J. Chem. Phys.* **2009,** *131* (9), 094702.

110. Tosoni, S.; Pacchioni, G., Oxide-supported gold clusters and nanoparticles in catalysis: a computational chemistry perspective. *ChemCatChem.* **2019,** *11* (1), 73-89.

111. Szabo, A.; Ostlund, N. S., *Modern Quantum Chemistry: Introduction to Advanced Electronic Structure Theory*. Dover Publications: 1996.

112. Hohenberg, P.; Kohn, W., Inhomogeneous electron gas. *Phys Rev* **1964,** *136* (3B), B864.

113. Kohn, W.; Sham, L. J., Self-sonsistent equations including exchange and correlation effects. *Phys. Rev.* **1965,** *140* (4A), A1133-A1138.

114. Dudarev, S.; Botton, G.; Savrasov, S.; Humphreys, C.; Sutton, A., Electron-energy-loss spectra and the structural stability of nickel oxide: An LSDA+ U study. *Phys. Rev. B* **1998,** *57* (3), 1505.

115. Hoover, W. G., Canonical dynamics: equilibrium phase-space distributions. *Phys. Rev. A* **1985,** *31* (3), 1695.

116. Kresse, G.; Hafner, J., Ab initio molecular-dynamics simulation of the liquid-metal-amorphous-semiconductor transition in germanium. *Phys. Rev. B* **1994,** *49* (20), 14251-14269.

117. VandeVondele, J.; Krack, M.; Mohamed, F.; Parrinello, M.; Chassaing, T.; Hutter,

J., Quickstep: Fast and accurate density functional calculations using a mixed Gaussian and plane waves approach. *Comput. Phys. Commun.* **2005,** *167* (2), 103-128.

118. Perdew, J. P., Density-functional approximation for the correlation energy of the inhomogeneous electron gas. *Phys. Rev. B* **1986,** *33* (12), 8822-8824.

119. Perdew, J. P.; Burke, K.; Ernzerhof, M., Generalized gradient approximation made simple. *Phys. Rev. Lett.* **1996,** *77* (18), 3865-3868.

120. Janthon, P.; Kozlov, S. M.; Viñes, F.; Limtrakul, J.; Illas, F., Establishing the Accuracy of Broadly Used Density Functionals in Describing Bulk Properties of Transition Metals. *J. Chem. Theor. Comput.* **2013,** *9* (3), 1631-1640.

121. Janthon, P.; Luo, S.; Kozlov, S. M.; Viñes, F.; Limtrakul, J.; Truhlar, D. G.; Illas, F., Bulk properties of transition metals: a challenge for the design of universal density functionals. *J. Chem. Theor. Comput.* **2014,** *10* (9), 3832-3839.

122. Lippert, G.; Michele, P.; Jurg, H., A hybrid Gaussian and plane wave density functional scheme. *Mol. Phys.* **1997,** *92* (3), 477-488.

123. VandeVondele, J.; Hutter, J., Gaussian basis sets for accurate calculations on molecular systems in gas and condensed phases. *J. Chem. Phys.* **2007,** *127* (11), 114105.

124. Goedecker, S.; Teter, M.; Hutter, J., Separable dual-space Gaussian pseudopotentials. *Phys. Rev. B* **1996,** *54* (3), 1703.

125. Nosé, S., A unified formulation of the constant temperature molecular dynamics methods. *J. Chem. Phys.* **1984,** *81* (1), 511-519.

126. Berne, B. J.; Ciccotti, G.; Coker, D. F., *Classical and quantum dynamics in condensed phase simulations*. World Scientific: 1998.

127. Kresse, G.; Furthmüller, J., Efficiency of ab-initio total energy calculations for metals and semiconductors using a plane-wave basis set. *Comp. Mater. Sci.* **1996,** *6* (1), 15-50.

128. Kresse, G.; Hafner, J., Ab initio molecular-dynamics simulation of the liquid-metal–amorphous-semiconductor transition in germanium. *Phys. Rev. B* **1994,** *49* (20), 14251-14269.

129. Blöchl, P. E., Projector augmented-wave method. *Phys. Rev. B* **1994,** *50* (24), 17953-17979.

130. Kresse, G.; Joubert, D., From ultrasoft pseudopotentials to the projector augmented-wave method. *Phys. Rev. B* **1999,** *59* (3), 1758-1775.

Curriculum Vitae

Yong Li

Born in Guizhou, China, October 1988

Address: Institute of Applied and Physical Chemistry, University of Bremen, 28359, Bremen, Germany

ORCID: https://orcid.org/0000-0002-2774-841X

E-mail: liyong@uni-bremen.de

Professional Experience

Research Associate in Computational chemistry, Institute of Applied and Physical Chemistry (IAPC), University of Bremen (2015-present)

Teaching assistant at the University of Bremen, 2016-2018

Research assistant, Theoretical and Computational Chemistry Laboratory (TCCL), Tsinghua University Beijing (2013-2015)

Education

Bachelor, Metallic Materials Engineering

Wuhan University of Technology and Science, Wuhan, China (2005-2009)

Thesis: Exp. TEM Investigation of the Isotacticity Polypropylene

Master, Engineering and Science

Material Science and Engineering, Guangdong University of Technology (2009-2011)

Quantum Chemistry, Tsinghua University Beijing, (2011-2013)

Thesis: Relativistic Quantum-Chemical Studies of Physical Properties and Photocatalytic Mechanism at $[UO_2]^{2+}$@zeolite Heterogeneous System.

Technical Skills

Programming

Python, Shell scripting

Computational Material and Chemistry Software (expert level)

Material Studio, NWChem, ADF, Gaussian, Molpro, Molcas, CP2K, ORCA, VASP

Research Interests

Investigating energy materials and photoelectric materials and inorganic and bio-organic catalysis and photochemistry, with advanced, computational and simulation methods

Publications

[1] <u>**Li Y**</u>, M. Baeumer, L. V. Moskalev. In Situ Generated Au-CO Complexes Promoting Catalysis in a Ceria/Gold Inverse System: a Theoretical Insight from Ab Initio Molecular Dynamics. *J. Catal.* (Under revision)

[2] <u>**Y. Li***</u>, W. H. Eugen Schwarz, G. Zhang and J. Li. Excited State Chemistry: Photo-Catalytic Methanol Oxidation by Uranyl@Zeolite through Oxygen Centered Radicals –Making Waste Profitable. *Inorg. Chem*., 59 (2020) 6287-6300

[3] <u>**Y. Li**</u>, S. Li, M. Baeumer, E. Ivanova-Shor, L.V. Moskaleva. What Changes on the Inverse Catalyst? Insight from CO Oxidation on Au-Aupported Ceria Nanoparticles using Ab Initio Molecular Dynamics., *ACS. Catal*., 2020, 10, 3164-3174.

[4] S. Zhang, <u>**Y. Li**</u>, H. Zhu, S. Lu, P. Ma, W. Dong, F. Duan, M. Chen, M. Du. Understanding the Role of Nanoscale Hetero-Interfaces in Core/Shell Structures for Water Splitting: Covalent Bonding Interaction Boosts the Activity of Binary Transition Metal Sulfides, *ACS Appl. Mater. Interfaces*, 2020, 12, 6250-6261.

[5] C.-X. Wang, <u>**Y. Li***</u>, Z.-F. Li, Z.-J. Liu, E.F. Valeev, L.V. Moskaleva. A

Combined Relativistic Ab Initio Multireference and Experimental Study of the Electronic Structure of Terbium Luminescent Compound. *J. Phys. Chem. A*, 2020, 124, 82-89.

[6] **Y. Li**, W. Dononelli, R. Moreira, T. Risse, M. Bäumer, T. Klüner, L.V. Moskaleva. Oxygen-Driven Surface Evolution of Nanoporous Gold: Insights from Ab Initio Molecular Dynamics and Auger Electron Spectroscopy. *J. Phys. Chem. C*, 2018, 122, 5349-5357.

[7] Y. Li, **Y. Li,** Y. Wan, Y. Xie, J. Zhu, H. Pan, X. Zheng, C. Xia. Perovskite Oxyfluoride Electrode Enabling Direct Electrolyzing Carbon Dioxide with Excellent Electrochemical Performances. *Adv. Energy Mater.*, 2019, 9, 1803156.

[8] Z. Zhuang, **Y. Li**, J. Huang, Z. Li, K. Zhao, Y. Zhao, L. Xu, L. Zhou, L.V. Moskaleva, L. Mai. Sisyphus Effects in Hydrogen Electrochemistry on Metal Silicides Enabled by Silicene Subunit Edge. *Sci. Bull*., 2019, 64, 617-624.

[9] Z. Zhuang, J. Huang, **Y. Li,** L. Zhou, L. Mai. The Holy Grail in Platinum-Free Electrocatalytic Hydrogen Evolution: Molybdenum-Based Catalysts and Recent Advances. *ChemElectroChem*., 2019, 6, 3570-3589.

[10] J. Du, **Y. Li**, H. Liu, W. Shi, L.V. Moskaleva, P. Cheng. Formation of One-Dimensional Coordination Chains for High-Performance Anode Materials of Lithium-Ion Batteries via a Bottom-Up Approach, *ACS Appl. Mater. Interfaces*, 2019, 11, 25863-25869.

[11] C. Yu, **Y. Li**, M.J. Willans, Y. Zhao, K.R. Adair, F. Zhao, W. Li, S. Deng, J. Liang, M.N. Banis, R. Li, H. Huang, L. Zhang, R. Yang, S. Lu, Y. Huang, X. Sun. Superionic Conductivity in Lithium Argyrodite Solid-State Electrolyte by Controlled Cl-Doping. *Nano Energy*, 2019, 69, 104396.

[12] J.-B. Lu, X.-L. Ma, J.-Q. Wang, Y.-F. Jiang, **Y. Li**, H.-S. Hu, H. Xiao, J. Li. The df–d Dative Bonding in a Uranium–Cobalt Heterobimetallic Complex for Efficient Nitrogen Fixation. *Inorg. Chem.*, 2019, 58, 7433-7439.

[13] G. Tomaschun, W. Dononelli, **Y. Li**, M. Bäumer, T. Klüner, L.V. Moskaleva. Methanol Oxidation on the Au(310) Surface: A Theoretical Study, *J. Catal.*,

2018, 364, 216-227.

[14] J.-C. Liu, X.-L. Ma, **Y. Li**, Y.-G. Wang, H. Xiao, J. Li. Heterogeneous Fe_3 Single-Cluster Catalyst for Ammonia Synthesis via An Associative Mechanism. ***Nat. Commun***., 2018, 9, 1610.

[15] Z. Zhuang, **Y. Li**, Z. Li, F. Lv, Z. Lang, K. Zhao, L. Zhou, L. Moskaleva, S. Guo, L. Mai. $MoB/g-C_3N_4$ Interface Materials as a Schottky Catalyst to Boost Hydrogen Evolution. ***Angew. Chem***. ***Int***. ***Ed***., 2018, 57, 496-500.

[16] H. Zhu, G. Gao, M. Du, J. Zhou, K. Wang, W. Wu, X. Chen, **Y. Li**, P. Ma, W. Dong, F. Duan, M. Chen, G. Wu, J. Wu, H. Yang, S. Guo. Atomic-Scale Core/Shell Structure Engineering Induces Precise Tensile Strain to Boost Hydrogen Evolution Catalysis. ***Adv. Mater***., 2018, 30, 1707301.

[17] H. Zhu, G. Gao, M. Du, J. Zhou, K. Wang, W. Wu, X. Chen, **Y. Li**, P. Ma, W. Dong, F. Duan, M. Chen, G. Wu, J. Wu, H. Yang, S. Guo. Electrocatalytic Nanomaterials: Atomic-Scale Core/Shell Structure Engineering Induces Precise Tensile Strain to Boost Hydrogen Evolution Catalysis. ***Adv. Mater***., 2018, 30, 1870191.

[18] Q. Liu, X. Yang, L. Li, S. Miao, Y. Li, **Y. Li**, X. Wang, Y. Huang, T. Zhang. Direct Catalytic Hydrogenation of CO_2 to Formate over A Schiff-Base-Mediated Gold Nanocatalyst. ***Nat. Commun***., 2017, 8, 1407.

[19] S. Hoppe, **Y. Li**, L.V. Moskaleva, S. Muller. How Silver Segregation Stabilizes 1D Surface Gold Oxide: A Cluster Expansion Study Combined with Ab Initio MD Simulations. ***Phys. Chem. Chem***. ***Phys***., 2017, 19, 14845-14853.

[20] W.-L. Li, **Y. Li**, C.-Q. Xu, X.-B. Wang, E. Vorpagel, J. Li. Periodicity, Electronic Structures, and Bonding of Gold Tetrahalides $[AuX_4]^-$ (X = F, Cl, Br, I, At, Uus). ***Inorg. Chem***., 2015, 54, 11157-11167.

[21] **Y. Li**, J. Su, E. Mitchell, G. Zhang, J. Li. Photocatalysis with Visible-Light-Active Uranyl Complexes. ***Sci. China Chem***., 2013, 56, 1671-1681.

Reprint of Publications

Publication I

How Silver Segregation Stabilizes 1D Surface Gold Oxide: a Cluster Expansion Study Combined with *Ab Initio* MD Simulations

S. Hoppe, Y. Li, L.V. Moskaleva, S. Muller.

Phys. Chem. Chem. Phys., 2017, 19 14845-14853.
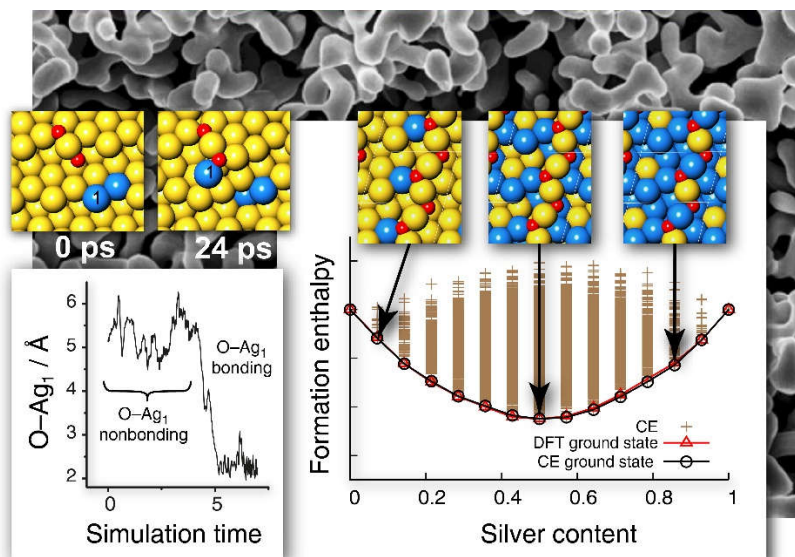
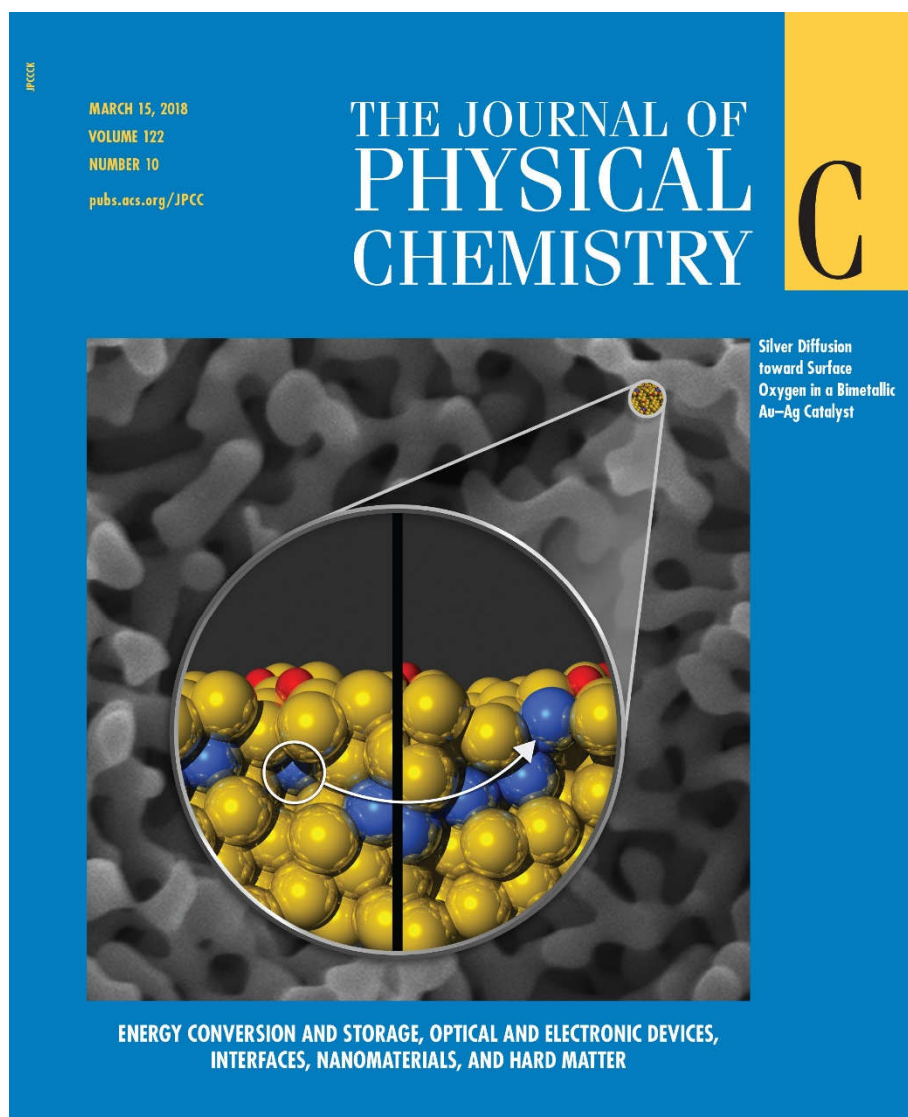The pdf-document of this publication is not embedded for copyright reasons.

The publication can be accessed via the link:

https://doi.org/10.1039/C7CP02221B

Publication II

Oxygen-Driven Surface Evolution of Nanoporous Gold: Insights from *Ab Initio* Molecular Dynamics and Auger Electron Spectroscopy

Y. Li, W. Dononelli, R. Moreira, T. Risse, M. Bäumer, T. Klüner, L.V. Moskaleva

. *J. Phys. Chem. C*, 2018, 122, 5349-5357. (Cover paper)

The pdf-document of this publication is not embedded for copyright reasons.

The publication can be accessed via the link:

https://doi.org/10.1021/acs.jpcc.7b08873

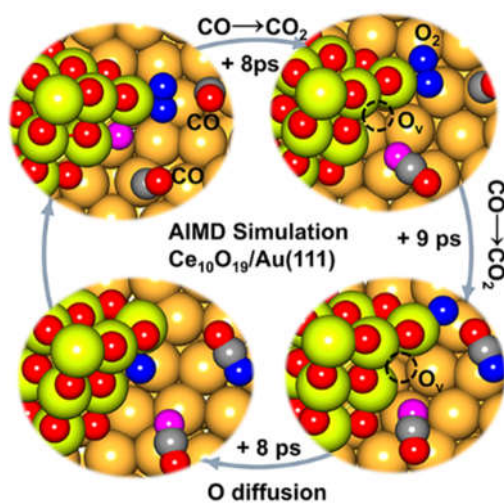**What Changes on the Inverse Catalyst? Insight from CO Oxidation on**

Au-Supported Ceria Nanoparticles using *Ab Initio* Molecular Dynamics

Y. Li, S. Li, M. Baeumer, E. Ivanova-Shor, L.V. Moskaleva

The pdf-document of this publication is not embedded for copyright reasons.

The publication can be accessed via the link:

https://doi.org/10.1021/acscatal.9b05175

Publication IV

Transient Au-CO Complexes Promote the Activity of an Inverse Ceria/Gold Catalyst: an Insight from *Ab Initio* Molecular Dynamics.

<u>**Y. Li**</u>, S. Li, M. Bäumer, L. V. Moskaleva

2020, ***J. Catal.*** Under revision